

This manuscript has been submitted for publication to JOURNAL OF CLIMATE (AMS). Please note that this manuscript has undergone two rounds of peer review but has yet to be formally accepted for publication. Subsequent versions of this manuscript may differ slightly in content.

1 **Efficient Estimation of Climate State and Its Uncertainty Using Kalman**
2 **Filtering with Application to Policy Thresholds and Volcanism**

3

4

J. Matthew Nicklas,^a Baylor Fox-Kemper,^a Charles Lawrence.^a

5

^a *Brown University, Providence, Rhode Island.*

6

7

Corresponding author: J. Matthew Nicklas, john_nicklas@brown.edu

8

9

ABSTRACT

10 We present the Energy Balance Model – Kalman Filter (EBM-KF), a hybrid model of the
11 global mean surface temperature (GMST) and ocean heat content anomaly (OHCA). It
12 combines an annual energy balance model (difference equations) with 17 parameters drawn
13 from the literature and a statistical Extended Kalman Filter assimilating GMST and OHCA,
14 either observed timeseries or simulated by earth system models. Our motivation is to create
15 an efficient and natural estimator of the climate state and its uncertainty, which we believe to
16 be Gaussian at a global scale. We illustrate four applications: 1) EBM-KF generates a similar
17 estimate to the 30-year time-averaged climate state 15 years sooner, or a model-simulated
18 hindcasts' annual ensemble average, depending on the preparation of volcanic forcing. 2)
19 EBM-KF conveniently assesses annually likelihoods of crossing a policy threshold, e.g.,
20 based on temperature records up to the end of 2023, $p=0.0017$ that the climate state was
21 1.5°C over preindustrial, but a 16% likelihood that the GMST in 2023 itself could have been
22 over that threshold. 3) The EBM-KF also approximates the spread of an entire climate model
23 large ensemble using only one or a few ensemble members. 4) The EBM-KF is sufficiently
24 fast to allow thorough sampling from non-Gaussian probabilistic futures, e.g., the impact of
25 rare but significant volcanic eruptions. This sampling with the EBM-KF better determines
26 how future volcanism may affect when policy thresholds will be crossed and what an
27 ensemble with thousands of members exploring future intermittent volcanism reveals.

28

29

SIGNIFICANCE STATEMENT

30 The global average of the Earth's historical climate over the past 150 years can be
31 explained by a thermal/radiation physics equation involving a small number of constants
32 (17), atmospheric CO_2 concentration, human-produced cloud-seeding aerosols, and dust from
33 volcanic eruptions. Global mean surface temperature measurements vary around this climate
34 state within a consistent normal distribution. This physics equation and statistical depiction
35 allowed us to construct a simple model that can rapidly estimate the uncertainty in Earth's
36 current climate, aid in policy discussions, and reduce ensemble modeling costs.

37

38 **1. Introduction**

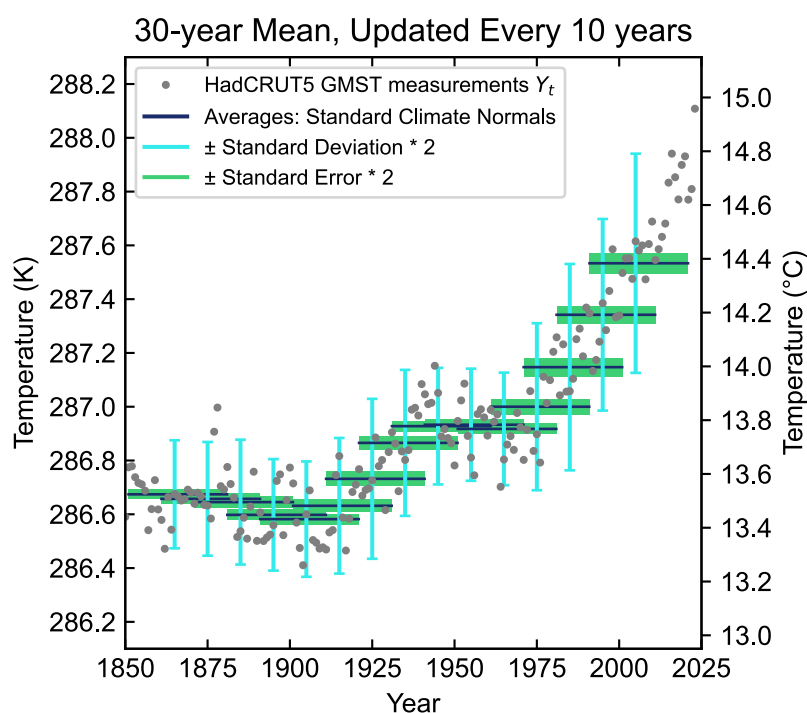
This manuscript has been submitted for publication to JOURNAL OF CLIMATE (AMS). Please note that this manuscript has undergone two rounds of peer review but has yet to be formally accepted for publication. Subsequent versions of this manuscript may differ slightly in content.

39 What is the uncertainty in Earth's climate? From a measurement standpoint, this issue was
40 resolved many decades ago. The instantaneous measurement of global mean surface
41 temperature (GMST) is currently performed with average accuracy of 0.05°C (max 0.10°C)
42 via arrays of infrared-sensing satellites and ground stations (Susskind, Schmidt et al. 2019).
43 Both satellite and ground datasets extend back to 1981 (Merchant, Embury et al. 2019), and
44 the yearly seasonal fluctuation is easy to smooth with a running annual average. However,
45 this GMST still has significant dynamical and random stochasticity, from processes like the
46 2-7 year quasi-periodic El Nino events (Hu and Fedorov 2017) and volcanic eruptions that
47 intermittently affect climate for 1-2 years (Soden, Wetherald et al. 2002). Measurement errors
48 also arise from sparse or inconsistently calibrated historical data and paleoproxies (Carré,
49 Sachs et al. 2012; Emile-Geay, McKay et al. 2017; Kaufman, McKay et al. 2020;
50 McClelland, Halevy et al. 2021). Internal variability dominates over climate-forced
51 variability in most short-term signals, both in climate simulations and reality (Kirtman, Power
52 et al. 2013; Marotzke and Forster 2015; Gulev, Thorne et al. 2021; Lee, Marotzke et al.
53 2021). By “simulations”, we refer to computationally expensive global coupled models (and
54 occasionally to numerical weather model predictions). Other climate variables reveal
55 warming that is steadier than GMST (less “noisy” annual variability). One such steady
56 climate variable is the Ocean Heat Content Anomaly (OHCA), where >90% of the
57 anthropogenic energy anomaly is found (Cheng, Trenberth et al. 2017; Fox-Kemper, Hewitt
58 et al. 2021; Gulev, Thorne et al. 2021; Cheng, von Schuckmann et al. 2022). Even radical
59 reductions in global CO₂ emissions may not show an identifiable impact on GMST over a
60 time scale of a few years (Szopa et al. 2021), posing a challenge for policy and assessment.

61 In 1935 the World Meteorological Association began reporting the "standard climate
62 normal" as surface temperature averages over an interval of 30 years (\overline{Y}_t in this paper's
63 notation, starting with 1901-1930). A 30-year window was chosen to minimize most internal
64 fluctuations (such as El Nino) and short-term forcings such as single volcanoes (Guttman
65 1989). Fig. 1 shows this metric and emphasizes the 30-year span over which the average is
66 taken. To generate continuous estimates of the climate, this 30-year average can be updated
67 annually rather than decadal, forming a running mean (Supp. Fig. 4b). While standard
68 climate normals and running means are straightforward and widely accepted definitions of
69 climate, they involve lag: the most current 30-year unweighted average necessarily describes
70 the average climate state of Earth over a window centered on 15 years ago. Weighted moving
71 averaging can shift the center of this window closer toward the current year but some lag

This manuscript has been submitted for publication to JOURNAL OF CLIMATE (AMS). Please note that this manuscript has undergone two rounds of peer review but has yet to be formally accepted for publication. Subsequent versions of this manuscript may differ slightly in content.

72 always remains. Moreover, anthropogenic climate change distorts standard statistical metrics:
73 most of the variance in recent 30-year periods derives from the trend rather than internal
74 variability (Fig. 1). Averaging filters (such as a running mean) remove high-frequency signals
75 that reflect year-to-year variations in global weather, as do other statistical approaches better-
76 suited to removing frequencies above a particular cutoff (Smith 2003). The anthropogenic
77 change in Fig. 1 is gradual enough to be preserved by moving averages (running mean) or
78 any lowpass filter / smoother. But this is not true in general: in a hypothetical (or
79 extraterrestrial) climate where forcings undergo an impulse change, such as a quadrupling of
80 CO₂ within 1 year, the 30-year running mean inadequately represents the climate state (see
81 supplemental Section B, Supp. Fig. 3). To directly fit the effect of forcings to the climate
82 (incorporating relaxation time), the multi-pattern fingerprint method was developed,
83 (Hasselmann 1997) leading to “attributable anthropogenic warming” (Otto, Frame et al.
84 2015) and a “real-time Global Warming Index” (Haustein, Allen et al. 2017). This
85 methodology is statistically conservative, generating a wide 5-95% confidence interval
86 spanning $\pm 0.1^{\circ}\text{C}$ from 1980-2010, which then expands out to $\pm 0.15^{\circ}\text{C}$. Other example
87 applications to Earth’s recent GMST of statistical, as opposed to physical, filters used in
88 climate analysis are shown in supplemental Section B (Supp. Figs. 4c,d & 5).



89

90 Fig. 1: Illustration of Standard Climate Normals $\overline{{}_{30}Y_t}$ (blue horizontal lines in 10-year
91 overlapping bins) as applied to the HadCRUT5 GMST dataset (grey dots) (Morice, Kennedy

This manuscript has been submitted for publication to JOURNAL OF CLIMATE (AMS). Please note that this manuscript has undergone two rounds of peer review but has yet to be formally accepted for publication. Subsequent versions of this manuscript may differ slightly in content.

92 et al. 2021). Twice the population standard deviation ($\pm 2\sigma$) is plotted above and below (cyan
93 error bars), and two standard errors are also plotted (green rectangles). Note how standard
94 deviations widen in recent decades due to the anthropogenic trend, and the most recent
95 standard climate normal is much cooler than recent GMST measurements.

96

97 Policy goals often are framed via climate change staying below a particular policy
98 threshold (e.g., 1.5°C or 2°C above pre-industrial conditions as in the Paris Agreement).
99 Using a 30-year mean brings difficulty in determining exactly when or if a policy threshold is
100 crossed (Lee, Marotzke et al. 2021). Policy thresholds are not system thresholds —
101 temperature “tipping” points when the dynamics of the climate system are reorganized, often
102 occurring abruptly or irreversibly — and so they are subject to definitional uncertainty.
103 Relatedly, magnitudes and uncertainty ranges are meaningful only under specific averaging
104 windows, e.g., “GMST increased by 0.85 (0.69 - 0.95) °C between 1850–1900 and 1995–
105 2014 and by 1.09 (0.95 - 1.20)°C between 1850–1900 and 2011–2020.” (Gulev, Thorne et al.
106 2021). Tools for assessing if a policy threshold has been crossed yet will be useful as these
107 policy targets approach. Throughout this paper we use both $\mu \pm 2\sigma$ and μ (a - b) notation to
108 refer to 95% confidence intervals (95% CI), in contrast to [a-b] notation which refers to finite
109 or closed ranges. In this notation, μ is a point estimate, σ is a standard deviation, a is the
110 minimum of the interval or range, and b is the maximum.

111 To overcome limited sampling of the real world, many climate studies instead investigate
112 the climate system within globally coupled climate simulations (“coupled” refers to
113 interacting sub-models, such as atmosphere/ocean/land/ice components), also known as earth
114 system models or ESMs (Meehl, Moss et al. 2014). Typically, these simulations are forced
115 using historical records and a range of scenarios for future projections including CO₂
116 emissions, other pollutants, land use, and volcanic eruptions (Lee, Marotzke et al. 2021). The
117 chaotic nature of weather and varying initial conditions produce an ensemble of identically-
118 forced simulations that explore the span of outcomes consistent with forcing, such as for the
119 CESM2 Large Ensemble (Rodgers, Lee et al. 2021), abbreviated here as LENS2 (Supp. Fig.
120 6). Unfortunately, each ensemble member simulation is computationally expensive and does
121 not accurately or transparently reflect the real climate system, but only one realization of it
122 including model errors. Combining such ensembles with real observations yields
123 improvements, such as a more realistic possible spread (due to internal variability) of winter
124 temperatures in North America from 1966-2015. (McKinnon, Poppick et al. 2017) Betts,
125 Belcher et al. (2023) proposed combining 10 years of previous observations with a

This manuscript has been submitted for publication to JOURNAL OF CLIMATE (AMS). Please note that this manuscript has undergone two rounds of peer review but has yet to be formally accepted for publication. Subsequent versions of this manuscript may differ slightly in content.

126 subsequent 10 years forecasted by several ESMs, an approach named the “current global
127 warming level”. While useful, this technique cannot completely solve all issues inherent to
128 ESMs, such as whether some predictions should be weighted over others (Lehner, Deser et al.
129 2020; Sherwood, Webb et al. 2020), or how an ensemble of short-term projections should be
130 initialized.

131 We sought an efficient and natural estimator of the climate state and its uncertainty: the
132 EBM-KF. We combined a nonlinear energy-balance difference equation (EBM) and a
133 statistical observation equation (KF) that brings in the available measured GMST and OHCA
134 data, yielding a hybrid physical model – statistical filter. This data-driven climate emulator
135 (Forster, Storelvmo et al. 2021) is vastly more computationally efficient than ensembles of
136 ESMs that provide similar information about GMST. Our emulator is interpretable as a global
137 energy budget (and so assimilates OHCA as well as GMST), benefits from the mathematical
138 similarities between an energy balance model and a Kalman Filter, and allows access to
139 proven methodologies for parameter estimation (Chen, Heckman et al. 2018; Zhang and Atia
140 2020) and uncertainty quantification (Sætrum and Omre 2013). We did not empirically fit
141 this emulator to the climate record: 12 of the 17 parameters within the energy-balance
142 equation were directly obtained from literature estimates, whereas the remaining 5 parameters
143 are inferred indirectly from assumed pre-industrial climate equilibrium and literature
144 estimates of climate sensitivities. Thus, while some of these parameters were calibrated to the
145 historical climate record independently by other researchers, they were not adjusted to suit
146 this novel EBM combination. Our simple iterative EBM has good skill at predicting the
147 GMST and OHCA despite being by itself "blind" to all measurements (i.e., it’s a “forward”
148 model in numerical weather prediction terminology). The statistical component is an
149 Extended Kalman Filter, which allows for incorporation of current measurements to "course-
150 correct" under a well-understood mathematical framework, with time-varying “weather” and
151 “climate state” uncertainty. Other noise covariance matrices had to be fixed a priori within
152 the statistical Kalman Filter framework to incorporate observational uncertainty. Part of this
153 noise was due to time-varying uncertainty provided with the observations of GMST and
154 OHCA. Another part of the noise covariance was chosen such that the variability in “climate
155 state” most closely resembles the 30-year running mean of GMST and OHCA. While perhaps
156 unconventional in data assimilation, this approach is directly analogous to the inference of
157 some of our parameters: a handful of numbers were abstracted from the historical climate
158 record using established statistical methods. Hybridizing the EBM with the Extended Kalman

This manuscript has been submitted for publication to JOURNAL OF CLIMATE (AMS). Please note that this manuscript has undergone two rounds of peer review but has yet to be formally accepted for publication. Subsequent versions of this manuscript may differ slightly in content.

159 Filter yields statistical distributions of internal variability and a physical rationale for the
160 filtered current climate state.

161 First, the EBM-KF is introduced within Section 2 in phases: the EBM in Section 2a and
162 the structure of the Extended Kalman Filter in Section 2b. An elaboration beyond fixed
163 assumed measurement uncertainty is detailed in Section 2c. The scope of EBM-KF is
164 expanded to future projections including volcanic eruptions in Section 2d. Then in Section 3,
165 EBM-KF is illustrated on four applications to historical and future climate. Section 3a shows
166 that it estimates the 30-year mean climate normal every year, including the latest observations
167 and without lag. Section 3b shows how it can be used to assess the probability that a policy
168 threshold has been crossed in any particular year. Section 3c shows how it can be used to
169 estimate the ensemble mean of an ESM Large Ensemble from only one ensemble member.
170 Section 3d shows that the EBM-KF is sufficiently fast to allow high-density sampling of non-
171 Gaussian probabilistic futures, e.g., directly sampling over highly intermittent distributions of
172 future volcanic eruptions. Section 4 discusses these results, some cautionary remarks,
173 opportunities for extension, and application to policymaking. Section 5 concludes. Extensive
174 appendices and supplementary material convey additional detail. Throughout, a 2σ or
175 approximately 95% confidence interval is used, indicating the *extremely likely* range in IPCC
176 terminology.

177 **2. Methods**

178 *a. Energy-Balance Model*

179 We constructed the energy-balance model (Fig. 2) by envisioning a uniform planet and
180 capturing the principal atmospheric and surface energy fluxes (Budyko 1969; Sellers 1969).
181 This model is “blind” with respect to observations and is inspired by other energy-budget
182 models illustrating quantitative skill (Hu and Fedorov 2017; Kravitz, Rasch et al. 2018) at
183 approximating both GMST and the 30-year running mean. The model includes two idealized
184 layers, with each layer having homogenous temperature: a surface layer including thermally
185 active soil and 86m of ocean water depth (with temperature approximating GMST), and a
186 deep ocean layer reaching (1141+86)m depth that exchanges energy (part of OHCA) with the
187 surface layer (Gregory 2000; Held, Winton et al. 2010; Geoffroy, Saint-Martin et al. 2013).
188 These depths are chosen to select a two-state system that best represents the heat capacities of
189 spatially complex heat uptake patterns in total into the global oceans (Newsom, Zanna et al.
190 2023), rather than representing the heat uptake relative to depths associated with

This manuscript has been submitted for publication to JOURNAL OF CLIMATE (AMS). Please note that this manuscript has undergone two rounds of peer review but has yet to be formally accepted for publication. Subsequent versions of this manuscript may differ slightly in content.

191 observational oceanographic traditions (e.g. 700m, 2000m). As this EBM does not directly
 192 incorporate any spatial dimensions, it should be considered 0-dimensional in the context of
 193 other ESMs with spatial gradients. Closely related variables to GMST, such as Global
 194 Surface Air Temperature (GSAT), differ only from GMST by measurement and slightly in
 195 uncertainty (by less than our confidence intervals) but not systematically (Gulev et al. 2021).
 196 For example, GMST is easier to measure in the past, while GSAT is a standard output
 197 variable in future model projections, so here we do not distinguish between them.

198 The overall energy fluxes into the model layers are as follows:

$$199 \quad C_{\text{surf}} \frac{dT}{dt} = \mathcal{F}_{\text{sw}}(T, t) - \phi_{\text{LW}}(T, t) - \gamma * (T - \theta - \zeta_0) \quad (1)$$

$$200 \quad C_{\text{deepO}} \frac{d\theta}{dt} = \gamma * (T - \theta - \zeta_0) \quad (2)$$

$$201 \quad H = (T - T_{1850}) * C_{\text{upperO}} + (\theta - \theta_{1850}) * C_{\text{deepO}} \quad (3)$$

$$202 \quad \mathcal{F}_{\text{sw}}(T, t) = \frac{1}{4} G_{\text{SC}}(t) * \tilde{d}(t) * f_{\text{aA}}(T, t) * f_{\text{aS}}(T) \quad (4)$$

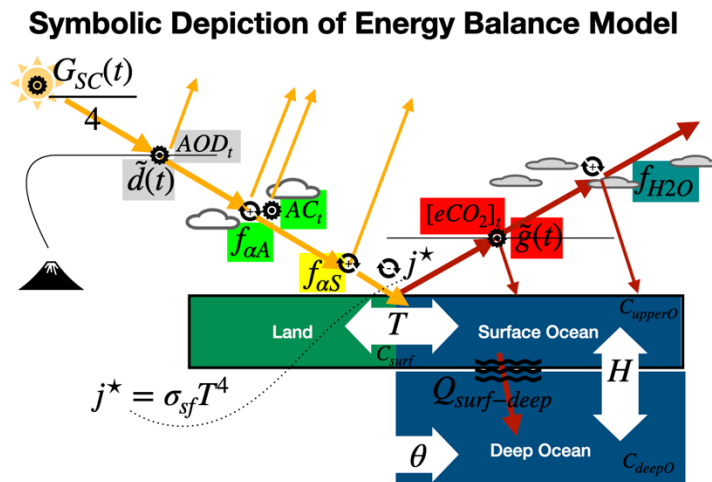
$$203 \quad \phi_{\text{LW}}(T, t) = \sigma_{\text{sf}} T^4 * \tilde{g}(t) * f_{\text{H2O}}(T) \quad (5)$$

204 T is GMST, whereas θ is the potential (or conservative) temperature of the deep ocean in
 205 that same year, and H is OHCA including both that deep ocean layer and the surface ocean
 206 (McDougall, Barker et al. 2021). The time variable t is the calendar year index, and often
 207 used as a subscript (e.g. $t=2000$, T_{2000} is the modeled GMST in the year 2000). On the right
 208 side of the equation, both the shortwave radiative flux ($\mathcal{F}_{\text{sw}}(T, t)$) and longwave radiative
 209 flux ($\phi_{\text{LW}}(T, t)$) take the same form: (source $\frac{G_{\text{SC}}}{4}$, $\sigma_{\text{sf}} T^4$) * (prescribed attenuation from
 210 forcing: $\tilde{d}(t)$, $\tilde{g}(t)$) * (attenuation functions with feedback: $f_i(T)$). The attenuation function
 211 of clouds on shortwave light $f_{\text{aA}}(T, t)$, contains both prescribed forcing and feedback. The
 212 overall surface heat capacity, C_{surf} , is 17 ± 7 W (year) $\text{m}^{-2} \text{K}^{-1}$, obtained from modeling /
 213 timeseries analysis (Schwartz, 2007), including 11.7 W (year) $\text{m}^{-2} \text{K}^{-1}$ or 86m of upper
 214 surface ocean C_{upperO} , while there is a separate deep ocean heat sink with capacity 155.7 W
 215 (year) $\text{m}^{-2} \text{K}^{-1}$ or 1141m C_{deepO} (Geoffroy, Saint-Martin et al. 2013; Hall and Fox-Kemper
 216 2023). $\frac{G_{\text{SC}}}{4}$ is the total solar irradiance (TSI) normalized to the Earth's surface area at ~ 340.2
 217 W/m^2 ; we incorporated its record $\frac{1}{4} G_{\text{SC}}(t)$ of $[340.06 - 340.48]$ from Coddington (2017) but
 218 these variations were found to be insignificant to the climate. $\tilde{d}(t)$ is the prescribed record of
 219 shortwave radiation attenuation due to volcanic dust (values of aerosol optical depth AOD_t

This manuscript has been submitted for publication to JOURNAL OF CLIMATE (AMS). Please note that this manuscript has undergone two rounds of peer review but has yet to be formally accepted for publication. Subsequent versions of this manuscript may differ slightly in content.

220 from Sato (1993), Vernier (2011), and NASA (2018)), $f_{\alpha\Lambda}(T, t)$ is the additional atmospheric
 221 shortwave attenuation due to cloud albedo incorporating both feedback and anthropogenic
 222 cloud-nucleating aerosols AC_i , while $f_{\alpha S}(T)$ is the surface shortwave attenuation due to
 223 ground albedo. Infrared heat emitted from the surface is $j^* = \sigma_{sf} T^4$, the ideal Planck black
 224 body radiation. $\tilde{g}(t)$ is the prescribed record of longwave attenuation due to CO₂ and other
 225 greenhouse gasses combined as effective carbon dioxide concentration $[eCO_2]_t$, and $f_{H_2O}(T)$ is
 226 the additional atmospheric longwave attenuation due to water vapor parameterized as a
 227 function of GMST.

228 We can choose to pre-filter the input forcings because we are most interested in the
 229 slowly evolving climate state. This pre-filtering is inconsequential for greenhouse gasses
 230 which are slowly evolving anyway, but it is very consequential for aerosol optical depth
 231 which undergoes impulse changes during volcanic eruptions. In the discussion section, we
 232 will return to the consequences of pre-filtering.



233
 234 Fig. 2: Diagram of the Energy Balance Model, with all major forcing functions,
 235 corresponding climate driver datasets, and feedback functions (j^* or f_i) represented. All
 236 feedback functions are dependent on surface temperature T , but this is not written on the
 237 diagram above for simplicity. Shortwave incoming solar radiation is successively fractionated
 238 by various forcing and feedback functions, as is outgoing longwave radiation. These in net
 239 warm the surface layer, which in turn warms the deep ocean.

240 Both AC_i and $\tilde{g}(t)$ are taken from Forster et. al. (2023). Several of the coefficients within
 241 the feedback functions f_i are defined to satisfy the constraints of the climate feedbacks
 242 presented in the IPCC AR6 (Forster et al. 2021; particularly Table 7.10), and all coefficients
 243 are based on observational and modeling literature values, typically with energy fluxes
 244 measured from satellites and temperature feedback coefficients determined from model

This manuscript has been submitted for publication to JOURNAL OF CLIMATE (AMS). Please note that this manuscript has undergone two rounds of peer review but has yet to be formally accepted for publication. Subsequent versions of this manuscript may differ slightly in content.

245 results (full derivation in Appendix A and Supplemental). Because the Planck radiation
246 requires absolute temperatures, we use degrees Kelvin in model calculations and convert to
247 °C. OHCA is also approximately convertible to thermosteric sea level rise, via the 0.0121
248 cm/ZJ factor from analysis of 1995 to 2014 (Fox-Kemper, Hewitt et al. 2021). With this
249 factor, the estimated thermosteric sea level rises we find are consistent with observations and
250 projections. Thus, the EBM also estimates sea level rise in this manner (Fox-Kemper, Hewitt
251 et al. 2021). The two negative albedo attenuations, $f_{ad}(T, \theta) * f_{as}(T)$ are expressed relative to
252 $Y_{2002} = 287.55\text{K}$ (14.40°C), the inferred (see below) GMST measurement in 2002 (Jones and
253 Harpham 2013; Morice, Kennedy et al. 2021).

254 $\zeta_0 = 10^\circ\text{C}$ is an equilibrium temperature difference between the surface layer (including
255 the upper ocean) and the deep ocean, arising because the global ocean is thermally stratified.
256 This realistic choice of ζ_0 , explained below, does not affect either T or H , provided that θ and
257 T are in equilibrium at the model's preindustrial initialization (and thus ζ_0 is often abstracted
258 away in similar 2-layer energy-balance models) (Gregory 2000; Held, Winton et al. 2010;
259 Geoffroy, Saint-Martin et al. 2013). γ is the thermal conductivity or "efficiency" between
260 layers of the ocean, taken from Geoffroy et al. Part II (2013) to be 0.67 W/m²/K, the average
261 from the CMIP5 models. The form of this parameterization of deep ocean temperature
262 exchange follows recent work in emulating ocean heat uptake, ignoring "efficacy factor" heat
263 loss (Gregory 2000; Winton, Takahashi et al. 2010; Geoffroy, Saint-Martin et al. 2013;
264 Emile-Geay, McKay et al. 2017; Palmer, Harris et al. 2018).

265 We first obtained the baseline $\zeta_1 = 287.01\text{K}$ of the HadCRUT5 GMST anomaly (Morice,
266 Kennedy et al. 2021) to place the 1960-1989 "standard climate normal" of absolute GMST
267 HadCRUT5 measurements to fall at 13.85°C, the center of the range (13.7°C - 14°C) given
268 by Jones and Harpham (2013). Measurements of surface temperature will later be assimilated
269 as absolute temperatures: $Y_t = \zeta_1 + (\text{HadCRUT5})_t$. Our model assumes energy fluxes were
270 balanced before industrial forcings, which requires an equilibrium temperature. We set this
271 preindustrial equilibrium temperature to the 1850-1879 "standard climate normal" of
272 286.67K (13.52°C) = T_{1850} , and initialized the 1850 climate state to this temperature. This
273 choice is important regarding the determination of many nonlinear feedback functions and
274 coefficients affecting the surface layer (Eq. 7 below), particularly with respect to the Planck
275 feedback. Inconsequentially to the EBM dynamics, the deep potential ocean temperature θ
276 was initialized to be 276.67K (3.52°C) = θ_{1850} , such that current deep ocean potential
277 temperatures are ~3.8°C, choices consistent with both recent and historical measurements of

This manuscript has been submitted for publication to JOURNAL OF CLIMATE (AMS). Please note that this manuscript has undergone two rounds of peer review but has yet to be formally accepted for publication. Subsequent versions of this manuscript may differ slightly in content.

278 the globally averaged ocean temperature (Robinson and Stommel 1959; Abraham, Baringer
279 et al. 2013). So $\zeta_0 = T_{1850} - \theta_{1850} = 13.55^\circ\text{C} - 3.55^\circ\text{C} = 10^\circ\text{C}$. Initializing the deep ocean
280 potential temperature θ to another value would change ζ_0 correspondingly, such that the
281 modeled heat flow into the deep ocean would be unchanged.

282

$$283 \quad \theta_t = (H_t - (T_t - T_{1850}) * C_{\text{upper0}}) / C_{\text{deep0}} + \theta_{1850} \quad (6)$$

$$284 \quad T_{t+1} = T_t + \frac{(\frac{G_{SC}}{4})_t * c_2}{(AOD_t + c_4)} \left(1 + \beta_2 (T_t - Y_{2002}) + \frac{AC_t - AC_{2002}}{c_3} \right) (1 + \beta_3 (T_t - Y_{2002}))$$

$$285 \quad - c_1 * (T_t)^{4+\eta} (1 - \beta_\theta \log_{10}([e\text{CO}_2]_t)) - \frac{\gamma}{C_{\text{surf}}} (T_t - \theta_t - \zeta_0) \quad (7)$$

$$286 \quad H_{t+1} = H_t + (T_{t+1} - T_t) * C_{\text{upper0}} + \gamma * (T_t - \theta_t - \zeta_0) \quad (8)$$

Symbol	Value (Range)	Derivation or Def.	Source
ζ_1	287.01 K (13.86°C)	$13.85^\circ\text{C} = \zeta_1 + \frac{1}{30} * \sum_{t=1960}^{1989} (\text{HadCRUT5})_t$	(Jones and Harpham 2013)
Y_{2002}	287.55 K (14.40°C)	$\zeta_1 + (\text{HadCRUT5})_{2002}$	(Morice, Kennedy et al. 2021)
T_{1850}	286.67K (13.52°C)	$\zeta_1 + \frac{1}{30} * \sum_{t=1850}^{1879} (\text{HadCRUT5})_t$	(Morice, Kennedy et al. 2021)
θ_{1850}	276.67K (3.52°C)	approx.	(Abraham, Baringer et al. 2013)
ζ_0	10 K (10°C)	$T_{1850} - \theta_{1850}$	(Abraham, Baringer et al. 2013)
γ	$0.67 \frac{W}{K m^2}$	Ocean heat conductivity/year	(Geoffroy, Saint-Martin et al. 2013)
C_{surf}	$17 \frac{W}{K m^2}$	Heat capacity/year, Earth surface	(Schwartz 2007)
C_{upper0}	$11.7 \frac{W}{K m^2}$ (86m H ₂ O)	Heat capacity/year, upper ocean	(Geoffroy, Saint-Martin et al. 2013)
C_{deep0}	$155.7 \frac{W}{K m^2}$ (1141m)	Heat capacity/year, deep ocean	(Geoffroy, Saint-Martin et al. 2013)
η	1.615	Degree of H ₂ O feedback	Eq. A26 & A27
β_θ	0.04660	Infrared reflect per log ₁₀ ppm CO ₂	Eq. A20, A21, & A35
c_1	$2.1989 * 10^{-5} K^{-3+\eta}$	$\frac{\sigma_{sf} \beta_1}{C_{\text{surf}}}$	Eq. A22 & A35
β_2	$0.00136 K^{-1}$	Atm. albedo temp. feedback	Eq. A13 & A28
β_3	$0.00163 K^{-1}$	Ground albedo temp. feedback	Eq. A14 & A29
c_2	$0.4044 \frac{K m^2}{W}$	$0.834 * 0.909 * 9.068 / C_{\text{surf}}$	Eq. A11, A23, A24
c_3	$264.377 \frac{W}{m^2}$	$\frac{\overline{G_{SC}}}{4} \overline{d_{2002}} 0.834$	Eq A23
c_4	9.73 (unitless)	$\frac{2q'}{1-g}$	Eq. A11 (Notation is eq9 of (Harshvardhan and King 1993))
AC_{2002}	$-0.988 \frac{W}{m^2}$	Anthro. cloud rad. forcing, 2002	Eq A23
$(\frac{G_{SC}}{4})_t$	[340.06 – 340.48] $\frac{W}{m^2}$	Top of atm. total solar irradiation	(Coddington, Lean et al. 2017)

This manuscript has been submitted for publication to JOURNAL OF CLIMATE (AMS). Please note that this manuscript has undergone two rounds of peer review but has yet to be formally accepted for publication. Subsequent versions of this manuscript may differ slightly in content.

AOD_t	[0.2 – 142.9]	Aerosol optical depth	(Miller, Schmidt et al. 2014; Nasa/Larc/Sd/Asdc 2018)
AC_t	$[-1.09 – -0.06] \frac{W}{m^2}$	Anthro. cloud radiative forcing	(Forster, Smith et al. 2023)
$[eCO_2]_t$	[287.9 – 563.4]	Effective CO ₂ concentration, ppm	(Forster, Smith et al. 2023)

287 Table 1: Constants and climate driver datasets referenced in Eqs. 6-8, in addition to
 288 temperature baselines. Equations referenced in “Source” column are found in Appendix A
 289 and Supplement A1&A2.

290
 291 Future projections along the shared socioeconomic pathways (SSPs) for the EBM-KF
 292 also require the concentrations of greenhouse gasses including carbon dioxide ($[eCO_2]_t$),
 293 stratospheric aerosol optical depth due to volcanic dust and human emissions (AOD_t), and
 294 reflective flux from anthropogenic clouds (AC_t). ESMs simulate the carbon cycle and thus
 295 find an equivalent of $[eCO_2]_t$ from specified CO₂ and greenhouse gas emissions, but our
 296 EBM-KF does not have this capability. Future greenhouse gas concentrations and
 297 anthropogenic cloud forcings are instead taken from a conversion of anthropogenic fluxes by
 298 the MAGICC7.0 carbon cycle emulator (Meinshausen, Nicholls et al. 2020), as reported by
 299 (Smith, Forster et al. 2021). For instance, SSP1-2.6 and SSP3-7.0 are shown in Figs. 9 & 10,
 300 which flank the most likely result of current environmental policies (Pielke Jr, Burgess et al.
 301 2022). Projection of anthropogenic forcings from Nazarenko et. al. (2022) using the NASA
 302 GISS ESM yield very similar future curves (not shown).

303 Overall, the blind (forward) energy-balance model (orange dashed line in Fig. 2) has 4
 304 yearly forcing inputs ($[eCO_2]_t$, AOD_t , AC_t , $(\frac{G_{SC}}{4})_t$) and 17 irreducible parameters (including 1
 305 inferred exponent η , 4 inferred β coefficients, 3 heat capacities, and 3 reference
 306 temperatures). The time step of this iterative difference equation model is 1 year chosen
 307 arbitrarily to coincide with the calendar year. The deep ocean potential temperature θ_t is
 308 recalculated at each time step from the GMST (T_t) and the OHCA (H_t) by (6), and then
 309 these two terms are updated with (7)-(8). The measured temperature in the year 2002 (Y_{2002})
 310 appears prominently in this model because that was the midpoint of the measurement window
 311 of the CERES satellite (Wielicki, Barkstrom et al. 1996; Loeb, Wielicki et al. 2009), and all
 312 albedo-related feedbacks are expressed relative to these measurements. For this model, the
 313 OHCA (H_t) is calculated in units of W*year/m² on an average of the Earth’s surface, and
 314 then converted to ZJ within the ocean by multiplying by a factor of $11.42 = 3.154e7 \text{ s/year} * 5.101e7 \text{ m}^2 / \text{Earth surface} * 0.71 \text{ ocean/surface}$. This time-step function (6-8) and its partial
 315 derivative (see Appendix A4) will become critical parts of our Kalman Filter: (9, 10) below.
 316

This manuscript has been submitted for publication to JOURNAL OF CLIMATE (AMS). Please note that this manuscript has undergone two rounds of peer review but has yet to be formally accepted for publication. Subsequent versions of this manuscript may differ slightly in content.

317 This blind EBM model had good skill at predicting the GMST with $r^2=0.902$ when
318 compared to the HadCRUT5 GMST timeseries (Morice, Kennedy et al. 2021), and OHCA
319 with $r^2=0.907$ when compared with the inferred history (Zanna, Khatiwala et al. 2019), as is
320 demonstrated by the dashed orange lines in Fig. 3. The blind EBM has a comparably high
321 correlation ($r^2=0.890$) with the 30-year running mean (i.e., the climate normal) of the
322 HadCRUT5 GMST, indicating that this forward energy balance model also has skill in
323 reproducing the climate state as determined by standard approaches, with departures due to
324 volcanic eruptions. Thus, most observed climate change can be explained by the literature-
325 based blind, forward EBM and records of anthropogenic emissions (greenhouse gasses,
326 cloud-seeding tropospheric aerosols) and records of top-of-atmosphere aerosol optical depth
327 (primarily altered by stratospheric aerosol concentrations), consistent with recent forward-
328 EBM applications (Hu and Fedorov 2017; Kravitz, Rasch et al. 2018). The distribution of
329 residuals in the GMST record from either the 30-year running mean or the EBM has small
330 bias and skewness (see Supp. Fig. 9). These residuals' kurtosis is slightly less than Gaussian
331 to accommodate measurement uncertainty, as discussed in Section 3a in relation to Figs. 4 &
332 5. So, the 30-year running mean's "weather" or "noise" empirical probability density
333 function combining residuals and measurement uncertainty is very nearly Gaussian, and thus
334 amenable to treatment by a Kalman filter framework (see section 2b). The Fig. 3 forward
335 model comparisons were made without any assimilated data, illustrating that the EBM
336 physics alone has skill in reproducing aspects of the GMST and OHCA records. Tuning the
337 EBM parameters may further improve skill, but the EBM is only the forward projection
338 component of the data assimilating Kalman Filter hybrid model described in the next section.
339 The combined system is the focus of this paper.

340 *b. EBM-Kalman Filter: A Weighted Average of Energy Balance and Measurements*

341 While similar algorithms were developed in the 1880s by Thorvald Nicolai Thiele
342 (Lauritzen 1981; Lauritzen and Thiele 2002), Kalman filtering rose to prominence due to its
343 use in the Apollo navigation computer as proposed by Ruslan Stratonovich (1959; 1960),
344 Peter Swerling (1959), Rudolf E. Kálmán (1960), Richard S. Bucy (1961), and implemented
345 by Stanley Schmidt (1981). Versions of this statistical filter are universally used in aerospace
346 guidance systems (Grewal and Andrews 2001), aspects of numerical weather prediction
347 (Houtekamer and Mitchell 1998; Kalnay 2002), and recently popularly in climate science as
348 Ensemble Kalman filters (which use a Monte Carlo approximation via simulations in high-

This manuscript has been submitted for publication to JOURNAL OF CLIMATE (AMS). Please note that this manuscript has undergone two rounds of peer review but has yet to be formally accepted for publication. Subsequent versions of this manuscript may differ slightly in content.

349 dimensional space, see below). Ensemble Kalman filters (not to be confused with Extended
350 Kalman filters, the local linearization extension method of this paper described below) have
351 been instrumental to 20th century reanalysis (Compo, Whitaker et al. 2011) and last
352 millennium reanalysis projects (Hakim, Emile-Geay et al. 2016) of global atmospheric
353 circulation. In the Ensemble Kalman Filter, observations sample the full gridded weather
354 patterns (a space with hundreds to millions of dimensions) within an ensemble of ESMs.
355 Despite the success of Ensemble Kalman filters, *Extended* Kalman filters are computationally
356 intractable as the sole data assimilation tool for atmospheric weather patterns (Bouttier 1996)
357 because many local weather processes do not sample from a Gaussian distribution. However,
358 the central limit theorem states that taking the average of many independent non-Gaussian
359 samples will produce a mean that approximates a Gaussian distribution. This is the case for
360 annual GMST (Montgomery and Runger 2013), which is the average of many non-Gaussian
361 regional and daily weather patterns (Quevedo and Gonzalez 2017). Likewise, while annual
362 OHCA is largely constrained by the subtropical pycnocline depth (Newsom, Zanna et al.
363 2023), it too is comprised of numerous regional and seasonal patterns (Hummels, Dengler et
364 al. 2013; Cheng, Trenberth et al. 2017; Huguenin, Holmes et al. 2022). In this case of *global*
365 GMST and OHCA, an Extended Kalman Filter works because both measurement and
366 dynamical noise are approximately Gaussian (by the Central Limit central limit theorem, to
367 be verified in Section 3), and the energy-balance equation (Section 2a) has a continuous and
368 bounded gradient (see Appendix A4), so it can be locally linearized. Careful construction of
369 the EBM with T^2 in the shortwave term and $T^{2.39}$ in the counteracting longwave term in (Eqs.
370 1 & 5) ensures the derivative (Eqs. A37-41) does not change significantly over the relevant
371 range of temperatures [286 – 291]K, $[eCO_2]_t$ effective CO₂ concentrations [278 – 2000] ppm,
372 AOD_t aerosol optical depths [0 - 0.15], and AC_t anthropogenic cloud forcing [-1 – 0] W/m².
373 This approximate linearity means that more complex realizations of the Kalman filter,
374 particularly the Unscented Kalman Filter (Julier and Uhlmann 1997; Wan and Van Der
375 Merwe 2000) are not necessary (see Supplement Section D). This approach has already
376 proven successful using a 1-(spatial)-dimensional (north-south) energy balance model, with
377 time-steps of decades (or longer), and optimized for use in paleoclimate research (García-
378 Pintado and Paul 2018). Thus, for a variety of reasons an EBM-Kalman Filter (EBM-KF) can
379 be built from an Extended Kalman Filter combined with an (annual, 0-spatial-dimensional)
380 Energy Balance Model.

381 In-depth derivations and tutorials for constructing Kalman filters have been published
382 elsewhere (Miller 1996; Lacey 1998; Särkkä 2013; Benhamou 2018; Youngjoo and
383 Hyochoong 2018; Ogorek 2019). Here we describe enough for basic intuition, and we refer
384 readers to Kalnay (2002), page 281, for a more detailed explanation with alternative notation.
385 We use the term “forecast” where other authors use “prior”, and we avoid use of
386 “measurement error” in a manner that would be ambiguous and confusing in this application.
387 Initially, there is some estimated *state vector* (GMST and OHCA within this paper) $\hat{\mathbf{x}}_{t-1}$ and a
388 Gaussian uncertainty envelope around this vector defined by a *state covariance matrix* \mathbf{P}_{t-1} .
389 This *state vector* is transformed (or projected) one year into the future using a *dynamic model*
390 *Jacobian matrix* Φ into a *forecast state* $\hat{\mathbf{x}}_{t|t-1} = \Phi \hat{\mathbf{x}}_{t-1}$, a transformation that may depend on
391 time-varying control parameters u_t . For our climate system this linear projection is extended
392 to the nonlinear function $\hat{\mathbf{x}}_{t|t-1} = \mathbf{F}(\hat{\mathbf{x}}_{t-1}; u_t)$ in (11), which is just the forward energy balance
393 model equations (6)-(8), where u_t represents the collection of climate forcings ($[eCO_2]_t$,
394 AOD_t , AC_t , $(\frac{G_{SC}}{4})_t$). This simple extension to nonlinearity is the meaning of “Extended”
395 Kalman Filter. The *state covariance* is projected to the next year using a local linear
396 approximation Φ_t (Eq. 9) and enlarges by an additional *assumed model error covariance* \mathbf{Q} ,
397 yielding $\mathbf{P}_{t|t-1}$ the *forecast covariance* (Eq. 12). To arrive at a *posterior* (including
398 observations) information a *measurement vector* \mathbf{y}_t is considered (Eq. 13). The probabilistic
399 range of discrepancies between $\hat{\mathbf{x}}_{t|t-1}$ and \mathbf{y}_t is given by the *innovation covariance matrix* \mathbf{S}_t ,
400 which is the sum of $\mathbf{P}_{t|t-1}$ and an *assumed measurement covariance* \mathbf{R} (14). The *posterior*
401 *estimate* of the state $\hat{\mathbf{x}}_t$ is found by taking a weighted average of $\hat{\mathbf{x}}_{t|t-1}$ and \mathbf{y}_t (16), with the
402 weight on \mathbf{y}_t given by $\mathbf{P}_{t|t-1}(\mathbf{S}_t)^{-1}$, a product known as the *Kalman gain* (15). To reflect the
403 greater certainty in the state vector because of this correction, \mathbf{P}_t , the *posterior covariance*
404 *matrix*, is $\mathbf{P}_{t|t-1}$ shrunk by a factor of $(\mathbf{I}$ minus the Kalman gain) per (17). Within the context
405 of climate modeling, this “posterior state estimate” is somewhat analogous to a climate
406 reanalysis product, as both combine observations and models. Within the context of Bayesian
407 probability, the *prior (forecast) distribution* is given by projecting $N(\hat{\mathbf{x}}_{t-1}, \mathbf{P}_{t-1})$ into the future
408 using the Jacobian matrix Φ , which is multiplied by the marginalized likelihood of \mathbf{y}_t to give
409 a *posterior distribution* $N(\hat{\mathbf{x}}_t, \mathbf{P}_t)$. Note that $(\Phi_t)^*$ in (12) below indicates matrix
410 transposition.

$$411 \quad \Phi_t = \left. \frac{\partial \mathbf{F}(\mathbf{x}; u_t)}{\partial \mathbf{x}} \right|_{\mathbf{x}=\hat{\mathbf{x}}_{t-1}} \quad \text{linearization at timepoint } t \quad (9)$$

$$412 \quad \begin{cases} \mathbf{x}_t = \mathbf{F}(\mathbf{x}_{t-1}; u_t) + \mathbf{w}_t & \text{dynamic model, error: } \mathbf{Q} = \text{Cov}(\mathbf{w}_t) \\ \mathbf{y}_t = \mathbf{x}_t + \mathbf{v}_t & \text{weather variability, error: } \mathbf{R} = \text{Cov}(\mathbf{v}_t) \end{cases} \quad (10)$$

$$413 \quad \hat{\mathbf{x}}_{t|t-1} = \mathbf{F}(\hat{\mathbf{x}}_{t-1}; u_t) \quad \text{forecast ("prior") state estimate} \quad (11)$$

$$414 \quad \mathbf{P}_{t|t-1} = \Phi_t \mathbf{P}_{t-1} (\Phi_t)^* + \mathbf{Q} \quad \text{forecast ("prior") covariance} \quad (12)$$

$$415 \quad \mathbf{z}_t = \mathbf{y}_t - \hat{\mathbf{x}}_{t|t-1} \quad \text{innovation residual} \quad (13)$$

$$416 \quad \mathbf{S}_t = \mathbf{P}_{t|t-1} + \mathbf{R}_t \quad \text{innovation covariance} \quad (14)$$

$$417 \quad \mathbf{K}_t = \mathbf{P}_{t|t-1} (\mathbf{S}_t)^{-1} \quad \text{Kalman gain} \quad (15)$$

$$418 \quad \hat{\mathbf{x}}_t = \hat{\mathbf{x}}_{t|t-1} + \mathbf{K}_t \mathbf{z}_t \quad \text{posterior state estimate} \quad (16)$$

$$419 \quad \mathbf{P}_t = (\mathbf{I} - \mathbf{K}_t) \mathbf{P}_{t|t-1} \quad \text{posterior state covariance} \quad (17)$$

420 If \mathbf{y}_t is an indirect measurement of the state vector \mathbf{x}_t , an observation (or emission) matrix \mathbf{H}
 421 further complicates the procedure (details in the references above). Here we consider only
 422 direct "observations" of GMST and OHCA making mapping and interpolation errors implicit
 423 and the observation matrix $\mathbf{H} = \mathbf{I}$.

424 The true climate state \mathbf{x}_t is the 2-entry vector underlying GMST and OHCA, filtering out
 425 weather and internal variability: $\mathbf{x}_t = [T_t, H_t]$. Throughout this paper, [a, b] indicates a 2-
 426 dimensional vector with components a and b, and we use italic symbols to indicate the
 427 climate state vector containing temperature and heat content. The noisy measurements $\mathbf{y}_t =$
 428 $[Y_t, \psi_t]$ are the yearly time series of GMST and OHCA, and $\hat{\mathbf{x}}_t = [\hat{T}_t, \hat{H}_t]$ is the estimate of
 429 the unknown 2-dimensional climate state, expressed in degrees Kelvin and $\frac{W yr}{m^2}$ (convertible
 430 to ZJ by the factor $5.1006 * 3.154 * 0.71 = 11.42$). The energy-balance model \mathbf{F} (10) governing
 431 \hat{T}_t is nonlinear (with T^2 and $T^{2.385}$ terms due to albedo and Planck feedbacks) (Friedrich,
 432 Timmermann et al. 2016), which necessitates some way to handle the nonlinearity: an
 433 Extended Kalman filter, Ensemble Kalman filter, or Unscented Kalman filter are among the
 434 potential nonlinear methods. In our Extended Kalman Filter, the *forecast* state $\hat{\mathbf{x}}_{t|t-1}$ (11) is
 435 given by (6)-(8) above and Φ_t and the *forecast* covariance projection (12) is a time-varying
 436 linearization (Eqs. A21-A25). This energy-conserving difference equation thus resembles a
 437 first-order Taylor series approximation of a differential energy-balance model (if
 438 discretization errors are considered part of the tendency), or the integral form of a
 439 conservative discretization in time (if shortwave and longwave fluxes are taken as a model
 440 for their time-integrated value), and the Kalman Filter re-approximates a GMST and OHCA
 441 climate state every year. The initial estimated state uncertainty is intentionally overestimated

442 at $P_{1850} = \begin{bmatrix} 1K^2 & 1K \frac{W yr}{m^2} \\ 1K \frac{W yr}{m^2} & 20 \left(\frac{W yr}{m^2}\right)^2 \end{bmatrix}$ and then P_t rapidly converges (within 15 years) in the

443 EBM-KF to $P_{1865} = \begin{bmatrix} 0.0017 K^2 & 0.035 K \frac{W yr}{m^2} \\ 0.035 K \frac{W yr}{m^2} & 4.0 \left(\frac{W yr}{m^2}\right)^2 \end{bmatrix}$, and then continues to slowly shrink with

444 time as more accurate measurements are made. For convenience we form confidence
445 intervals for GMST and OHCA climate state by taking twice the square root of the respective
446 diagonal elements of P_t . For clarity, we give both diagonal elements their own symbols, and
447 similarly for S_t , noting that here T as a superscript just labels a scalar value.

448 $[\hat{p}_t^T, \hat{p}_t^H] = \text{diag}(P_t)$ (18a) $[\hat{s}_t^T, \hat{s}_t^H] = \text{diag}(S_t)$ (18b)

449 95% CI GMST state, 1865: $\hat{T}_{1865} \pm 2\sqrt{\hat{p}_{1865}^T} = 286.66K \pm 2\sqrt{0.0017K^2} = 286.66 \pm 0.07K$ (19)

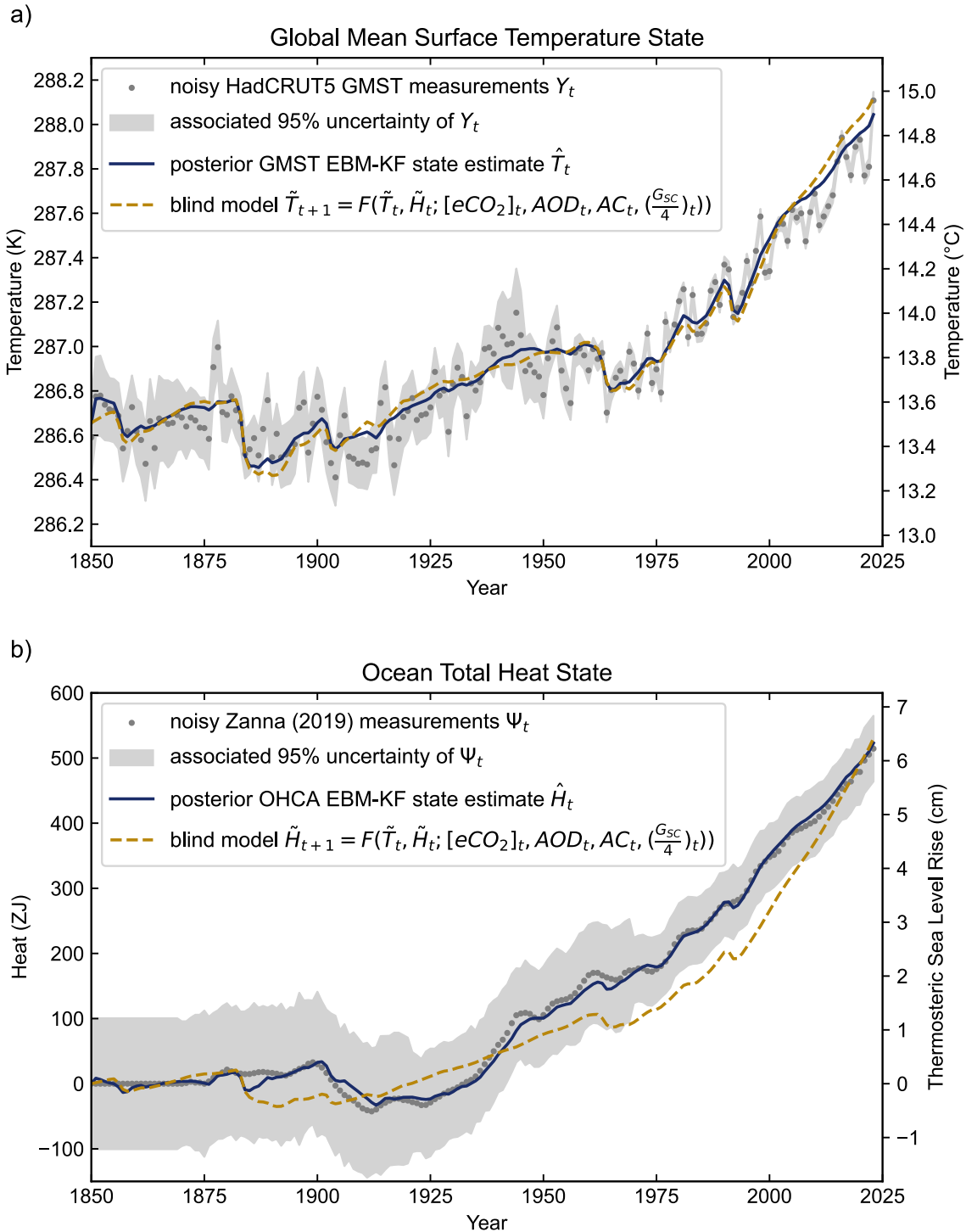
450 Similarly, we use the diagonal elements of S_t to form confidence intervals of next-year
451 measurements about $\hat{x}_{t|t-1}$ (18b). The Extended Kalman Filter implicitly assumes that
452 Gaussian “model” noise is added to this climate state at each time step (10a), and additionally
453 the climate state emits annual “weather variability” from a yet wider Gaussian noise
454 distribution (10b). Whereas we interpret global annual weather to be the noisy measurements
455 $y_t = [Y_t, \psi_t]$, “weather variability” is observed via *innovation residuals* z_t . These *innovation*
456 *residuals* have components $[z_t^T, z_t^H] = z_t$, and the Kalman Filter expects them to come from
457 an unbiased Gaussian noise distribution with covariance S_t (not R_t because the Kalman Filter
458 does not have knowledge of the true climate state x_t .)

459 $z_t^T = Y_t - \hat{T}_{t|t-1}$ (20a) $z_t^H = \psi_t - \hat{H}_{t|t-1}$ (20b)

460 The EBM-KF climate state \hat{x}_t and state covariance P_t only access information from
461 the measurements taken prior to and at year t : $\{y_{1850}, y_{1851}, \dots, y_t\}$. This past-to-present
462 Kalman Filter (Eqs. 9-17) can be further extended into a RTS smoother (Rauch, Tung et al.
463 1965) by additional steps (see Supp. Section A3), which meld information from all
464 measurements in the time window $\{y_{1850}, y_{1851}, \dots, y_{2023}\}$ into each re-estimated posterior
465 state \hat{x}_t and posterior state covariance \hat{P}_t by running backward from the latest EBM-KF state
466 estimates (\hat{x}_{2023} and P_{2023}). In the 1850 to present application, this extension has little effect
467 on \hat{x}_t (Supp. Fig. 2), but there is greater certainty in the smoothed state. Defining

468 $\text{diag}(\hat{P}_t)=[\hat{p}_t^T, \hat{p}_t^H]$, for the GMST uncertainty $\hat{p}_t^T \approx 2.25 * \hat{p}_t^T$, and for the OHCA uncertainty
469 $\hat{p}_t^H \approx 2.84 * \hat{p}_t^H$.

470 In summary, the Extended Kalman Filter projects forward one year into the future
471 based on the unbalanced fluxes of the energy balance model equation, and then takes a
472 weighted average of this projection with the annual GMST measurement (the data
473 assimilation increment). Thus, even though the EBM conserves energy (by construction), the
474 combined EBM-KF does not, unlike other alternative data assimilation approaches (Wunsch
475 and Heimbach 2007). The state estimates from this EBM-KF (in navy blue in Fig. 3) often lie
476 between the blind EBM (in dashed orange in Fig. 3) and the annual temperature
477 measurements (scattered gray dots in Fig. 3), a corrective effect that can be seen most clearly
478 within the GMST measurements in Fig. 3a from 1900 to 1945 and within the OHCA
479 measurements in Fig. 3b from 1940 to 1970. It is possible for the EBM-KF state estimates to
480 escape these bounds for a short time, for instance from 1945 to 1950 in Fig. 3a or after 2007
481 in Fig 3b. These “escape periods” may reflect bias in the measurements, such as warm-biased
482 WWII-era measurements of (sea) surface temperature (Chan and Huybers 2021), or the bias
483 of the Zanna et al. (2019) OHCA product to indicate less heat uptake since 2005 than all but
484 1 of 19 other OHCA estimates (Gulev, Thorne et al. 2021). Both the “blind” EBM predictions
485 $[\tilde{T}_{t+1}, \tilde{H}_{t+1}] = \mathbf{F}(\tilde{T}_t, \tilde{H}_t; u_t)$ where u_t represents the 4 climate forcings, and EBM-KF state
486 estimates $\hat{x}_t = [\hat{T}_t, \hat{H}_t]$ dip down with each major volcanic eruption within the AOD record
487 (see Fig. 11 in the Discussion, Section 4). These volcanic dips are far more pronounced for
488 the GMST component than for OHCA (see Fig. 3) and are present only as flat spots in the
489 deep ocean potential temperature curve (see Supp. Fig. 11).



490

491 Fig. 3: Behavior of the EBM-KF state in relation to blind EBM projections and the stochastic
 492 measurements of GMST and OHCA. Panel a) shows GMST prediction and b) the OHCA
 493 prediction. The blind model (dashed orange) and Kalman Filter state estimate (navy blue) use
 494 EBM dynamics to project from the previous state to the current state, but the state estimate
 495 also assimilates observations (grey dots; GMST from HadCRUT5 (Morice, Kennedy et al.
 496 2021) and OHCA from Zanna et al. (2019)). Incorporation of these observations makes only
 497 small modifications to the EBM-KF's GMST state in a), whereas in b) there is an impressive
 498 difference between the blind EBM's OHCA projections and the EBM-KF's OHCA state - the
 499 latter sticks close to observations.

500

501 *c. Selection of Model Uncertainty and Time-Varying Measurement Uncertainty*

502 Fig. 3 also demonstrates the accuracy associated with each of the temperature
503 measurements. The uncertainty in the climate state P_n automatically responds to unexpected
504 values of the measured temperature (Wunsch 2020). The HadCRUT5 GMST decreases in
505 reported measurement standard deviation from 0.079K in the 1850-1879 window to 0.017K
506 in the 1990-2019 window (Morice, Kennedy et al. 2021), a 78% reduction primarily
507 reflecting a lack of observations in the Southern hemisphere before the satellite age. The
508 inferred deep ocean heat content taken primarily from a hybrid model-observation
509 reconstruction (Zanna, Khatiwala et al. 2019) has a very wide confidence interval before the
510 introduction of modern sampling methods in the 1970s. We use the Zanna et al. (2019)
511 hybrid product due to its long duration of OHCA estimates (based on surface forcing in early
512 years) rather than the shorter direct measurement products (Ishii, Fukuda et al. 2017),
513 although both could be assimilated simultaneously within EBM-KF if desired (as discussed in
514 Section 4c). The additional increase in OHCA after 2018 was provided from a separate NCEI
515 dataset (Levitus, Antonov et al. 2017). Our EBM-KF incorporates these known physical
516 measurement uncertainties in the HadCRUT5 measurements of GMST and the OHCA
517 reconstruction as R_t^{var} . The total assumed measurement covariance R_t (in Eq. 14) is
518 composed of two components: the time-varying physical measurement uncertainty R_t^{var} , and
519 the constant uncertainty R^{const} reflecting internal variability due to dynamical chaos:
520 primarily ENSO and other climate oscillations with limited predictability. Both forms of
521 measurement noise are added onto the underlying climate signal via the random vector \mathbf{v}_t to
522 generate annual observations (see Eq. 10). We assume that R_t^{var} is diagonal and simply sum
523 the two variance matrices to obtain a time-varying value:

$$524 \quad R_t = R_t^{var} + R^{const} \quad (21)$$

525 The realization of the EBM-KF shown in Fig. 2 also has a measurement uncertainty
526 R^{const} that is constant in time and based on the [HadCRUT5's GMST, Zanna (2019) OHCA]
527 residual co-variance with respect to their 30-year running means. In other words, we
528 computed:

$$529 \quad R^{const} = \text{Cov}(\mathbf{y}_t - 30\bar{\mathbf{y}}_t) = \begin{bmatrix} 0.01107 \text{ K}^2 & 0.04627 \text{ K} \frac{\text{W yr}}{\text{m}^2} \\ 0.04627 \text{ K} \frac{\text{W yr}}{\text{m}^2} & 1.17278 \left(\frac{\text{W yr}}{\text{m}^2}\right)^2 \end{bmatrix} = 30 * \mathbf{Q} \quad (22)$$

This manuscript has been submitted for publication to JOURNAL OF CLIMATE (AMS). Please note that this manuscript has undergone two rounds of peer review but has yet to be formally accepted for publication. Subsequent versions of this manuscript may differ slightly in content.

530 The assumed model covariance, Q (see Eq. 12), is set to $R^{const}/30$ to emulate the 30-year
531 running average definition of climate state (Guttman 1989), thus we assume that the random
532 noise contained within the climate model has a variance that is $1/30^{\text{th}}$ as large as the variance
533 in the “weather” measurements. By this simple method, the data-assimilating EBM-KF is
534 tuned to match the “standard climate normal”, as any 30-member sample average has a
535 variance $1/30^{\text{th}}$ as large as the annual measurements’ variance (assuming yearly anomalies are
536 uncorrelated). Variance in these annual measurements arises due to chaos within the climate
537 system, so this R^{const} contribution to the model and measurement uncertainty would exist
538 even if all measurements could be made with arbitrary accuracy.

539 *d. Non-Gaussian Future Projection and Sampling of Volcanic Activity*

540 The EBM-KF can project one year into the future, given greenhouse gas and aerosol
541 concentrations, without any new measurements using only the forward model to obtain
542 *forecast* estimates (11)-(12). To project farther into the future, the *posterior* state and
543 *posterior* covariance are set equal to the *forecast* state and *forecast* covariance, i.e., a
544 *posterior* unaffected by any new observations: $\hat{\mathbf{x}}_t = \mathbf{F}(\hat{\mathbf{x}}_{t-1})$ and $\mathbf{P}_t = \Phi_t \mathbf{P}_{t-1} (\Phi_t)^T + \mathbf{Q}$. While
545 these far-future state estimates behave equivalently to a blind model, the covariance grows
546 over time, either sub-linearly or exponentially (see Section 3d).

547 While the SSPs are used for most forcing variables, future volcanic eruptions require
548 modeling as well. Volcanic eruptions determining AOD_t are inherently stochastic, but the
549 time intervals between eruptions can be approximated using exponential distributions (Papale
550 2018). In standard ESM SSPs, future volcanism is usually included by a steady “background”
551 volcanism, neglecting volcanism’s intermittency and the associated exponential distributions.
552 Even though the EBM-KF assumes Gaussian error and thus cannot include exponential
553 distributions in the same way as measurement and internal chaotic variability, it is so
554 computationally inexpensive that it can be rerun to sample over complex non-Gaussian
555 distributions. This ability to include future volcanoes illustrates a major advantage of this
556 system: thousands of future scenario inputs can be generated and utilized within minutes on a
557 laptop, while each ESM of the LENS2 ensemble took over a week to run on a supercomputer
558 (roughly a billion times more effort in core-hours per ensemble member) which limits the
559 ensemble size and thus motivates using only a background constant level of volcanism. No
560 single exponential distribution fits well to the observed series of volcano eruption intervals,
561 so an exponential mixture with two components was found to be the best fit to the data using

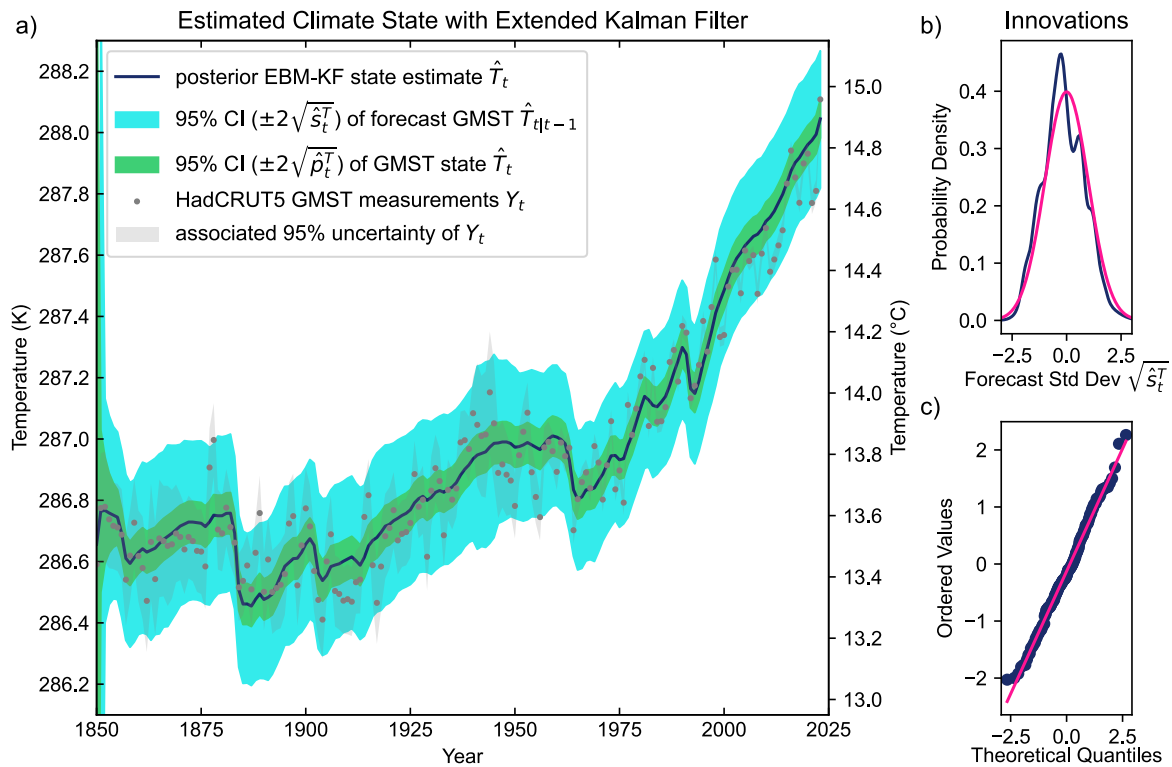
562 the decomposed normalized maximum likelihood (Okada, Yamanishi et al. 2020). See

563 Appendix B for further details.

564

565 3. Results

566 a. Examination of the EBM-KF Climate State (1850-Present)



567 Fig. 4: EBM-KF and associated uncertainties. a) The EBM-KF climate state estimate (navy
 568 blue line) is drawn with a 95% or *extremely likely* confidence interval (light green area) of its
 569 posterior uncertainty $\pm 2\sqrt{\hat{s}_t^T}$. Annual-mean HadCRUT5 GMST measurements are
 570 assimilated (gray dots and gray area mostly within the light blue). A 95% confidence interval
 571 (CI) in light blue indicates the forecast uncertainty $\pm 2\sqrt{\hat{s}_t^T}$. b) The Gaussian mixture of
 572 innovations z_t^T (deviations between measurements minus Y_t the projected climate state $\hat{T}_{t|t-1}$)
 573 with each year's associated measurement uncertainty (navy blue), normalized onto a
 574 horizontal axis labeled with standard deviations $\sqrt{\hat{s}_t^T}$ of the ideal forecast covariance
 575 (pink). c) Quantile-quantile plot of these normalized innovations ($z_t^T / \sqrt{\hat{s}_t^T}$). All panels
 576 demonstrate that the gray HadCRUT5 GMST observations appropriately fill out the 95% CI
 577 of the forecast uncertainty (light blue) around the EBM-KF state estimate (navy blue).
 578
 579

580 A primary product of this paper is the EBM-KF climate state, spanning from 1850 to
 581 present. Recall that the forward EBM uses published literature values: this is not an empirical

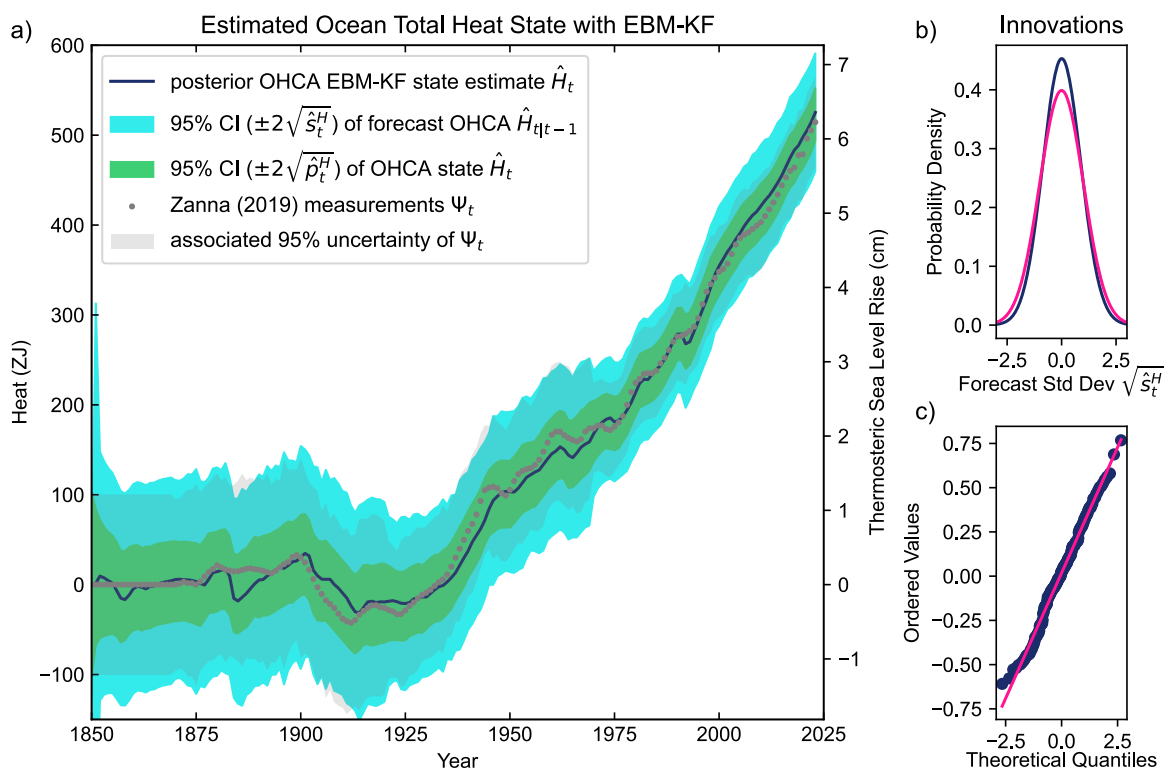
This manuscript has been submitted for publication to JOURNAL OF CLIMATE (AMS). Please note that this manuscript has undergone two rounds of peer review but has yet to be formally accepted for publication. Subsequent versions of this manuscript may differ slightly in content.

582 fit to GMST and OHCA data, but rather the EBM-KF assimilates these data. We first
583 examine the GMST component \hat{T}_n of the Kalman-Filtered climate state $\hat{\mathbf{x}}_n$. There are two
584 distinct Gaussian distributions relevant to understanding our method: the uncertainty in the
585 current GMST *climate state*, as graphed in narrow green envelope in Fig. 4a, and the
586 uncertainty window of possible next-year (forecast) GMST measurements, as graphed in the
587 light blue wider envelope in Fig. 4a. Further examination of the “*update*” difference (from
588 $\mathbf{K}_t \mathbf{z}_t$ in Eq. 16) of the posterior estimated states minus forecast states ($\hat{T}_t - \hat{T}_{t-1}$) reveals that
589 in any individual year after 1855, assimilation of the GMST measurement only shifts the
590 forecast GMST state projection \hat{T}_{t-1} by $-0.001 \pm 0.009 \text{K/yr}$ (\pm standard deviation), range $[-$
591 $0.020 - 0.022] \text{K/yr}$. This *update* value is miniscule compared with the GMST adjustment in
592 \tilde{T}_n from the blind, forward EBM contribution of forced climate state change of
593 $+0.025 \pm 0.027 \text{K/yr}$ since 1975, and $+0.002 \pm 0.027 \text{K/yr}$ from 1850 to 1975, while the forecast
594 change can be as large as $[-0.191 - 0.053] \text{K}$ in a single year.
595 However, as shown in Fig. 3, repeated small *updates* in the same direction (due to repeatedly
596 lower or higher than expected GMST measurements) can drift \hat{T}_t away from the blind model
597 estimate \tilde{T}_t . This “*accumulated correction*” ($\hat{T}_t - \tilde{T}_t$) is $+0.004 \text{K}$ on average, and as much as
598 $[-0.086 - 0.096] \text{K}$ (after 1885: $+0.02 \text{K}$ range $[-0.086 - 0.062] \text{K}$). *Accumulated corrections*
599 are 3-4 times larger in extreme than the most extreme *updates*, indicating that these *updates*
600 had accumulated over >4 years prior to 1886 and 2022 (~ 5 and ~ 8 years respectively, see Fig.
601 3a). Note the mean *accumulated correction* is slightly positive while the mean *update* is
602 slightly negative because of the influence of OHCA corrections (see below and Fig. 3b). The
603 EBM-KF state \hat{T}_t is still very highly correlated with the blind, forward EBM \tilde{T}_n ($r^2=0.992$).
604 Measurements Y_t have nearly equal warming and cooling contributions to the underlying \hat{T}_t
605 climate state, forming the expected Gaussian distribution of normalized *innovations*
606 ($z_t^T / \sqrt{\hat{\mathbf{s}}_t^T}$) as demonstrated over the entire timeseries in Fig 4b and in every full 50-year
607 period in Supp. Fig. 12. The GMST observations since 2000 slightly cool the EBM (Supp.
608 Fig. 12d,h) indicating that the EBM may have oversized positive climate feedbacks, an issue
609 which could be rectified with parameter adjustment (Section 4c).

610 After an initial convergence period of about a decade, the green 95% CI of the GMST
611 state uncertainty $2\sqrt{\hat{\mathbf{p}}_t^T}$ slightly shrinks from $\pm 0.067 \text{K}$ in the 1870s to $\pm 0.062 \text{K}$ since 1980, a
612 reduction of -7.5%. The 95% CI of forecast uncertainty, from $2\sqrt{\hat{\mathbf{s}}_t^T}$, is drawn in light blue
613 around the forecast estimated GMST state projection \hat{T}_{t-1} , showing where the Kalman Filter

614 expects the subsequent year's temperature measurement to be. This forecast uncertainty
615 converges from roughly $\pm 0.26\text{K}$ in the 1870s to $\pm 0.223\text{K}$ since 1980. Both reductions reflect
616 the improvement in the GMST component of the time-varying measurement uncertainty,
617 R_t^{var} , with modern satellite observations. But these reductions are modest compared to the
618 76% reduction in time-varying HadCRUT5 measurement uncertainty over the same period
619 because the EBM-KF is also assuming time-invariant climate process uncertainty, Q and the
620 associated R^{const} . The empirical projection probability distribution (a Gaussian mixture of all
621 measurement uncertainties relative to the EBM-KF forecast distribution) and an ideal
622 Gaussian distribution closely match (Fig. 3b), confirming that the annual measurements of
623 GMST can be interpreted as Gaussian noise around an underlying climate state. The quantile-
624 quantile plot (Fig. 3c) demonstrates this same finding, just using gray points of innovations
625 (z_t^T the difference between EBM-KF forecasts $\hat{T}_{t|t-1}$ and measurements Y_t) rather than each
626 innovation being a distribution (with variance from R_t^{var}) as in Fig. 3b. Each innovation point
627 is normalized to the forecast uncertainty ($z_t^T / \sqrt{\hat{S}_t^T}$), and then these are sorted from lowest to
628 highest and plotted on the vertical axis. Along the horizontal (theoretical quantiles) axis, the
629 percentile of each innovation is plotted where it would lie on an ideal Gaussian distribution,
630 showing the real GMST “weather” measurements from HadCRUT5 are distributed around
631 the EBM-KF GMST climate state in precisely the expected Gaussian distribution.

632 As we hoped, the EBM-KF GMST climate state estimate over 1850 to present is not
633 substantively different from the 30-year running average except for the impact of major
634 volcanoes (see Fig. 10a, $r^2=0.923$), thus $\hat{T}_t \approx \overline{Y}_t$ in non-volcano years. The LENS2
635 hindcasts depart from both in the interval from 1940 – 2000 (see Fig. 10a) causing a lower
636 $r^2=0.906$ over all 174 years between EBM-KF and LENS2. The EBM-KF with unfiltered
637 volcanic forcing can thus be interpreted as a middle ground between the 30-year running
638 average and a LENS2 ensemble average (which are farther apart with $r^2=0.820$). The
639 performance of the GMST and OHCA portions of EBM-KF model do vary; the most
640 noticeable biases (see Fig. 3) are that the blind OHCA is significantly corrected toward the
641 Zanna et al. (2019) reconstruction of OHCA from 1875-2005 (assimilation of this data
642 reconstruction continues through 2018), but these correction periods are not evident as
643 persistent biases in the EBM-KF (Fig. 5). Forward model biases may be ameliorated by
644 automated, optimized tuning of parameters. This is addressed in Section 4c and is well-
645 studied in Kalman filter applications (Zhang and Atia 2020); the potential adoption of these
646 tools to climate science is a key advantage of the EBM-KF hybrid.



647

648 Fig. 5: EBM-KF state estimate (navy blue) for deep ocean OHCA in units of mean potential
 649 temperature from the same EBM-KF run as in Fig. 3. 95% CI of forecast estimate is drawn in
 650 light blue, and posterior 95% CI is drawn in green. Annual-mean Zanna et al. (2019)
 651 reconstructions are assimilated (gray dots and gray area almost entirely within the light blue).
 652 Other panels and colors as in Fig. 4. All panels demonstrate that the uncertainty window of
 653 the assimilated OHCA data (gray) closely corresponds to the 95% CI of the
 654 forecast uncertainty (light blue) around the EBM-KF state estimate (navy blue).

655 Fig. 5 shows the deep OHCA component of the EBM-KF and its associated
 656 uncertainties. While the OCHA measurements from the Zanna et al. (2019) hybrid product
 657 are more autocorrelated than the HadCRUT5 GMST (relatively less year-to-year variability),
 658 the innovations for OHCA are again approximately Gaussian (panels 5b, 5c). In the context
 659 of this empirical probability distribution, each member of the Gaussian mixture has a larger
 660 gray window given by the time-varying measurement uncertainties R_t^{var} from the OHCA
 661 measurements. In simpler language, the light blue forecast window is large because it must
 662 encapsulate the gray measurement uncertainty window, which moves around within it. To
 663 achieve the nearly Gaussian empirical probability distribution in panel 5b, it is unsurprising
 664 that most EBM-KF estimated states are pulled very close to the autocorrelated OHCA
 665 measurements in Figs. 5a & 3b. This is a situation dominated by measurement uncertainty
 666 R_t^{var} , which is different than observable dynamic “weather variability” (innovations z_t^T)

This manuscript has been submitted for publication to JOURNAL OF CLIMATE (AMS). Please note that this manuscript has undergone two rounds of peer review but has yet to be formally accepted for publication. Subsequent versions of this manuscript may differ slightly in content.

667 filling the full forecast distribution (light blue) in Fig. 4a. As a result, the OHCA component
668 of the EBM-KF pays much more attention to these measurements ψ_t than relying mostly on
669 the blind EBM (see Fig. 3b). This *updates* the OHCA state estimate ($\hat{H}_t - \hat{H}_{t-1}$) after 1855
670 by 0.05 ± 3.72 ZJ/yr, range $[-8.16 - 9.78]$ ZJ/yr; comparable with the OHCA change in \tilde{H}_t from
671 the blind, forward EBM contribution 3.07 ± 5.30 ZJ/yr, up to $[-25.31 - 14.72]$ ZJ/yr.
672 Unsurprisingly, the EBM-KF takes a substantially different track than the blind EBM,
673 yielding an *accumulated correction* of up to +91.6ZJ in 1998. Reflecting this improvement in
674 measurement accuracy (as incorporated via R_t^{var}), the OHCA components of both state
675 uncertainty $2\sqrt{\hat{p}_t^H}$ and forecast uncertainty $2\sqrt{\hat{s}_t^H}$ shrinks dramatically over the 174-year run.
676 $2\sqrt{\hat{p}_t^H}$, the envelope for the OHCA climate state estimate, has a very slow initial convergence
677 that reaches ± 45.1 ZJ by 1865 and then gradually falls to ± 29.4 ZJ by 2000, a 35% decrease.
678 $2\sqrt{\hat{s}_t^H}$, the 95% forecast envelope for OHCA, drops from ± 115.0 ZJ by 1865 to ± 66.2 ZJ by
679 1970 (42% decrease) and then remains near this value through the present, range $[\pm 63.4 -$
680 $\pm 71.2]$. This reduction in forecast uncertainty directly reflects a 48% decrease in the
681 uncertainty from the Zanna et al. (2019) hybrid product over the equivalent time period.

682 *b. Using the EBM-KF to determine Policy Threshold Crossing*

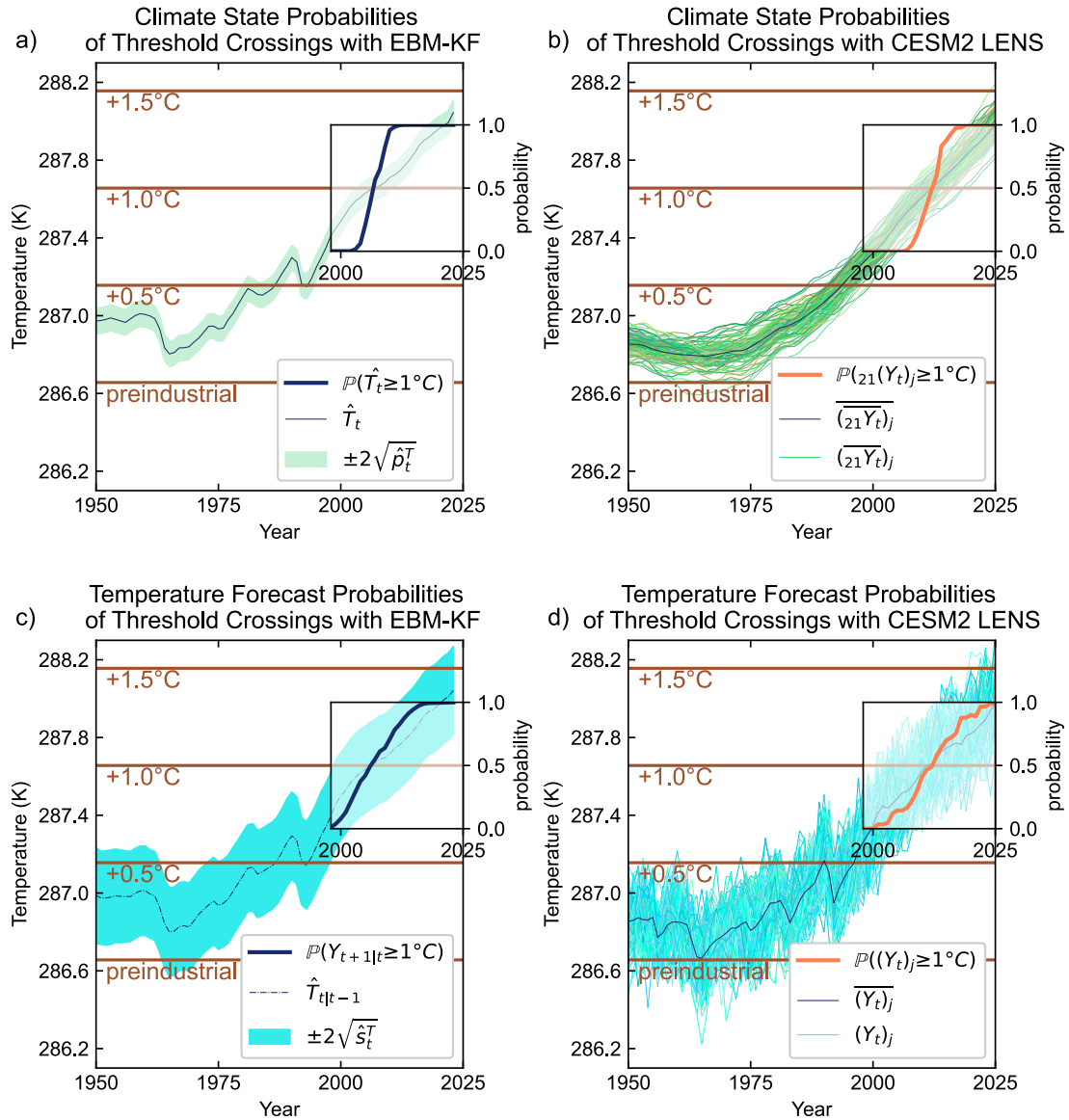
683 A single GMST measurement is not an accurate measurement of anthropogenic
684 climate change due to the large internal variability of the system, and so a single annual
685 temperature above a particular policy threshold is not a guarantee of the climate state crossing
686 that threshold. One interpretation of “crossing” is when the climate state underlying GMST
687 (e.g. the “standard climate normal”, or 30-year running mean of GMST) is determined with a
688 given probability to have passed a policy threshold. This “climate state above” the threshold
689 definition was used by Tebaldi and Knutti (2018) for regional thresholds and the IPCC AR6
690 (Lee, Marotzke et al.) who state “the time of GSAT exceedance is determined as the first year
691 at which 21-year running averages of GSAT exceed the given policy threshold.”¹ A second
692 interpretation would be the chance that next year’s annual-mean GMST will exceed the
693 policy threshold, or “annual temperature forecast above” the threshold. The EBM-KF

¹ We use a 30-year averaging window nearly everywhere, but for consistency with these practices we use a 21-year averaging window for raw ESM simulations (only in Fig. 6b and Fig 12a-e). The EBM-KF climate state covariance is chosen to reflect the uncertainty in the 30-year average of real-world GMST (see Section 2c)—using R^{const} and Q matrices reflecting the 21-year means to match the IPCC definition would be a trivial modification.

694 generates probability distributions for both the “climate state above” and the “annual
695 temperature forecast above” interpretations of whether a policy threshold has been crossed.

696 This climate state threshold, as in the IPCC definition, is given in the EBM-KF by a
697 Gaussian distribution (green in Fig. 6a) about the state \hat{T}_t with a variance \hat{p}_t^T . The IPCC has
698 an ensemble of models to draw upon over both the historical period and future projections
699 (including those from LENS2 in Fig. 6b), so the fraction of the climate states (21-year means)
700 of each (j) of the ensemble members ($\overline{{}_{21}Y_t}$) _{j} found above a given policy threshold
701 determines the overall probability that the climate policy threshold was crossed (see Fig. 6d).
702 Within our notation, we reuse Y_t to represent a GMST timeseries, but with the additional j
703 subscript this timeseries is indicated to be the j^{th} LENS2 hindcast, not a historical record. This
704 empirical approach assumes the ensemble spread is a good representation of GMST
705 uncertainty – yet recent IPCC reports discount the 90% ensemble spread to a 66% confidence
706 range because coarse climate models under-represent internal variability and model
707 uncertainty (Collins, Knutti et al. 2013; Lee, Marotzke et al.). The EBM-KF does not require
708 a future projection to arrive at a present-day climate state, because it already provides an
709 instantaneous and continual estimate of \hat{T}_t . The uncertainty $2\sqrt{\hat{p}_t^T}$ around the *posterior*
710 climate state \hat{T}_t is used to calculate the probability of threshold crossing (see Fig. 6a) as
711 follows: The probability of the climate state exceeding the policy threshold q is the integral of
712 the probability density of the GMST climate state above q , equivalently 1 minus the
713 integrated probability below q . The Gaussian cumulative distribution function centered at \hat{T}_t
714 with variance set to \hat{p}_t^T , evaluated at q , is this cumulative probability below the threshold.

715
$$\mathbb{P}(\hat{T}_t \geq q) = 1 - \text{CDF}_{\mathcal{N}(\hat{T}_t, \hat{p}_t^T)}(q) = \frac{1}{2} \left(1 + \text{erf} \left(\frac{\hat{T}_t - q}{\sqrt{2 \hat{p}_t^T}} \right) \right) \quad (23)$$



716

717 Fig. 6a: EBM-KF and climate state crossing policy thresholds: As in Fig. 4, there are the
 718 EBM-KF GMST state estimate (navy blue line) \hat{T}_t , 95% CI of the climate state (light green)
 719 $\pm 2\sqrt{\hat{p}_t^T}$, and GMST measurements (gray dots) Y_t . Additionally, policy thresholds (brown
 720 lines) are shown at 286.7K (+0°C), 287.2K (+0.5°C), and 287.7K (+1.0°C), compared to the
 721 preindustrial baseline. One inset axis indicates the +1°C), threshold crossing probability, with
 722 a y-axis of cumulative probability (thick navy blue; from 0 to 1) and the x-axis in time
 723 (years). Fig. 6b: each of the 21-year running means of the LENS2 ensemble is plotted in
 724 green, along with the ensemble-average in black. Individual LENS2 ensemble members are
 725 symbolized $(Y_t)_j$ with the subscript j indicating that this GMST timeseries is a hindcast
 726 simulation. The fraction of these running means above the +1°C policy threshold is plotted
 727 within the inset probability axis. Fig. 6c: The projected GMST “weather” 95% CI: $\pm 2\sqrt{\hat{s}_t^T}$
 728 is shown in light blue around the forecast EBM-KF GMST state estimate (navy blue dashed-
 729 dotted line) $\hat{T}_{t|t-1}$. Actual annual GMST measurements (gray dots) Y_t are also shown. The
 730 inset axis indicates the likelihood that the actual GMST measurement will be above the
 731 +1°C), particular policy threshold based on this projection, a y-axis of cumulative probability
 732 (purple; from 0 to 1) and the x-axis in time (years). Fig. 6d: each of the LENS2 ensemble
 733 members is plotted as a blue or green line, along with the ensemble-average in dark blue. The

734 fraction of these members with annual GMST above the +1°C weather threshold is plotted
735 within the inset probability axis.

736
737

738 For the second interpretation of temperature forecast above the policy threshold, the
739 EBM-KF predicts a relevant window (blue in Fig. 6c) of possible next-year GMST
740 measurements. This EBM-KF window is a Gaussian distribution centered at the projected
741 state $\hat{T}_{t|t-1}$ (dashed dark blue line) with a variance $\hat{\sigma}_t^T$: in other words, a simulated draw from
742 the *forecast* state. This uncertainty range reflects and encapsulates actual annual GMST
743 measurements, not the uncertainty in the climate. For an ensemble of ESMs, the analogous
744 temperature forecast probability is the fraction of unfiltered individual ensemble members
745 $(Y_t)_j$ at year t that are warmer than the policy threshold (blue lines in Fig. 6d).

746
747

748 There is additional ambiguity regarding whether “crossing a policy threshold” should
749 specify an instant or a brief period. Here we define (based on the 1σ confidence interval, or
750 the *likely* range in IPCC terminology) the “policy threshold crossing period” to span from the
751 earliest year when $\geq 15.9\%$ of climate states or temperature forecasts exceed the policy
752 threshold to the latest year when $\leq 84.1\%$ of climate states or temperature forecasts exceed
753 that policy threshold. A “policy threshold crossing instant” is the year when the probability of
754 exceeding the policy threshold is nearest to 50% while continuing to increase (or *as likely as*
755 *not* to have crossed the policy threshold in IPCC terminology).

756 Regardless of whether an ESM ensemble (see Fig. 6b,d) or EBM-KF (see Fig. 6a,c) is
757 used, the temperature forecast above threshold period (Fig. 6c,d) has a longer duration than
758 the climate state above period (Fig. 6a,b) because the uncertainty/ensemble spread in the
759 annual forecasts is wider than the uncertainty/ensemble spread of the time-averaged states.
760 Both ESM ensemble and EBM-KF methods report similar policy threshold crossing instants
761 (Fig. 11). Interestingly, the Mt. Pinatubo eruption in 1991 resets the +0.5K threshold crossing
762 repeatedly in both the EBM-KF and ESM ensemble by its perturbation of elevated aerosols.

763 Fig. 6 quantifies the probability of crossing policy thresholds as a function of time
764 (dark blue or orange), inset on top of the relevant GMST timeseries and spread. The EBM-
765 KF climate state estimate in Fig. 6a and annual temperature forecast in Fig. 6c are aligned by
766 year, although these two quantities are in entirely different probability domains. As the EBM-
767 KF state estimate approaches any given policy threshold, the cumulative temperature policy
768 threshold approaches 0.5, or 50% at a “policy threshold crossing instant”. The +1.0K policy

This manuscript has been submitted for publication to JOURNAL OF CLIMATE (AMS). Please note that this manuscript has undergone two rounds of peer review but has yet to be formally accepted for publication. Subsequent versions of this manuscript may differ slightly in content.

769 threshold's crossing instant was in 2010. For the annual temperature forecast in Fig. 6c, the
770 crossing period was 2003-2015 for +1.0K. The crossing period for the climate state in Fig. 6a
771 is briefer: 2008-2012 for +1.0K. For comparison using LENS2 the analogous climate state
772 thresholds are plotted in Fig. 6b,d, although these do not precisely align temporally due to the
773 cold bias of LENS2 during this decade. All threshold crossing periods and instants including
774 future projections under SSP3-7.0 are compared directly in Fig. 12.

775 *c. The spread from one member – using EBM-KF to generate an analog for an ESM large*
776 *ensemble spread*

777 There are many more past and future climate scenarios that researchers wish to
778 investigate than there are computational resources to run a full large ensemble for each
779 scenario. Fortunately, the EBM-KF allows for one or a handful of ESM simulations to
780 approximate the distribution of an entire ensemble spread (similar to an approach taken for
781 ensembles of ice sheet models in (Edwards, Nowicki et al. 2021; van Katwyk, Fox-Kemper et
782 al. 2023)). There are inter-annual differences which persist between runs of the ensemble and
783 skew some climate states persistently cooler and others warmer (Supp. Fig. 6), an effect not
784 captured by a Kalman filter framework.

785 Figure 7a shows the comparison between the EBM-KF GMST climate state
786 uncertainty distribution (light green) and the LENS2 time-Filtered ensemble members. This
787 time-Filtering was performed using the same EBM-KF, momentarily assuming that one of
788 the ensemble members' hindcast was the actual measured temperature record. Each of the
789 orange lines is a climate state central estimate that is comparable to the blue line of the real
790 observed GMST climate state. Sometimes the observations' EBM-KF climate state
791 uncertainty distribution contains the time-Filtered LENS2 ensemble members, such as in
792 1900 and 1935, but at other times it does not, such as in 1950. In corresponding panels within
793 Supp. Fig. 14, we show the histogram Supp. Fig. 14a and quantile-quantile comparison Supp.
794 Fig. 14b: both demonstrating a clear bias. This is what it means to say that the LENS2
795 climate state disagrees with the observed climate state within the EBM-KF framework.

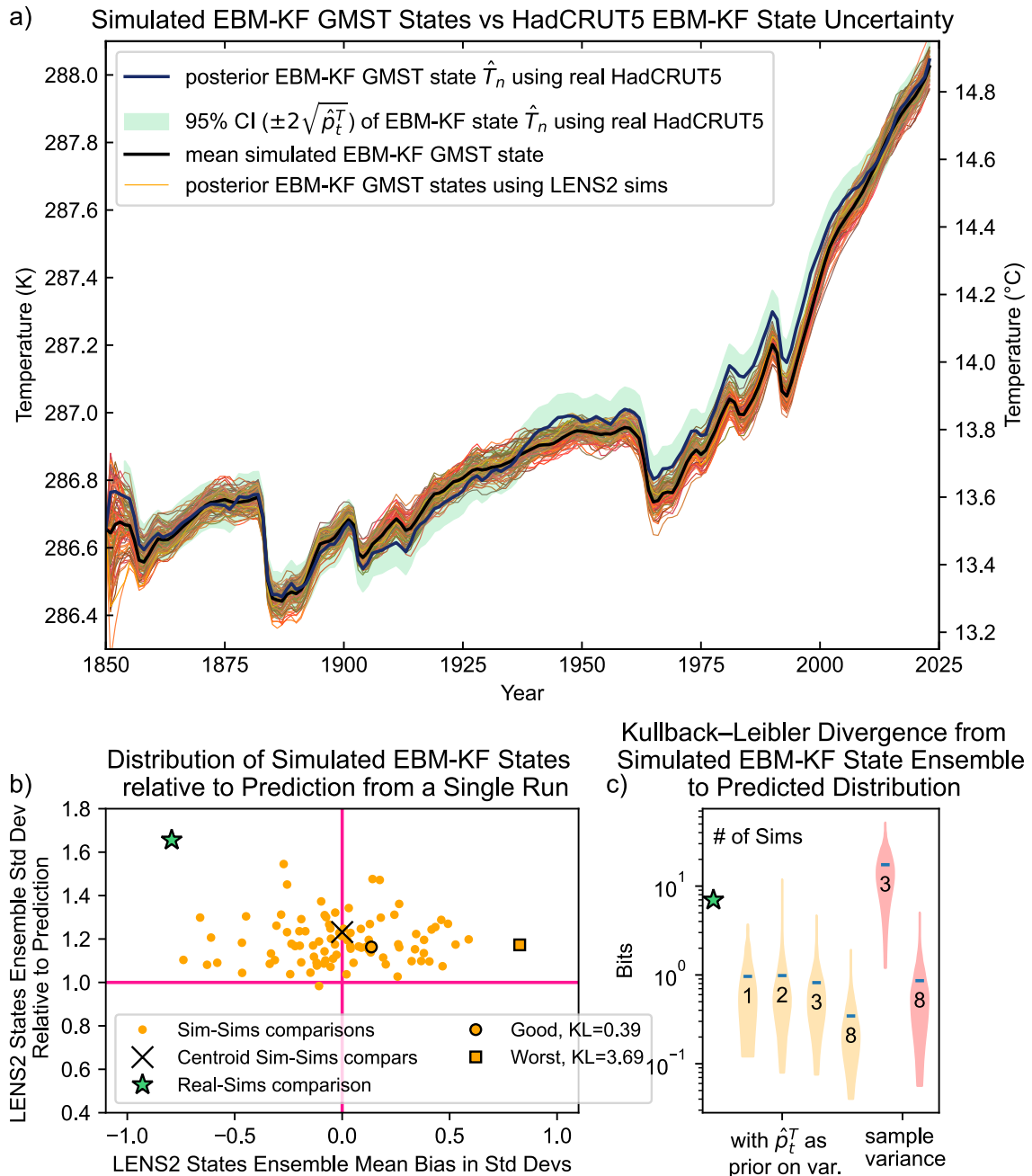
796 We could interpret the time-Filtered ensemble spread versus the climate state
797 uncertainty distribution of one ensemble member in a similar fashion. This has a different
798 purpose, as now we are testing whether the EBM-KF can predict the spread of the time-
799 Filtered LENS2 ensemble correctly, regardless of whether the LENS2 ensemble matches the
800 observed temperatures. If so, that would indicate that from one ensemble member simulation
801 we could effectively predict all the other ensemble members. As expected, there is a

802 distribution of results, where some of the ensemble members are close to the center of the
803 distribution and others are outliers.

804 We can statistically calculate the expected error in our predicted ensemble of time-
805 Filtered LENS2 states from a single member versus the true ensemble of time-Filtered
806 LENS2 states. Panel 7b shows the error in spread (standard deviation) and error in bias by
807 repeatedly making this prediction of a distribution from single members of LENS2 and
808 comparison to the whole time-Filtered LENS2 ensemble. Examining the centroid, this is an
809 unbiased estimate of the distribution (as it should be). However, the ensemble of time-
810 Filtered LENS2 is distributed with a standard deviation that is 1.22 times larger than the
811 average prediction from one ensemble member. At worst, it is 1.54 times larger than any
812 single ensemble member's estimate. Figure 7b labels two examples of where one ensemble
813 member predicts the whole ensemble: a good fit (best quartile) is shown as a circle, and the
814 worst fit is shown as a square. Supp. Fig. 14c,d show these two comparisons in more detail.
815 This error in spread, as well as the distribution of biases are all better than the comparison
816 between the LENS2 time-Filtered states and the observed record's EBM-KF state uncertainty
817 (green star). From this we conclude that the error in predicted distribution from one ensemble
818 member is negligible in comparison to the distance between the model and reality. Thus, this
819 approach is effective in making such comparisons, with a typical bias error in single
820 ensemble member estimate of order $\pm 0.007\text{K}$ with range $(-0.0265--0.0268)\text{K}$.

821 Within panel 7c, the Kullback-Leibler divergence is utilized to evaluate the utility of
822 using the EBM-KF state uncertainty as a prior estimate of the spread between time-Filtered
823 LENS2 ensemble members. At each year, this GMST state variance \hat{p}_t^T is combined in a
824 weighted mean with the sample variance of a small subset of LENS2 members (shown in
825 yellow violin plots, with a number indicating the number of members taken: 1, 2, 3, or 8).
826 Taking 2 LENS2 members does not improve the predicted distribution, as there is a
827 significant chance that two members which are close together will be selected, incorrectly
828 shrinking the predicted ensemble spread. With 3 LENS2 members, the predicted distribution
829 slightly improves. Without using this prior estimate (and allowing the sample variance to
830 change over time, red violin plots), at least 8 LENS2 members are required to generate a
831 predictive ensemble distribution that is comparable to using a single LENS2 member and the
832 Kalman Filter \hat{p}_t^T as the ensemble's variance. Panel 7c demonstrates this with 3 and 8 LENS2
833 members with a time-varying sample mean (red: 3 or 8). Thus, Fig. 7 shows the power of the

834 parametric Gaussian statistics generated by the EBM-KF over a raw ensemble member
 835 sample estimate.
 836
 837



838
 839 Fig. 7: Comparison of the GMST Kalman Filter states across the LENS2 ensemble. a) The
 840 EBM-KF posterior HadCRUT5 state estimate (thick blue) and its 95% confidence interval
 841 (light green), along with EBM-KF state estimates for each individual CESM2 ensemble
 842 member (orange lines) and their mean (thick black line). b) Climate states and associated
 843 uncertainties arising from each of 90 LENS2 simulations and HadCRUT5 are compared to all
 844 other LENS2 climate states, and the relative bias and standard deviation of the resulting
 845 empirical distributions with respect to a particular ensemble member's \hat{p}_t^T . c) Violin plots are
 846 shown comparing the Kullback-Leibler divergence (on a log scale, smaller indicates a better

This manuscript has been submitted for publication to JOURNAL OF CLIMATE (AMS). Please note that this manuscript has undergone two rounds of peer review but has yet to be formally accepted for publication. Subsequent versions of this manuscript may differ slightly in content.

847 match) for a variety of methods of generating a distribution predicting the LENS2-time-
848 Filtered ensemble spread. In yellow, the mean \hat{p}_t^T from 1, 2, 3, or 8 EBM-KF LENS2 runs is
849 averaged, and used in combination with the time-varying sample variance. In red, 3 or 8 of
850 these time-Filtered ensemble members are used to predict an ensemble distribution from
851 time-varying sample variance alone. Taking a single EBM-KF LENS2 run with \hat{p}_t^T
852 approximates the time-Filtered LENS2 ensemble equivalently well to taking the time-varying
853 sample variance of 8 time-Filtered ensemble members.

854
855 LENS2 runs are more similar to each other than to the real Earth, especially regarding
856 outputs such as OHCA (see Supp. Fig. 13) and Arctic or Antarctic sea ice extent (Rosenblum
857 and Eisenman 2017; Roach, Dörr et al. 2020; Horvat 2021). Also, the current generation of
858 ESMs tend to underestimate the appropriate full spread of climate variability. For instance,
859 some weather models use stochastic noise to push their distribution wider than dynamic
860 variation alone (Buizza, Milleer et al. 1999), and other numerical climate models perturb
861 parameters to achieve the same distribution-widening effect (Keil, Schmidt et al. 2021;
862 Duffy, Medeiros et al. 2023).

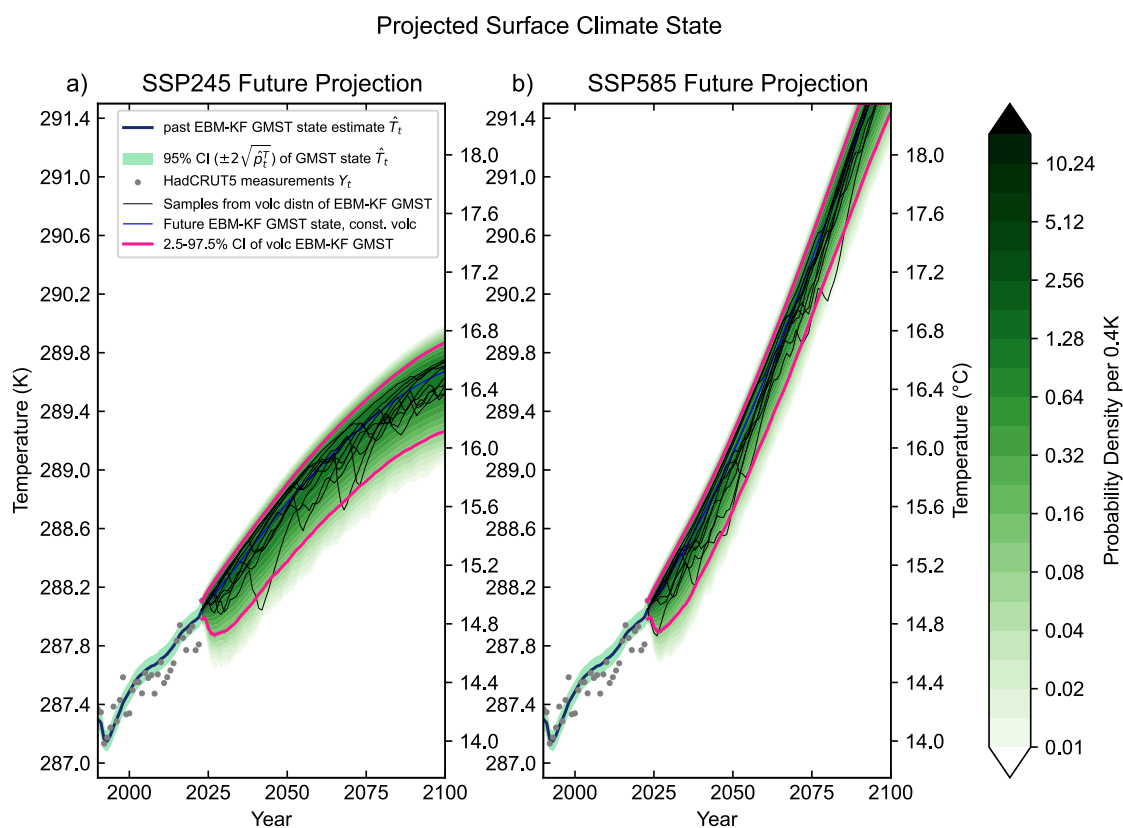
863 Again, Fig. 7 shows that the EBM-KF climate state based on HadCRUT5
864 temperatures or based any one of the LENS2 ensemble members show the expected level of
865 consistency and (potentially biased) Gaussian differences with the rest of the LENS2
866 ensemble. The GMST was estimated from the GSAT of each LENS2 ensemble member.
867 Thus, the EBM-KF on any one of the ensemble members does a good job of estimating the
868 GMST climate state (i.e., averaged over internal variability) and its uncertainty as simulated
869 by the entire LENS2 ensemble.

870 *d. Sampling Future Projections from a Non-Gaussian Volcanic Distribution*

871 In standard climate assessments (e.g., IPCC 2021), future volcanism has long been singled
872 out as an unknown aspect of projected climate change in any given future year, particularly
873 regarding tropical eruptions' contribution to planetary albedo (Marshall et al. 2022). The
874 forcing of historical-period climate models includes the effects of known past volcanoes,
875 while the forcing of future climate models includes only “background forcing from
876 volcanoes”, i.e., an expected average forcing value in future years. Applying an average
877 forcing misses the potential impact of individual volcanic events on the global climate state
878 (compare blue line to black lines in Fig. 8), and because of the nonlinearities and feedbacks in
879 the climate system, these volcanic events can gradually shift the distribution's center.
880 Individual volcanoes can shift weather crossing thresholds by construction (as seen from

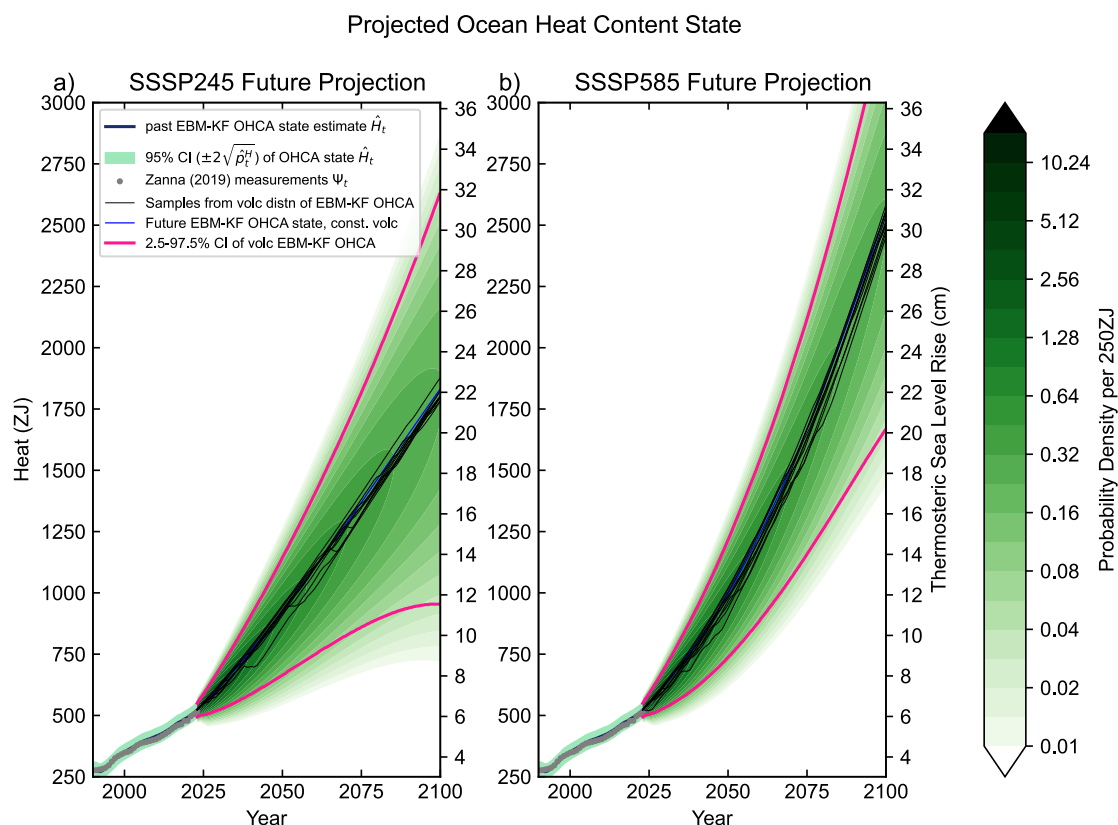
This manuscript has been submitted for publication to JOURNAL OF CLIMATE (AMS). Please note that this manuscript has undergone two rounds of peer review but has yet to be formally accepted for publication. Subsequent versions of this manuscript may differ slightly in content.

881 Pinatubo in Fig. 12f), and so they are important for understanding weather forecasts
 882 especially in the next decade (see Fig. 11a,b). However, running an ESM ensemble of
 883 sufficient size to explore the low probability of a large volcanic eruption in any potential year
 884 is computationally challenging using traditional ESMs, motivating specialized model
 885 intercomparison projects (Zanchettin, Khodri et al. 2016; Timmreck, Mann et al. 2018). By
 886 contrast, robust sampling of rare events is easily accomplished with the inexpensive EBM-
 887 KF. The added contribution of CO₂ and other greenhouse gases from random volcanic
 888 eruptions is not included in this analysis, both because all volcanoes at all latitudes make this
 889 contribution (so the distribution is more uniform), and because this annual contribution is
 890 miniscule compared to anthropogenic greenhouse gasses: 20x smaller in 1900, 130x smaller
 891 in 2010) (Gerlach 2011). Slightly different climate responses have been modeled to occur
 892 when volcanic events were simulated at different phases of climate oscillation patterns, such
 893 as the Pacific Decadal Oscillation (PDO) and North Atlantic Oscillation (NAO) (Illing,
 894 Kadow et al. 2018). Due to its low-dimensional state space, the EBM-KF neglects such
 895 complexities.



896
 897 Fig. 8: Future GMST projections of SSP1-2.6 (a) and SSP3-7.0 (b) scenarios using sampled
 898 measures of volcanic activity and greenhouse gas concentrations calculated according to

899 MAGICC7.0 (Meinshausen, Nicholls et al. 2020). The historical Mt. Pinatubo eruption in
 900 1991 is shown in the lower left corner of both graphs for scale. 10 of the sampled 6000
 901 potential future climate states from the volcanic probability distribution are graphed (thin
 902 black), along with a future climate state projection that uses constant volcanism with average
 903 AOD (blue). The probability density function formed by taking the summation of all sampled
 904 Gaussian kernels at each time point is shaded in green on a logarithmic scale (note these
 905 probability densities are not probabilities so they can exceed 1). Pink lines show the 2.5-
 906 97.5% confidence interval of these probability density functions, which are very
 907 asymmetrical (negatively skewed) due to the sampled volcanic eruptions' impact on GMST.



908
 909 Fig. 9: Future OHCA projections of SSP1-2.6 (a) and SSP3-7.0 (b) scenarios using sampled
 910 measures of volcanic activity and greenhouse gas concentrations calculated according to
 911 MAGICC7.0 (Meinshausen, Nicholls et al. 2020). 10 of the sampled 6000 potential future
 912 climate states from the volcanic probability distribution are graphed (thin black), along with a
 913 future climate state projection that uses constant volcanism with average AOD (blue). The
 914 probability density function formed by taking the summation of all sampled Gaussian kernels
 915 at each time point is shaded in green on a logarithmic scale (note these probability densities
 916 are not probabilities so they can exceed 1). Pink lines show the 2.5-97.5% confidence interval
 917 of these probability density functions, which are only slightly asymmetrical because the
 918 sampled volcanic eruptions have a much smaller impact on OHCA.

919
 920 Figs. 8 & 9 show the future projections of GMST and OHCA using EBM-KF,
 921 including sampling for future volcanoes for two scenarios. SSP1-2.6 shown in Figs. 8a & 9a
 922 has CO₂ emissions that sharply decline after 2020 to keep GMST rise below 2K (van Vuuren,

This manuscript has been submitted for publication to JOURNAL OF CLIMATE (AMS). Please note that this manuscript has undergone two rounds of peer review but has yet to be formally accepted for publication. Subsequent versions of this manuscript may differ slightly in content.

923 den Elzen et al. 2007; van Vuuren, Stehfest et al. 2017). SSP3-7.0 shown in Figs. 8b & 9b is
 924 a higher emission scenario in which CO₂ emissions double by 2100 (Fujimori, Hasegawa et
 925 al. 2017). Note that the volcanic ensemble probability density is not symmetrical for GMST -
 926 there is a much longer tail on the cooler side because of intermittent cooling by volcanic
 927 aerosols. In Fig. 8 the cooler side of the distribution takes a few years to fully expand out
 928 because large eruptions generally did not produce their maximal effect on AOD (and thus the
 929 GMST climate state) until 1-2 years after the eruption began, and there are no major
 930 eruptions ongoing at present. Indeed, the volcanic eruptions dominate the future uncertainty
 931 over the slowly growing GMST climate state uncertainty and rival or exceed the scenario
 932 uncertainty up until about 2050 (assuming known model parameters, Fig. 11a). By contrast,
 933 the LENS2 using “constant background” future volcanism has a symmetrical distribution for
 934 future projections of the same SSPs (Supp Fig. 6, right of dashed line). The effects of
 935 volcanism on OHCA (Fig. 9) are much smaller than on GMST (Fig. 8), but there is still a
 936 longer tail toward the low OHCA side. Regarding future GMST policy threshold crossings,
 937 the uncertainty regarding volcanic eruptions lessens the difference between the climate state
 938 threshold crossing interval and the temperature prediction threshold crossing interval.

939 Across many future simulations the dynamic model Jacobian matrix Φ_t happens to
 940 remain nearly constant at values of: $\Phi_t \approx \begin{bmatrix} 0.893 & 0.000253 \text{ K} / \frac{\text{W yr}}{\text{m}^2} \\ 11.1 \frac{\text{W yr}}{\text{m}^2} / \text{K} & 0.999 \end{bmatrix}$, nearly unit
 941 triangular. Due to this Jacobian matrix shape and the 0.893 factor, \hat{p}_t^T grows sub-linearly,
 942 with yearly growth less than the GMST-exclusive component of $Q = \sqrt{0.01107 \text{ K}^2} = 0.00037$
 943 K^2 . (see Eq. 22) Over a 78-year future projection (2023-2100) the GMST state 95%
 944 confidence interval $2\sqrt{\hat{p}_t^T}$ only grows from 0.0625K to between 0.1757K and 0.1792K. This
 945 2.8-fold increase is small over the 21st century compared to the GMST dips that occur under
 946 volcanic eruptions (see Figs. 8 & 10). The effect of volcanoes on historical state (Figs. 3 & 4)
 947 and future projections (Fig. 8) is therefore worthy of specialized treatment in addition to
 948 measurement uncertainty and internal chaotic variability (see Section 3d). In contrast, the
 949 OHCA component of the state uncertainty 95% confidence interval $2\sqrt{\hat{p}_t^H}$ grows
 950 exponentially due to the 11.1 value in the lower-left entry of Φ_t , and volcanoes have a
 951 negligible effect on of projected OHCA trajectories (see Fig. 9). The ocean state uncertainty
 952 95% CI = $2\sqrt{\hat{p}_t^H}$, initially at $2.57 \frac{\text{W yr}}{\text{m}^2}$ (29.4 ZJ) in 2023, balloons to $76.1-77.1 \frac{\text{W yr}}{\text{m}^2}$ (870-880
 953 ZJ) by 2100.

954

955 **4. Discussion**

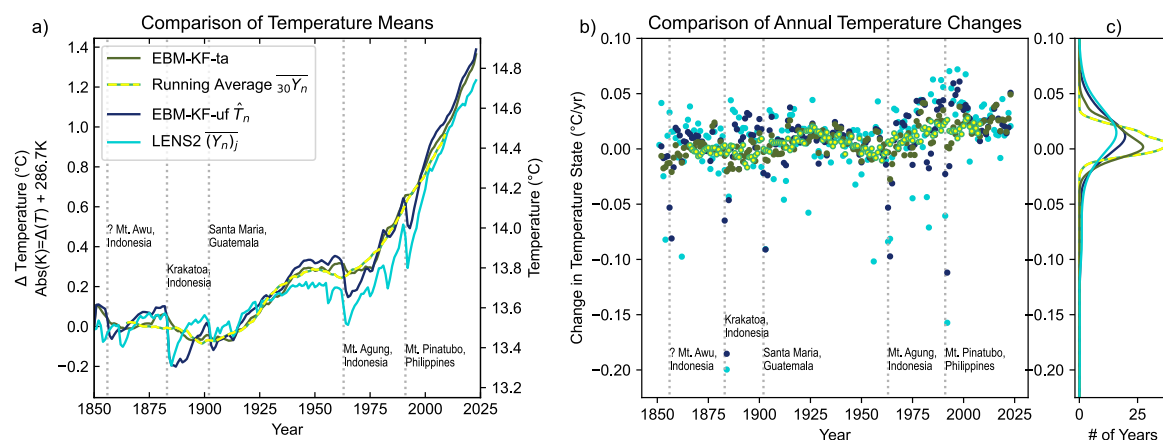
956 The EBM-KF climate state estimate resembles other standard estimates of climate state, but it
957 has advantages they do not share. The EBM-KF algorithm, because of its relationship to a
958 forward or “blind” EBM, can be projected forward in time without temperature observations
959 and thus can be used in many situations. Unlike an ESM, the EBM-KF benefits from data
960 assimilation due to its Kalman filter nature and thus remains close to observations or
961 synthetic data (e.g., the examples in Section 4 of reproducing the LENS2 from few ensemble
962 members or the ensemble of potential volcanic activity futures). The OHCA component is
963 particularly sensitive to assimilated observations (see Fig. 3b), largely because of reduced
964 understanding of the ocean dynamics that drive deep ocean heat uptake compared to
965 atmospheric radiative feedbacks. The EBM has a correspondingly simpler model of this
966 process. Unlike an Ensemble Kalman filter approach that can reweight a full-physics ESM
967 ensemble toward observations, the EBM-KF has negligible computational cost and can thus
968 examine rare, long-tailed events such as volcanoes. Additionally, tuning of the EBM
969 parameters and uncertainty quantification of these results can benefit from the literature and
970 algorithms to optimize our Kalman Filter parameters.

971 *a. Comparison to Previous Estimation Methods of the Climate State*

972 Although they are different types of average, a direct comparison (Fig. 10) of the state
973 estimated from the EBM-KF (Fig. 4) and that estimated by the 30-year running mean (Fig. 1)
974 and the LENS2 ensemble mean (Supp. Fig. 6), the EBM-KF has slightly more year-to-year
975 variation than the 30-year mean and less than the LENS2 ensemble mean. Departures from
976 the main Gaussian cloud in all methods represent volcanoes. The 5 largest eruptions which
977 caused the largest dip in EBM-KF state are labeled in Fig. 10, corresponding to the 5 peaks in
978 $\text{AOD} \geq 0.06$ plotted in Fig. B1a in the appendix. The climate effects of these major tropical
979 volcanic eruptions have been studied extensively (*McCormick, Thomason et al. 1995; Jones
980 and Kelly 1996*). Note for the eruptions listed, plus many others, the dips in the EBM-KF
981 mean state correspond with dips in the sample mean of the LENS2 simulations. However, the
982 earliest AOD values provided by Sato (1993) also demonstrate a major spike at 1856, which
983 is not reflected in the LENS2 simulations. This may correspond to either the 1856 eruptions
984 of Komaga-take, Japan or Mt. Awu, Indonesia, and we labeled this with the latter eruption

985 because tropical volcanic eruptions typically have a much larger climate impact (Marshall et
 986 al. 2022).

987



988

989 Fig. 10 a) Direct GMST “climate state” comparison of the 30-year averaged GMST (yellow-
 990 green dashed), the EBM-KF-ta state (dark green), the EBM-KF-uf state (navy blue), and the
 991 ensemble mean of GSAT in the LENS2 simulations (sky blue). b) For “climate states” with
 992 the same colors as in panel a, the distribution of innovations (derivative) is plotted against
 993 time. c) A smoothed empirical density with respect to yearly change in temperature is linked
 994 to panel b. (This empirical density is simply an approximation of a histogram, and the kernel
 995 densities are not provided by elements of the Kalman Filter as in Fig 4b and 5b). Major
 996 volcanic eruptions are labeled in both panels a and b with dotted vertical light gray lines. In
 997 all panels, the 30-year averaged GMST (yellow-green dashed) is close to the EBM-KF-ta
 998 state (dark green), whereas the EBM-KF-uf state (navy blue) resembles the LENS2
 999 simulations (sky blue) in responses to volcanic eruptions.

1000

1001 Based on this interpretation of Fig. 10, we now see that the LENS2 ensemble average
 1002 (light blue) is closer to the (EBM-KF-uf, navy blue, with uf abbreviating “un-filtered” AOD
 1003 forcing) regarding sensitivity to volcanoes than the 30-year running mean (yellow-green). In
 1004 response to this, we will distinguish three preparations of AOD forcing: one that takes a
 1005 centered 30-year running average of AOD (EBM-KF-ca, not shown, with ca abbreviating
 1006 “centered average”), one that directly uses the annual measured values of AOD (EBM-KF-uf,
 1007 navy blue, as above), and one that takes a 15-year trailing average combined in equal weight
 1008 with the overall timeseries AOD mean (EBM-KF-ta in dark green, the best point estimate for
 1009 the 15-years of future AOD and displayed as a green line in Fig. B1a, with ta abbreviating
 1010 “trailing average”). As demonstrated in Fig. 10, this EBM-KF-ta preparation of the AOD
 1011 (dark green) brings the EBM-KF-tf close to the 30-year running mean (yellow-green)
 1012 regarding sensitivity to volcanoes (their maximum separation was in 1962 with the 30-year

This manuscript has been submitted for publication to JOURNAL OF CLIMATE (AMS). Please note that this manuscript has undergone two rounds of peer review but has yet to be formally accepted for publication. Subsequent versions of this manuscript may differ slightly in content.

1013 running average -0.073°C cooler, otherwise their average absolute separation $\pm 0.025^{\circ}\text{C}$,
1014 standard deviation $\pm 0.030^{\circ}\text{C}$, $r^2=0.986$). We prefer EBM-KF-ta (dark green) to EBM-KF-ca
1015 (not shown) as the latter involves future information, and the EBM-KF-ca does not get closer
1016 to the 30-year running mean (maximum separation was in 1976 with the 30-year running
1017 average -0.080°C cooler than the EBM-KF-ca, otherwise their average absolute separation
1018 was $\pm 0.025^{\circ}\text{C}$, standard deviation $\pm 0.031^{\circ}\text{C}$, $r^2=0.987$). If we are trying to directly match the
1019 behavior of ensembles such as LENS2 (light blue), the EBM-KF-uf (navy blue) is the correct
1020 choice. As noted in Section 3a, LENS2 is farther from EBM-KF-uf because LENS2 has a
1021 cold bias over 1940-2000 (max separation in 1983 of 0.262°C , average absolute separation
1022 $\pm 0.088^{\circ}\text{C}$, standard deviation $\pm 0.085^{\circ}\text{C}$, $r^2=0.928$), but the responses to volcanic events are
1023 very similar (highlighted in Fig. 10b). If we are trying to estimate both the weather and
1024 climate state without bias, for next-year predictions and beyond (so AOD will be
1025 unavailable), then the optimal method is to run many predictions using EBM-KF-uf and a
1026 volcanic probability distribution, as in section 4d. Filtering of other forcing, e.g., $[\text{eCO}_2]$,
1027 yielded negligible changes as these fields are more slowly evolving than volcanic AOD.

1028 It is beyond the scope of this paper to detail the characteristics of the large and
1029 growing variety of “mean state” definitions, but a summary is useful. For all methods we
1030 have examined regarding the GMST (30-year mean – Fig. 1, EBM-KF – Fig. 4, LENS2
1031 model ensemble mean – Supp. Fig. 6, purely statistical methods – Supp. Fig. 4c, 4d, 5), the
1032 differences in the estimated climate state are relatively small in available years (on the order
1033 of 0.1K – see Supp. Fig. 7, column 1). The largest differences seen between these methods lie
1034 in the spread of the changes from year to year (see Supp. Fig. 7, column 2) which can be
1035 addressed by preparations filtering the forcing and persistent mean anomalies relative to
1036 observations, particularly so in the forward, blind LENS2 ensemble (see Supp. Fig. 7, column
1037 4).

1038 The primary distinction of our EBM-KF method and all existing alternative
1039 definitions is the integrated quantification of uncertainty. While many methods exhibit a
1040 relationship between the “mean state” and “sample” that varies in time, the EBM-KF (and the
1041 related RTS) quickly converge to a stable state uncertainty of 0.034K (and 0.023K for the
1042 RTS, see Supp. Fig. 2). Our choice of method was motivated by the mathematical
1043 compatibility between the governing equation for a Kalman filter and that of an EBM, which
1044 is not true of many alternatives, e.g., a Butterworth filter or Bayesian changepoint analysis

This manuscript has been submitted for publication to JOURNAL OF CLIMATE (AMS). Please note that this manuscript has undergone two rounds of peer review but has yet to be formally accepted for publication. Subsequent versions of this manuscript may differ slightly in content.

1045 and an EBM. We also emphasize again that our EBM-KF infers the climate state directly via
1046 yearly signal processing, which is a different approach than extrapolating the future weather
1047 to the next 15 years using reforecasts with a weather emulator and calculating many 30-year
1048 means. In the next section we compare the EBM-KF uncertainties to those of ESM
1049 ensembles.

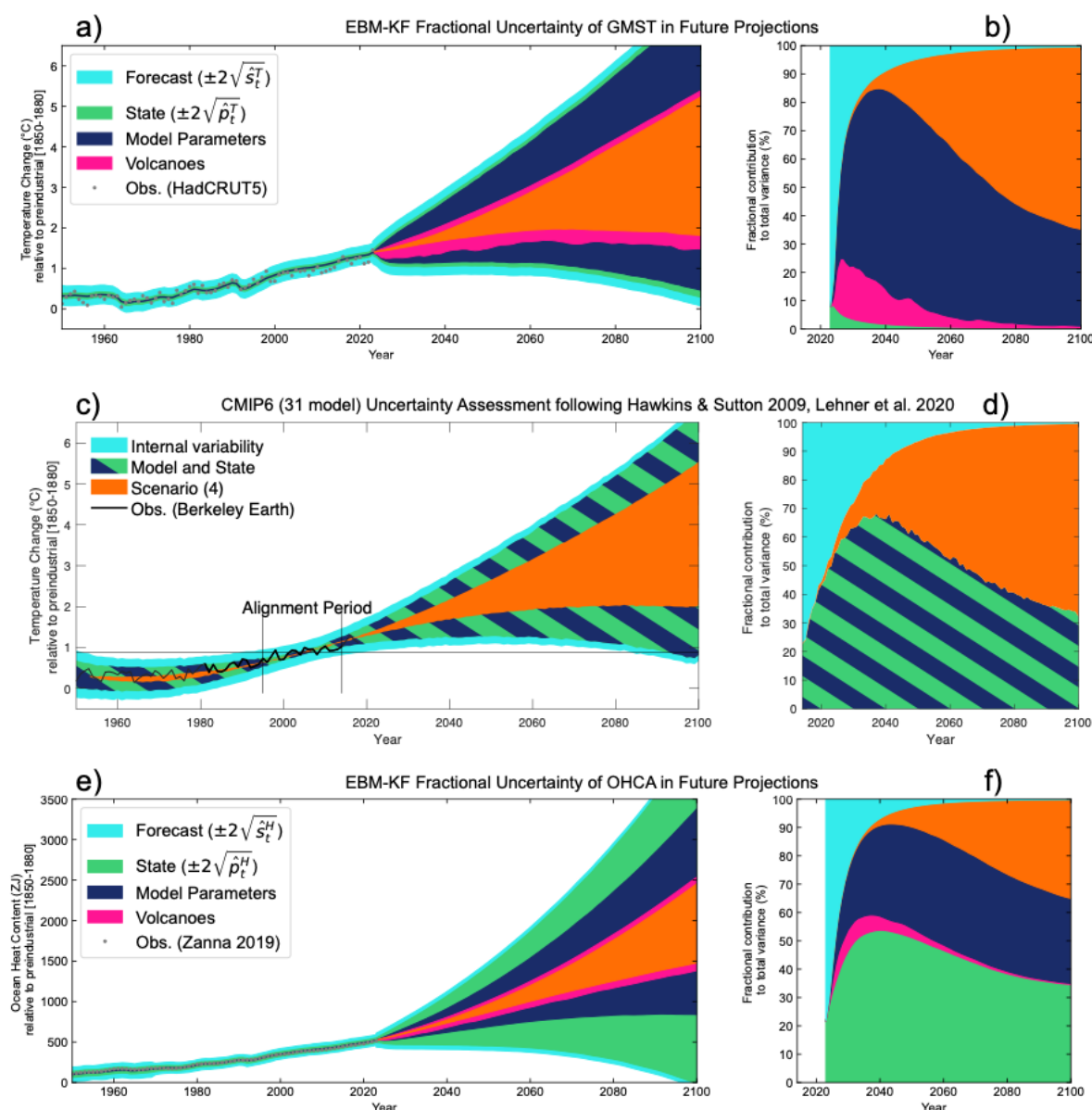
1050 *b. Comparison to Earth System Models (CESM2 Large Ensemble and CMIP5)*

1051 The chief advantages of EBM-KF over an ensemble of ESMs is that it replicates
1052 many statistical features while being trivial to compute. Fig. 7 suggested that any of the
1053 ensemble members or the observed temperature record could be used together with EBM-KF
1054 to recreate the climate state, but now we examine if we can anticipate or improve on the
1055 ensemble statistics *without a single ensemble member*.

1056 First, we examine the basic statistical character of LENS2. The distribution of annual
1057 differences of all ESM trajectories from the ensemble mean are remarkably close to Gaussian
1058 (see Supp. Fig. 10a). Therefore, again due to the central limit theorem, this fundamental
1059 assumption of the EBM-KF is also met by GSAT simulated by the CESM2. The standard
1060 deviation rises insignificantly with time in LENS2 over the entire simulation duration
1061 ($p=0.168$). Before 2065 this rise is significant ($p=1.2 \cdot 10^{-6}$, see Supp. Fig. 10b) while
1062 relatively small (linear trend $r^2=0.105$ and only 8.9% rise in σ from 1850-2065). The time-
1063 averaged standard deviation 0.127K was close to both chosen total GMST-exclusive (top-
1064 left) measurement noise from R_t (range 0.107 – 0.136K, see section 2c, Eq. 21) and half the
1065 converged values in the EBM-KF of $\sqrt{\hat{\sigma}_t^T}$: 0.13K in 1865, later 0.112K in 2000. Examining
1066 skewness and kurtosis, the distribution of simulations about the LENS2 GSAT ensemble
1067 mean is not meaningfully altered as the climate warms (see Supp. Fig. 10c,d).

1068 Next, we evaluated how well the LENS2 captures the overall shape of the observed
1069 HadCRUT5 temperatures, given that it is not constrained directly by these observations. The
1070 absolute temperature of the LENS2 runs had to be revised down by a full 1.75K to match its
1071 ensemble 1850-1950 100-year average GMST to HadCRUT5. Other authors have also noted
1072 this high absolute temperature as well as the high climate sensitivity of CESM2, the model
1073 used in LENS2 (Gettelman, Hannay et al. 2019; Feng, Otto-Bliesner et al. 2020; Zhu, Otto-
1074 Bliesner et al. 2022). Recall HadCRUT5 was recalibrated to a 1960-1990 30-year climate
1075 normal (Jones and Harpham 2013) of 13.85°C (287.00K), and the LENS2 average has a
1076 slightly lower temperature during this 30-year climate normal of 13.71°C (286.86K).

1077



1078

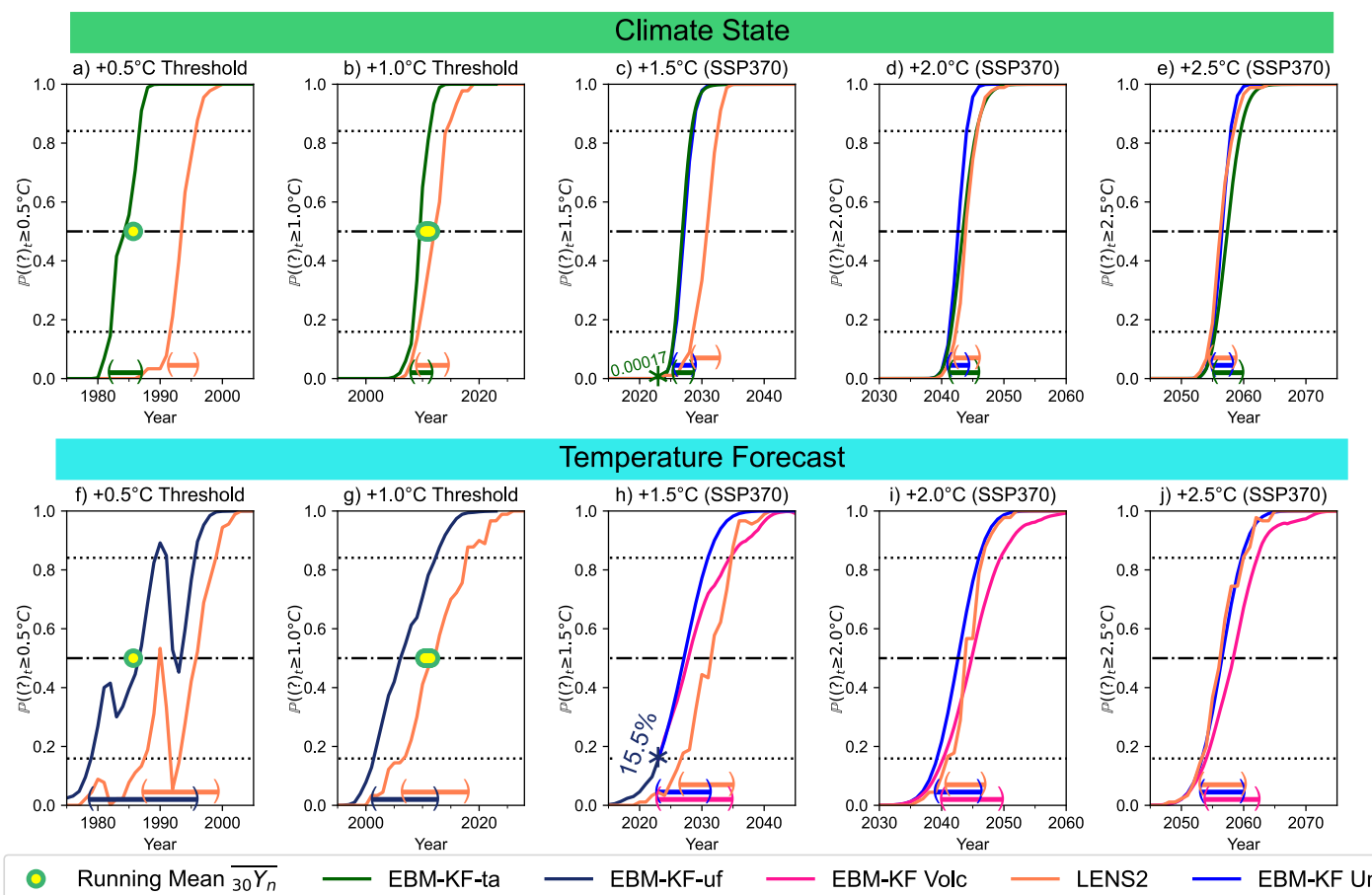
1079 Fig. 11: “Hawkins Plots” (Hawkins and Sutton 2009) of the sources of uncertainty (95% CI
 1080 on left, fractional variance on the right) in future projections, with the top row (a, b) showing
 1081 the GMST state projections from the EBM-KF, the middle row (c,d) showing global mean
 1082 surface air temperature GSAT from CMIP6, and the bottom figure (e,f) showing the OHCA
 1083 projections from the EBM-KF. Refer to (Lehner, Deser et al. 2020) for details on how panels
 1084 c and d were generated (relying on 4th-degree polynomials for smoothing), but here showing
 1085 95% CI and annual (rather than decadal) variability. Note that noise from internal dynamical
 1086 variability is marked in light blue in all figures, and while initially dominant ($\geq 80\%$), it
 1087 quickly falls off within the first decade, to eventually be replaced with emissions scenario
 1088 uncertainty in orange. The extent to which different smoothed ESMs disagree within CMIP6
 1089 for the same emissions scenario (“model uncertainty”) is plotted in green, as it is roughly
 1090 analogous to the climate state covariance within the EBM-KF, Future uncertainty related to
 1091 volcanoes (in magenta) is negatively skewed and very important in the first 3-25 years of the
 1092 EBM-KF’s projections of GMST.
 1093

1094 We also compared EBM-KF projections (Fig. 8) with LENS2 projections (Supp. Fig.
1095 6). Both Fig. 8b and the right side of Supp. Fig. 6 trace out roughly the same shapes, as both
1096 are forced by the SSP3-7.0 projections. The largely symmetric variation in the LENS2 is
1097 driven by dynamical instability. This is fundamentally different from the EBM-KF, which in
1098 addition to scaled, weather-driven uncertainty samples a noisy distribution of volcanic
1099 eruptions, yielding an asymmetrical distribution. LENS2 projections based on SSP3-7.0
1100 achieve a slightly higher mean temperature in 2100 (291.3K, +4.6K warming) than the
1101 equivalent EBM-KF projection (290.9K, +4.2K warming, see Fig. 8b), despite the LENS2
1102 simulations being cooler throughout most of the 20th century and early 21st century (see Fig.
1103 10a). Across all CMIP6 models (Lee, Marotzke et al. 2021; Tebaldi, Debeire et al. 2021) the
1104 projected warming under this scenario is 3.9K with 5-95% range (+2.8K, +5.5K), closer to
1105 the EBM-KF projection.

1106 Continuing beyond LENS2 to compare against the multi-model CMIP6 ensemble, a
1107 projected uncertainty decomposition is created following Hawkins and Sutton (2009) and
1108 Lehner, Deser et al. (2020) in Fig. 11. By the methods in Section 4c, the EBM-KF adds the
1109 volcanic uncertainty into this picture (pink). A second advantage is that the climate state
1110 uncertainty (due to the cumulative reliability of measurements with respect to a model) and
1111 the model uncertainty (due to the confidence in the model structure and parameters) can be
1112 distinguished. For simplicity, we estimated the model and parameter uncertainty of the EBM-
1113 KF by just varying the cloud feedback parameter (samples from $\mathcal{N}(0.42, 0.36^2)$, based on
1114 Figure 7.10 and Table 7.10 of AR6 (Forster, Storelvmo et al. 2021)) and the ocean heat
1115 conductivity (samples from $\mathcal{N}(0.42, 0.36^2)$, based on Geoffroy et al. Part II (2013)).
1116 Incomplete understanding of cloud feedback is a primary source of uncertainty within ESMs,
1117 leading to diverging predictions within CMIP6 (Zelinka, Randall et al. 2017; Ceppi and
1118 Nowack 2021), and as noted above the OHCA dynamics of EBM-KF are oversimplified
1119 (Cheng, von Schuckmann et al. 2022; Newsom, Zanna et al. 2023) and sparse long-term
1120 records yield disparate OHCA reconstructions before 2005 (see Figure 2.26 of AR6). (Gulev,
1121 Thorne et al. 2021).

1122 Regarding the various types of climate policy thresholds, the LENS2 can be used to
1123 generate very similar results to the EBM-KF (Figs. 6 & 12). Differences in absolute
1124 probability and policy threshold crossing instants reflect differences in the modeled climate
1125 states: particularly that the LENS2 ensemble was slightly cooler than the EBM-KF model
1126 after correcting to the same preindustrial temperature, so policy thresholds were crossed 3-5
1127 years later (Fig. 12). The eruption of Mt. Pinatubo caused the policy threshold of +0.5K to be

1128 crossed in three instants within the EBM-KF model, because this eruption temporarily cooled
 1129 the climate state back below the threshold temperature. The first of these EBM-KF crossings
 1130 coincides very closely with the (single) policy threshold crossing instant of the 30-year
 1131 running mean (indicated by orange asterisks). The 21-year running averages of the LENS2
 1132 simulations only crossed the 0.5K threshold once, illustrating how the EBM-KF state
 1133 estimate fundamentally differs from a running mean. Future threshold crossings (1.5K, 2.0K,
 1134 2.5K) under the SSP3-7.0 projection scenario show close temporal alignment in the threshold
 1135 instants between LENS2 and the EBM-KF estimates that sample for volcanic uncertainty.
 1136 Although shifted, the overall shapes of these cumulative distribution functions and spans of
 1137 the threshold crossing windows are more similar between LENS2 and a single EBM-KF
 1138 future estimate that like LENS2 keeps AOD constant (see Fig. 12). In contrast, there is a long
 1139 tail on the >90% portion of the future sample volcanism (pink lines, lower row) regarding
 1140 temperature forecast thresholds, extending the later bound of the crossing period by about 5
 1141 years, because there remains a modest chance that a large volcano will erupt and tip the
 1142 temperature forecast below that threshold.



1143 Fig. 12: Comparison of 0.5-2.5K GMST policy threshold crossing probabilities for various
 1144 relevant preparations of the EBM-KF and CESM2 LENS simulations (orange). The top row
 1145

This manuscript has been submitted for publication to JOURNAL OF CLIMATE (AMS). Please note that this manuscript has undergone two rounds of peer review but has yet to be formally accepted for publication. Subsequent versions of this manuscript may differ slightly in content.

1146 of panels a-e compare climate states in the EBM-KF with 21-year averages of the LENS2
1147 simulations. The bottom row f-j compares next-year temperature forecasts from the EBM-KF
1148 directly with the LENS2 simulations. Recall from Section 3b that these are the integrals of all
1149 probability densities of the GMST climate states or temperature forecasts below that policy
1150 threshold. Historical EBM-KF-uf estimates of temperature forecasts are in dark blue in panels
1151 f,g, with the latter reproduced from Fig. 6c. Regarding climate state thresholds, the EBM-KF-
1152 ta states are shown in green in panels a,b. These EBM-KF-ta state estimates come the closest
1153 to matching the instants (yellow-green dots) when the 30-year running average crossed the
1154 0.5°C threshold in 1985 (or very likely from a linear trend will have crossed the 1.0°C
1155 threshold in 2010 or 2011). Two versions of future EBM-KF state estimates are shown: an
1156 amalgamation of samples in pink (in h,i,j) from the volcanic distribution shown in Fig. 8, and
1157 a single run in bright blue (in c,d,e,h,i,j) with uniform AOD mirroring how LENS2 treats
1158 volcanism. In future climate state projections (green in c,d,e), samples of future volcanism
1159 are first pre-processed according to EMB-KF-ta. Policy threshold crossing instants
1160 (intersecting horizontal and vertical lines) and crossing windows (arrows at bottom) are also
1161 shown.

1162 *c. Potential Issues with the EBM-KF and Future Extensions*

1163 This first climate Kalman filter does not generate regional temperatures nor other
1164 essential climate variables, such as precipitation. These variables are often highly non-
1165 Gaussian and may require an understanding of regional “dynamical tipping points” or other
1166 important nonlinear process aspects of climate change. Additionally, this 2-component EBM-
1167 KF lacks a “memory ENSO state” to allow for prediction of 2-7 year quasi-periodic El Nino
1168 events (Hu and Fedorov 2017), and without such a state our EBM-KF wrongly assumes that
1169 weather innovations z_t^T have no autocorrelation. Therefore, this first EBM-KF is far from
1170 generating the information required to replace many aspects of large ensembles. An expanded
1171 global climate state vector, including precipitation, seasonal temperature, or eigenvalues of
1172 spatially decomposed principal components (e.g., El Nino / Southern Oscillation) might be
1173 appended into this statistical framework with appropriate physical forward modeling (Yang,
1174 Li et al. 2018).

1175 Astute readers may note the estimated climate state and covariance within the EBM-
1176 KF are influenced by the choice of reconstructed HadCRUT5 GMST and Zanna et al. (2019)
1177 OHCA. With only minor modifications, the EBM-KF method could be used with multiple
1178 annual reconstructions at the same time, e.g., GISTEMP GMST (Lenssen, Schmidt et al.
1179 2019) or other OHCA reconstructions (Cheng, Trenberth et al. 2017; Ishii, Fukuda et al.
1180 2017), considering each as only an estimate of the true GMST or OHCA (Willner, Chang et
1181 al. 1977). Reconstructions of sea level rise could be used from different sources as further
1182 constraints on OHCA (Palmer, Howard et al. 2018; Fox-Kemper, Hewitt et al. 2021; Palmer,
1183 Domingues et al. 2021).

This manuscript has been submitted for publication to JOURNAL OF CLIMATE (AMS). Please note that this manuscript has undergone two rounds of peer review but has yet to be formally accepted for publication. Subsequent versions of this manuscript may differ slightly in content.

1184 Here we use pre-selected, constant parameters at their published values in the EBM-
1185 KF. However, methods for tuning parameters, including time-dependent parameters, within
1186 Kalman filters are much more extensively studied mathematically (Chen, Heckman et al.
1187 2018; Zhang and Atia 2020; Chen, Heckman et al. 2021) than the methods thus far applied in
1188 climate sciences to diagnose parameter variations within energy balance models (e.g., the
1189 regional effects diagnosed in Armour, Bitz et al. (2013) and the global effects found by
1190 Gregory and Andrews (2016)). Our EBM-KF hybrid presents an opportunity to adopt KF
1191 parameter optimization methods for the GMST, OHCA projection optimization problem. In a
1192 preliminary experiment with Bayesian parameter search to give better estimates of the
1193 coefficients in the blind EBM, the prior distributions of these coefficients (rather than point
1194 estimates) were extracted from climate science literature, followed by a Metropolis-Hastings
1195 search. Several parameters required further care or tuning to achieve desired constraints (e.g.,
1196 balanced energy transfer in the preindustrial climate), such as the main longwave radiation
1197 coefficient and the temperature exponent. However, identifiability and overfitting are
1198 challenges of this approach and deserve more attention than the scope of this paper allows.
1199 In this first illustration of the system, opportune imperfections in the point estimates given by
1200 literature sources allow demonstration of the course-corrective properties of the EBM-KF
1201 (Fig. 4).

1202 *d. Policy Utility*

1203 Has the climate already passed the 1.5°C policy threshold? Real-time, accurate
1204 knowledge of policy threshold crossing will allow for more prudent planning and more
1205 comprehensible communication of climate science to the public. For instance, while the
1206 “Climate Clock” (<https://climateclock.world>) intends to communicate the urgency of the
1207 climate crisis with a countdown to the estimated expenditure of our remaining carbon budget,
1208 only a static date informs it. In contrast, an EBM-KF threshold reflects the most recently
1209 measured state of the Earth system and up-to-date emissions and present limits on future
1210 emissions. As can be seen in Fig. 12h, there was a substantial (15.5%) chance that 2023’s
1211 GMST measurement could have exceeded the 1.5°C threshold. Indeed, the HadCRUT5 2023
1212 number came close at 1.45°C, and others with slightly different methodologies reported
1213 1.52°C above preindustrial (Burgess 2024). Rather than relying on sponge proxy data to posit
1214 that the climate state has exceeded this threshold (McCulloch, Winter et al. 2024), or using an
1215 overlap window between ESM projections and smoothed observations that is challenging to
1216 translate into probability (Hausfather 2024), the EBM-KF-ta can simply give a p-value

This manuscript has been submitted for publication to JOURNAL OF CLIMATE (AMS). Please note that this manuscript has undergone two rounds of peer review but has yet to be formally accepted for publication. Subsequent versions of this manuscript may differ slightly in content.

1217 (subject to the key, but quantifiable uncertainties of the EBM-KF mapped in Fig. 11). By this
1218 method, assuming our original point-estimates of key feedback parameters, we have not yet
1219 crossed the 1.5°C climate policy threshold: the EBM-KF-ta states (Fig. 12c) that there is
1220 $p=0.00017$ that the climate state exceeded 1.5°C in 2021.

1221 Climate modeling with ESMs is slow, computationally expensive, and typically
1222 performed with blind models that do not respond to the latest observations. The relatively
1223 simple question, “How did the COVID-19 lockdowns and the 8% reduction in CO₂ emissions
1224 impact the near-term climate?” required hundreds of ESM simulations to yield a statistically
1225 insignificant answer (Jones, Hickman et al. 2021). That sort of modeling effort, arriving
1226 months or years after the question was posed, is an unsatisfactory prize for many aspects of
1227 communication and decision making for the annual profit or election term. The EBM-KF can
1228 produce the result that an 8% emissions reduction over 2 years cools the climate state by
1229 $\sim 0.0017\text{K}$ and pushes back subsequent threshold crossing time by 1.2 months – an
1230 insufficient reduction in climate change, but at least precisely and rapidly quantified. The
1231 EBM-KF is sufficiently fast that, once fully calibrated, it could be easily embedded as an
1232 interactive web tool for such exploration. This demonstrates that, like “attributable
1233 anthropogenic warming” the EBM-KF is an “anti-fragile index” and therefore of greater use
1234 to planning climate mitigation strategies (Otto, Frame et al. 2015).

1235 Additionally, Kalman filters are often used for process control (Myers and Luecke
1236 1991; Lee and Ricker 1994), and in this case an EBM-KF could be used to optimize climate
1237 change mitigation or intervention strategies (Filar, Gaertner et al. 1996; MacMartin, Kravitz
1238 et al. 2014; Kravitz, MacMartin et al. 2016). For instance, within carbon offset / sequestration
1239 and geoengineering accreditation markets, credits could be assigned based on the projected
1240 delay in crossing policy thresholds. Once a space of potential climate solutions has been
1241 defined, the EBM-KF can work seamlessly with a variety of optimizers to find the maximum
1242 climate benefit at the lowest societal cost.

1243 **5. Conclusion**

1244 The EBM-KF presented in this paper takes the best features from a 30-year running
1245 mean of GMST (the historical definition of climate) and state-of-the-art ESM large
1246 ensembles such as CESM2 LENS. The EBM-KF GMST climate state, which also tracks the
1247 ocean heat content anomaly (OHCA), is constructed to be very close to that of a running 30-
1248 year mean but generates this climate state 15 years sooner: it has no lag in reporting after
1249 annual observations are collected. This filtered climate state captures the overall shape of the

This manuscript has been submitted for publication to JOURNAL OF CLIMATE (AMS). Please note that this manuscript has undergone two rounds of peer review but has yet to be formally accepted for publication. Subsequent versions of this manuscript may differ slightly in content.

1250 30-year means of measured GMST ($r^2 = 0.922$) and OHCA ($r^2 = 0.989$). In comparison to the
1251 ensemble spread of a hindcast ensemble of an ESM (LENS2), which is the state-of-the-art
1252 method for quantifying internal variability and probabilistic futures, the EBM-KF provides a
1253 similar Gaussian distribution. Using this distribution, EBM-KF can annually assess the
1254 likelihood of whether a policy threshold, e.g., 1.5 or 2°C over preindustrial, has been crossed.
1255 The EBM-KF is also accurate at inferring the behavior of an entire climate model large
1256 ensemble using only one or a few ensemble members. In future projections of climate under
1257 SSP trajectories, the efficiency of the EBM-KF allows for sampling non-Gaussian
1258 probabilistic futures, e.g., the impact of rare but significant events such as future volcanic
1259 eruptions. An exponential mixture model of future volcanic eruptions causes the EBM-KF
1260 GMST climate states to be negatively skewed, unlike LENS2 which remains Gaussian by
1261 constant forcing design.

1262 The EBM-KF approach has transparent, clean physical parameters of the EBM that
1263 can be directly measured or taken from estimates in modeling literature, leading to trivial
1264 uncertainty quantification by the Kalman filter machinery under fixed parameters. This
1265 uncertainty quantification revealed important aspects of GMST and OHCA uncertainty, both
1266 in hindcast and future projections contexts, with and without volcanoes. We considered that
1267 the EBM-KF may be improved with time-varying EBM parameters or other extensions,
1268 although a thorough treatment is left for future work. While the EBM-KF does not predict all
1269 climate variables of interest, it is a powerful, transparent, and inexpensive tool that may be
1270 readily combined with other approaches.

1271 *Acknowledgments.*

1272 BFK was funded by ONR N00014-17-1-2393 and NOAA NA19OAR4310366. JMN
1273 was funded by a Brown University Fellowship, a Brown 2023 OVPR Seed Award, and the
1274 3CRS Project (NSF OIA 2316271). Conversations with Elizabeth Yankovsky, Anna Lo
1275 Piccolo, Joel Feske, Jochem Marotzke, Piers Forster, Lorraine E. Lisiecki, Zebedee
1276 Nicholls, Larissa Nazarenko, and Jung-Eun Lee helped to focus this work.

1277 *Data Availability Statement.*

1278 This study performed re-analysis of existing datasets openly available at locations
1279 provided in Appendix A regarding historical CO₂ and AOD, for SSP projections at
1280 <https://greenhousegases.science.unimelb.edu.au/>, and for LENS2 at
1281 https://www.earthsystemgrid.org/dataset/ucar.cgd.cesm2le.atm.proc.monthly_ave.TS.html.

This manuscript has been submitted for publication to JOURNAL OF CLIMATE (AMS). Please note that this manuscript has undergone two rounds of peer review but has yet to be formally accepted for publication. Subsequent versions of this manuscript may differ slightly in content.

1282 For critical measurements of the climate state, GMST via HadCRUT5 is at
1283 <https://www.metoffice.gov.uk/hadobs/HadCRUT5/data/current/download.html> and OHCA
1284 from Zanna et. al. (2019) is at <https://zenodo.org/record/4603700#.ZDuFNxXMI88>. Further
1285 documentation about data processing, copies of the utilized datasets, and EBM-KF Python
1286 code is available through Harvard Dataverse at <http://doi.org/10.7910/DVN/XLY8C2>.
1287

1288

APPENDICES

1289

Appendix A: Derivation of the Blind Energy-Balance Model

1290

A1: Overall Structure of the Model

1291

In the schematic diagram Fig. 2, one stream of incoming solar shortwave energy $\frac{G_{SC}}{4}$ is successively fractionated by three reflective layers until a portion warms the ground and surface ocean. Then this surface layer radiates longwave infrared energy back to space j^* , again with greenhouse “reflection” in two layers. The surface ocean warms the deep ocean with fixed thermal insulation between them.

1296

Temperature-dependent feedbacks are shown as cyclical arrows, with positive and negative feedback indicated relative to the overall energy balance. Positive feedbacks increase the energy flowing to the surface at higher surface temperatures T either by decreasing the fraction of shortwave reflection or increasing the greenhouse “reflection”. Prescribed forcings are indicated by gear symbols. Unknown coefficients $\beta_0 \beta_1 \beta_2 \beta_3$ exist respectively within the terms: $\tilde{g}(t), f_{H2O}(T), f_{aA}(T, t), f_{aS}(T)$ in addition to the unknown exponent η . All these symbols are defined below.

1303

Reiterating the overall structure in the model with discrete difference equations, T_t is the temperature of the surface in calendar year t (e.g. 2000), θ_t is the potential (or conservative) temperature of the deep ocean in that same year, and H_t is the total ocean heat content combining the heat in the surface ocean and deep ocean. The time step (abbreviated k in Kalman filter literature) is 1 year. Units are omitted in this section for brevity.

1308

$$\Delta \text{energy_total} = \mathcal{F}_{SW} - \phi_{LW} \quad (\text{A1})$$

1309

$$\Delta \text{energy_surf} = \mathcal{F}_{SW} - \phi_{LW} - Q_{\text{surf_deep}} \quad (\text{A2})$$

1310

$$\frac{T_{t+1} - T_t}{1} C_{\text{surf}} = \left(\frac{G_{SC}}{4}\right)_t * \tilde{d}_t * f_{aA}(T_t) * f_{aS}(T_t) - j^*(T_t) * \tilde{g}_t * f_{H2O}(T_t) - \gamma * (T_t - \theta_t - \zeta_0) \quad (\text{A3})$$

1311

$$\frac{\theta_{t+1} - \theta_t}{1} C_{\text{deep0}} = \gamma * (T_t - \theta_t - \zeta_0) \quad (\text{A4})$$

1312

$$H_t = (T_t - T_{1850}) * C_{\text{upper0}} + (\theta_t - \theta_{1850}) * C_{\text{deep0}} \quad (\text{A5})$$

1313

$$\theta_t = (H_t - (T_t - T_{1850}) * C_{\text{upper0}}) / C_{\text{deep0}} + \theta_{1850} \quad (\text{A6})$$

1314

$$H_{t+1} = (T_{t+1} - T_{1850}) * C_{\text{upper0}} + \gamma * (T_t - \theta_t - \zeta_0) + (\theta_t - \theta_{1850}) * C_{\text{deep0}} \quad (\text{A7})$$

1315
$$H_{t+1} - H_t = (T_{t+1} - T_t) * C_{\text{upper}0} + \gamma * (T_t - \theta_t - \zeta_0) \quad (\text{A8})$$

1316 Derivatives of θ_n :
$$\frac{\partial \theta_t}{\partial H_t} = 1/C_{\text{deep}0} \quad (\text{A9a}) \quad \frac{\partial \theta_t}{\partial T_t} = C_{\text{upper}0}/C_{\text{deep}0} \quad (\text{A9b})$$

1317 On the right side of equation A3, both the incoming shortwave radiative flux \mathcal{F}_{SW} and
 1318 outgoing longwave radiative flux ϕ_{LW} take the same form: (source $\{\frac{G_{\text{SC}}}{4}, j^*(T_t) = \sigma_{\text{sf}} T_t^4\}$) *
 1319 (prescribed attenuation $\{\tilde{d}(t), \tilde{g}(t)\}$) * (attenuations with feedback $\{f_{\alpha A}(T_b t) * f_{\alpha S}(T_t),$
 1320 $f_{H_2O}(T_t)\}$). C_{surf} , the heat capacity of the surface (including the atmosphere, thermally active
 1321 soil, and an 86m upper layer of the ocean), was known least precisely of all coefficients: $17 \pm$
 1322 $7 \text{ W (year) m}^{-2} \text{ K}^{-1}$, (Schwartz 2007). The deep ocean layer (technically the zone where most
 1323 of the ocean warming occurs) was chosen for the purpose of heat capacity estimation to be an
 1324 additional 1141m within the 71% of area covered by ocean based on previous work of this
 1325 heat transfer process. (Geoffroy, Saint-Martin et al. 2013; Hall and Fox-Kemper 2023). This
 1326 gives $C_{\text{deep}0} = 1141\text{m} * 0.71 * 1030\text{kg/m}^3 * 4180\text{Ws/kg/K} * 1 \text{ yr} / (3.154 * 10^7\text{s}) = 155.7 \text{ W}$
 1327 $(\text{year}) \text{ m}^{-2} \text{ K}^{-1}$. Constants γ, ζ_0 form a linear heat flux $Q_{\text{surf-deep}}$ into the deep ocean, as
 1328 discussed below. Radiative fluxes are signified in this text by the symbol ϕ , followed by
 1329 specific details of that flux.

1330

1331 ***A2: Functional Forms of Components***

1332 For brevity, derivations and detailed explanations of each of these components has
 1333 been moved to the Supplement (A1 & A2). Here the functional form of each component is
 1334 provided.

1335
$$Q_{\text{surf-deep}} = \gamma * (\Delta T_t - \Delta \theta_t) = \gamma * (T_t - \theta_t - T_{1850} + \theta_{1850}) \quad (\text{A9})$$

1336 The heat flowing from the surface layer into the deep ocean.

1337

1338
$$\tilde{d}(t) \approx \frac{9.07}{\text{AOD}_t + 9.73} \quad (\text{A10})$$

1339 The fraction of shortwave (incoming) light reflected by stratospheric (volcanic) aerosols.

1340

1341
$$\tilde{g}(t) = 1 - \beta_0 \log_{10}([\text{eCO}_2]_t) < 1 \quad (\text{A11})$$

1342 The fraction of longwave radiation absorbed by greenhouse gases.

1343

$$1344 \quad j^*(T_t) = \sigma_{sf} T_t^4 \quad (A12)$$

1345 Blackbody radiation, source of longwave outgoing radiation.

$$1346 \quad \phi_{LW}(\text{out}) = j^*(T_t) - \frac{\phi_{LW}(\text{absorbed})}{2} = j^*(T_t) * \tilde{g}(t) * f_{H2O}(T_t) \quad (A13)$$

1347 Two simplified expressions of how longwave radiation is blocked, in this paper we use the
 1348 one at right which relates CO₂ to a fraction absorbed (similarly to albedo). Other authors favor
 1349 the expression in the center, as it relates the absorption of a greenhouse gas to a power (in
 1350 W/m²) rather than an expression.

$$1351 \quad \phi_{LW}^{CO2} = 12.74 \log_{10}([eCO_2]_t) - 31.55 \quad (A14)$$

1352 The expression reported by Forster (2023) for the blocked outgoing longwave radiation – for
 1353 our EBM this expression must be converted into a fraction to solve for β_o .

1354

$$1355 \quad f_{H2O}(T_t) \doteq \beta_1 (1/T_t)^\eta \approx 1 - (1 + \beta_1 (T_{2002})^{-\eta} - \beta_1 \eta (T_{2002})^{-\eta-1} (T_t - T_{2002})) \quad (A15)$$

$$1356 \quad f_{aA}(T_b t) \doteq 0.834 \left(1 + \beta_2 (T_t - T_{2002}) \right) + \frac{AC_n - AC_{2002}}{\frac{GSE_{d2002}}{4}} \quad (A16)$$

$$1357 \quad f_{aS}(T_t) \doteq 0.909 \left(1 + \beta_3 (T_t - T_{2002}) \right) \quad (A17)$$

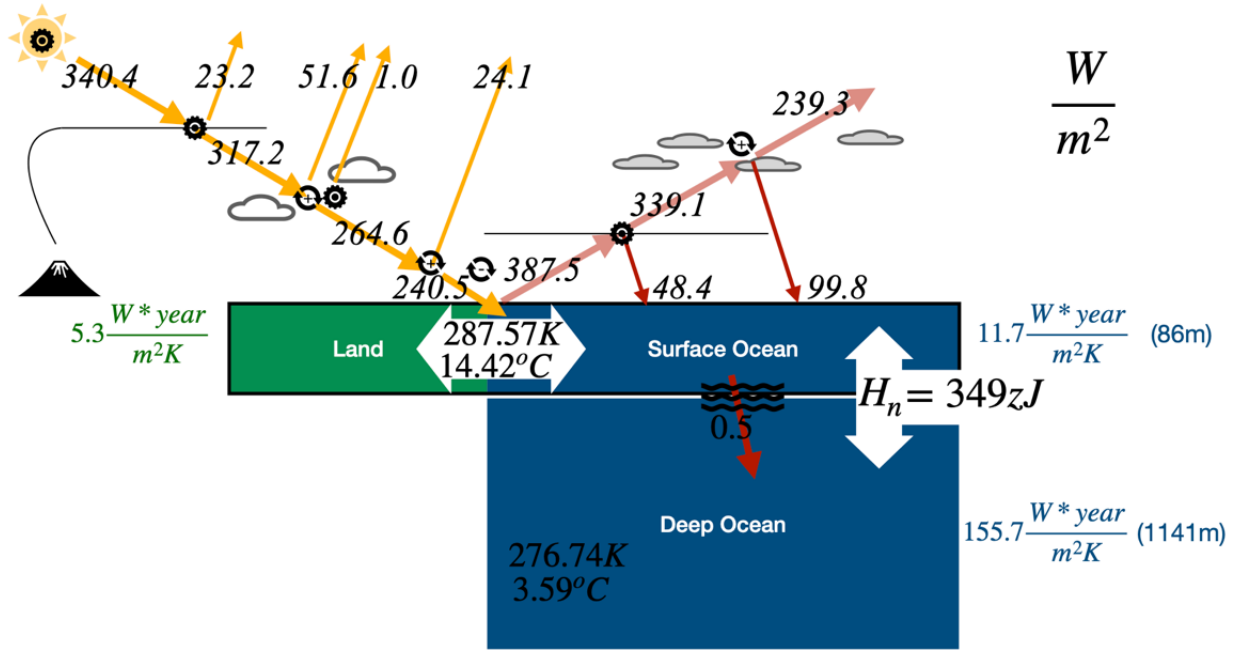
1358 Functions proposed by the authors for the water feedback (on absorbing fraction of longwave
 1359 radiation), atmospheric albedo feedback, and surface albedo feedback. Note that the values
 1360 of 0.834 and 0.909 came from the CERES satellite in the early 2000s. Solving for all the
 1361 coefficients, we find from feedbacks assessed in ESM (CMIP6 & AR6):

$$1362 \quad \eta = 1.615, \beta_2 = 0.00136 \text{ K}^{-1}, \beta_3 = 0.00163 \text{ K}^{-1} \quad (A18)$$

1363 And by assuming the climate was at equilibrium before 1850 and assimilating the longwave
 1364 anthropogenic greenhouse gas and anthropogenic aerosol energy fluxes published by Forster
 1365 (2023) at <https://github.com/ClimateIndicator/forcing-timeseries/tree/main/output>:

$$1366 \quad 6593.57 \approx \beta_1 \quad \text{and} \quad 0.04660 \approx \beta_o \quad (A19)$$

1367 This yields the following energy fluxes in 2002 (compare to Wild, Folini et al. (2015), Wild,
 1368 Hakuba et. al. Wild, Hakuba et al. (2019))



1369

1370 Fig. A1: Diagram with energy fluxes, temperatures, and total ocean heat content for the blind
 1371 run of energy balance model in 2002 (when many of the reflectivity values were first
 1372 measured by the CERES satellite). All numbers without units are in W/m^2 .
 1373

1374 **A3: Differentiating to Find the Jacobian Matrix**

1375 This yielded a blind energy-balance model with good skill at predicting the GMST
 1376 (orange dashed line in Fig. 2), $r^2 = 0.902$. Rewriting the overall model with β coefficients,

$$1377 \quad T_{t+1} = T_t + \frac{\left(\frac{G_{SC}}{4}\right)_t 0.758 * 9.068}{C_{surf} (AOD_t + 9.73)} \left(1 + \beta_2 (T_t - 287.5) + \frac{AC_t - AC_{2002}}{\frac{G_{SC}}{4} \overline{d_{2002}} 0.834} \right) (1 + \beta_3 (T_t - 287.5))$$

$$1378 \quad - \frac{\sigma_{sf} \beta_1}{C_{surf}} (T_t)^{2.39} (1 - \beta_0 \log_{10}([eCO_2]_t)) - \frac{\gamma}{C_{surf}} (T_t - \theta_t - 10) \quad (A20)$$

1379 Derivatives of θ_n : $\frac{\partial \theta_t}{\partial H_t} = 1/C_{deep}$ (A9a) $\frac{\partial \theta_t}{\partial T_t} = C_{upper0}/C_{deep}$ (A9b)

$$1380 \quad \frac{\partial T_{t+1}}{\partial T_t} = 1 + \frac{137.6}{AOD_t + 9.73} \left(\beta_2 + \beta_3 + 2\beta_2\beta_3 (T_t - 287.5) + \beta_3 \frac{AC_t - AC_{2002}}{G_0^* \overline{d_{2002}} 0.834} \right)$$

$$1381 \quad - \frac{2.39 \sigma_{sf} \beta_1}{C_{surf}} (T_t)^{1.39} (1 - \beta_0 \log_{10}([eCO_2]_t)) - \frac{\gamma}{C_{surf}} (1 - C_{upper0}/C_{deep}) \quad (A21)$$

$$1382 \quad \frac{\partial T_{t+1}}{\partial H_t} = \frac{\gamma}{C_{surf}} * \frac{\partial \theta_t}{\partial H_t} = \frac{\gamma}{C_{surf} C_{deep}} \quad (A22)$$

1383 The ocean heat content update equation ($r^2 = 0.907$ blind) and related partial derivatives are:

$$1384 \quad H_{t+1} = (T_{t+1} - T_{1850}) * C_{upper0} + \gamma * (T_t - \theta_t - \zeta) + (\theta_t - \theta_{1850}) * C_{deep} \quad (A23)$$

This manuscript has been submitted for publication to JOURNAL OF CLIMATE (AMS). Please note that this manuscript has undergone two rounds of peer review but has yet to be formally accepted for publication. Subsequent versions of this manuscript may differ slightly in content.

$$1385 \quad \frac{\partial H_{t+1}}{\partial H_t} = C_{\text{upper0}} \frac{\partial T_{t+1}}{\partial H_t} + \gamma * \left(0 - \frac{\partial \theta_t}{\partial H_t} \right) + C_{\text{deep}} \frac{\partial \theta_t}{\partial H_t} = \frac{\gamma}{C_{\text{deep}}} * \left(\frac{C_{\text{upper0}}}{C_{\text{surf}}} - 1 \right) + 1 \quad (\text{A24})$$

$$1386 \quad \frac{\partial H_{t+1}}{\partial T_t} = C_{\text{upper0}} * \frac{\partial T_{t+1}}{\partial T_t} + \gamma * \left(1 - \frac{C_{\text{upper0}}}{C_{\text{deep}}} \right) + C_{\text{upper0}} \quad (\text{A25})$$

1387

1388

1389

Appendix B: Generation of Volcanic Eruption Samplings

1390

As can be appreciated in Fig. B1a, long periods of no major volcanic eruptions (for

1391

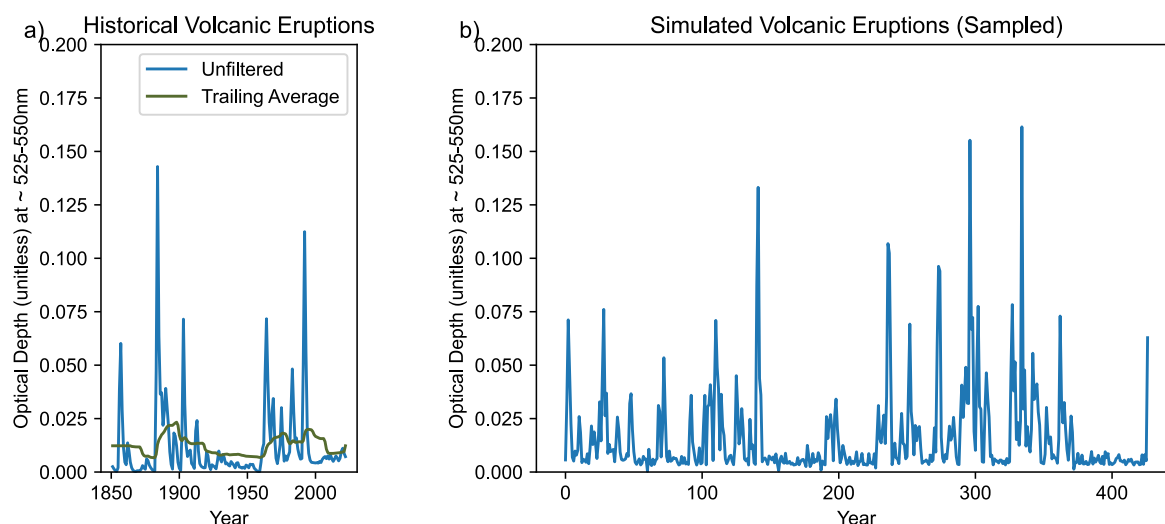
instance 1935-1960) alternated with periods of many eruptions occurring in rapid succession

1392

(1883-1914, 1960-1994). Perhaps this observed pattern has some relation to magma or

1393

tectonic dynamics, but it prevented one Poisson distribution from describing the data well.



1394

1395 Fig. B1: Comparison of Historical Volcanic Eruptions (B1a) with Simulated Volcanic
1396 Eruptions (B1b), generated from a combination of several probability distributions. Observe
1397 in panel a that the unfiltered aerosol optical depths (AOD_t) are plotted in blue, whereas the
1398 trailing average filter is plotted in green (it combines 15 years of a trailing average and 15
1399 years of future projections at the mean AOD).

1400

1401 Eruptions that occurred within 3 years were indistinguishable in the historical dataset,

1402

so the minimum time interval between simulated volcanic eruptions was 2.6 years plus a

1403

sample (Table B1) from the exponential mixture model i_t (Okada, Yamanishi et al. 2020).

1404

These intervals were rounded to integers. Similarly, the size of each volcanic eruption h_t was

1405

approximated using another shifted exponential distribution. The preceding year and two

1406

years following the eruption peak were positive fractions of the maximum aerosol optical

1407

depth, with Gaussian blur. Similarly, non-volcanic years were positive Gaussian noise (Table

1408

B2). Fig. B1b shows a sample from this combined generating function.

1409

This manuscript has been submitted for publication to JOURNAL OF CLIMATE (AMS). Please note that this manuscript has undergone two rounds of peer review but has yet to be formally accepted for publication. Subsequent versions of this manuscript may differ slightly in content.

Exponential Distribution	Rand. Var.	Scale (units)	P(if mixture)
Interval Between: $\text{round}(i_{t,0} + 2.6)$	$i_{t,0} \sim \text{Exp}$	2.263 (years)	88.9%
Interval Between: $\text{round}(i_{t,1} + 2.6)$	$i_{t,1} \sim \text{Exp}$	24.2 (years)	11.1%
Peak Size: $\text{AOD}_t = h_t + 0.0082$	$h_t \sim \text{Exp}$	0.0339 (m)	only “eruption” years

1410 Table B1. Exponential Parameters of Volcano Generating Function. This generating function
 1411 starts with a list of zero values for all AOD_t , and first samples several of these t years to be
 1412 major volcanic eruptions. “Interval Between” refers to the interval in years between two
 1413 successive major volcanic eruptions.
 1414

Gaussian Distribution	Rand. Var.	Mean μ (units)	Std Dev σ
Pre-Peak: $\text{AOD}_{t-1} = a_{(-1)} * \text{AOD}_t$	$a_{(-1)} \sim \text{Norm} > 0$	0.51	0.25
Post-Peak 1: $\text{AOD}_{t+1} = a_1 * \text{AOD}_t$	$a_1 \sim \text{Norm} > 0$	0.61	0.16
Post-Peak 2: $\text{AOD}_{t+2} = a_2 * \text{AOD}_t$	$a_2 \sim \text{Norm} > 0$	0.32	0.16
Other Years: $\text{AOD}_t = a_0$	$a_0 \sim \text{Norm} > 0$	0.00371 (m)	0.00286 (m)

1415 Table B2. Gaussian Parameters of Volcano Generating Function. These distributions are
 1416 sampled after the major eruptions have already been filled in by the exponential distributions
 1417 in Table B1.
 1418
 1419

Appendix C: Glossary of Mathematical Symbols and Notation

Symbol	Meaning	Context	Units
p , $\mathbb{P}(\text{event})$	Probability of the observed result for a particular hypothesis test (e.g. that the slope is positive)	Statistics	[0-1]
r^2	Coefficient of determination: fraction of variance explained by a model	Statistics	[0-1]
σ $\pm 2\sigma = 95\% \text{ CI}$	Standard deviation ($\sqrt{\text{Variance}}$) 95% confidence interval (extremely likely) under Gaussian distribution	Statistics	any
$\text{Cov}()$	Covariance of a random vector (here length 2)	Statistics	sq. matrix
t, k	Time index, time step	KF, EBM	year
T_t	GMST surface temperature climate state, idealized	EBM-KF	K ($^{\circ}\text{C}$)
θ_t	Deep ocean potential temperature state, idealized	EBM-KF	K
H_t	Ocean heat content anomaly, idealized	EBM-KF	$\frac{W \text{ yr}}{m^2}$ (ZJ)
$u_t = [eCO_2]_t, AOD_t, AC_t, (\frac{G_{SC}}{4})_t$	Time-varying concentrations in the atmosphere	EBM	ppm, \emptyset , W/m^2
$[\tilde{T}_{t+1}, \tilde{H}_{t+1}] = F(\tilde{T}_t, \tilde{H}_t, u_t)$	Blind energy balance model, which is entirely deterministic based on prior climate state	EBM	$[K, \frac{W \text{ yr}}{m^2}]$
$\Phi_t = \frac{\partial F(\mathbf{x}; u_t)}{\partial \mathbf{x}} \Big _{\mathbf{x}=\hat{\mathbf{x}}_{t-1}}$	Linearized tensor derivative of the (blind) EBM model	EBM-KF	$\begin{bmatrix} \emptyset & K / \frac{W \text{ yr}}{m^2} \\ \frac{W \text{ yr}}{m^2} / K & \emptyset \end{bmatrix}$
$\mathbf{x}_{\tilde{t}} = [T_t, H_t]$	Idealized true climate state, with dynamic model noise	EBM -KF	$[K, \frac{W \text{ yr}}{m^2}]$
$\hat{\mathbf{x}}_t = [\hat{T}_t, \hat{H}_t]$	Estimate of the underlying climate state	EBM -KF	$[K, \frac{W \text{ yr}}{m^2}]$

$y_t = [Y_t, \psi_t]$	Measurements with noise of the climate state, from HadCRUT5 (Morice, Kennedy et al. 2021) and Zanna et al. (2019).	EBM -KF	$[K, \frac{W \text{ yr}}{m^2}]$
$Q = \text{COV}[w_t]$	Assumed dynamic model error and model covariance matrix	KF	$\begin{bmatrix} K^2 & K \frac{W \text{ yr}}{m^2} \\ K \frac{W \text{ yr}}{m^2} & (\frac{W \text{ yr}}{m^2})^2 \end{bmatrix}$
$R = \text{COV}[v_t]$	Assumed measurement error and measurement covariance matrix	KF	$\begin{bmatrix} K^2 & K \frac{W \text{ yr}}{m^2} \\ K \frac{W \text{ yr}}{m^2} & (\frac{W \text{ yr}}{m^2})^2 \end{bmatrix}$
$\overline{30Y_t}$ $\overline{30\psi_t}$	30-year running mean of measurements, undefined before 1865 or after 2008	Prior climate methods	$[K, \frac{W \text{ yr}}{m^2}]$ K
$R_t = R_t^{var} + R^{const}$ $Q = R^{const}/30$	Actual covariance matrices used in the EBM-KF, defined to mimic the statistics of the 30-year running mean	EBM-KF	$\begin{bmatrix} K^2 & K \frac{W \text{ yr}}{m^2} \\ K \frac{W \text{ yr}}{m^2} & (\frac{W \text{ yr}}{m^2})^2 \end{bmatrix}$
$\hat{x}_{t t-1}$ $P_{t t-1}$	KF forecast state projection and forecast covariance projection (before new measurement)	KF	$[K, \frac{W \text{ yr}}{m^2}]$ $\begin{bmatrix} K^2 & K \frac{W \text{ yr}}{m^2} \\ K \frac{W \text{ yr}}{m^2} & (\frac{W \text{ yr}}{m^2})^2 \end{bmatrix}$
z_t S_t	Innovation residual, Innovation covariance	KF	$[K, \frac{W \text{ yr}}{m^2}]$ $\begin{bmatrix} K^2 & K \frac{W \text{ yr}}{m^2} \\ K \frac{W \text{ yr}}{m^2} & (\frac{W \text{ yr}}{m^2})^2 \end{bmatrix}$
K_t	Kalman gain: weight on innovation to correct state	KF	$\begin{bmatrix} \emptyset & \emptyset \\ \emptyset & \emptyset \end{bmatrix}$

\hat{x}_t P_t	KF posterior estimated state projection and state variance (after measurement)	KF	$[K, \frac{W yr}{m^2}]$ $\begin{bmatrix} K^2 & K \frac{W yr}{m^2} \\ K \frac{W yr}{m^2} & (\frac{W yr}{m^2})^2 \end{bmatrix}$
$\hat{K}_t, \hat{x}_t, \hat{P}_t$	RTS re-estimated Kalman gain, state estimate, and state covariance, following backward sweep	RTS	as above
$(Y_t)_j, (\psi_t)_j$	The j^{th} ensemble member's annual mean at time t of air temperature or ocean heat content	LENS2	$K, \frac{W yr}{m^2}$
$\overline{(Y_t)}_j$	Ensemble average (across all members) at year t	LENS2	K
$\overline{(21Y_t)}_j$	The 21-year running mean of ensemble member j	LENS2	K
$\overline{\overline{(21Y_t)}_j}$	The cross-ensemble average of all 21-year running means	LENS2	K
γ	Thermal conductivity between layers of the ocean	EBM	$\frac{W yr}{m^2 K}$
$\mathcal{F}_{SW}, \phi_{LW}$	Net radiative fluxes (shortwave and longwave) at the top of the atmosphere	EBM	W
$\Delta\text{Energy_surf}$ $Q_{\text{surf_deep}}$	Net heat flow into the surface and deep ocean layers respectively	EBM	W

This manuscript has been submitted for publication to JOURNAL OF CLIMATE (AMS). Please note that this manuscript has undergone two rounds of peer review but has yet to be formally accepted for publication. Subsequent versions of this manuscript may differ slightly in content.

$C_{\text{surf}} ; C_{\text{upper0}} ; C_{\text{deep0}}$	Heat capacities of the surface, surface ocean, and deep ocean	EBM	$\frac{W \text{ yr}}{m^2 K}$
$\left(\frac{G_{sf}}{4}\right)_t$ $j^* = \sigma_{sf} T^4$	Sources of shortwave (total solar irradiance) and longwave (blackbody or Planck feedback)	EBM	$\frac{W}{m^2}$
\tilde{d}_t, \tilde{g}_t	Prescribed, time-varying attenuations from atmospheric dust and longwave radiation respectively	EBM	\emptyset
$f_{aA}(T, t) * f_{aS}(T)$ $f_{H2O}(T)$	Attenuations due to albedo of the atmosphere, albedo of the surface, and longwave absorbing water vapor (all with feedback from T_t)	EBM	\emptyset
ζ_0	Equilibrium temperature difference between the surface and deep ocean.	EBM	K
ζ_1	Baseline temperature for HadCRUT5 to achieve the appropriate 1960-1989 climate normal (Jones and Harpham 2013)	EBM	K
σ_{sf}	Stefan-Boltzman constant $= 5.670 \cdot 10^{-8}$	EBM	$\frac{W m^2}{K^4}$
β_0	Solved coefficient on $\log_{10}([eCO_2]_t)$ within a	EBM	\emptyset

This manuscript has been submitted for publication to JOURNAL OF CLIMATE (AMS). Please note that this manuscript has undergone two rounds of peer review but has yet to be formally accepted for publication. Subsequent versions of this manuscript may differ slightly in content.

	sequential filter atmosphere approximation		
β_1, η	Solved coefficient and exponent for the $f_{H_2O}(T)$ water vapor feedback on longwave	EBM	\emptyset
β_2, β_3	Solved coefficients for $f_{aA}(T, t) * f_{aS}(T)$, atmosphere and surface albedo feedbacks.	EBM	\emptyset
$c_1, c_2,$ c_3, c_4	Simplifications of constants within the EBM, see Eq. 4-6 and Table 1.	EBM	$K^{-3+\eta}, \frac{K m^2}{W},$ $\frac{W}{m^2}, \emptyset$ (AOD)
q	Location of a climate policy threshold	EBM-KF thresholds	K
$i_{t,0} i_{t,1}$	Exponential mixture random variables to determine the interval between major eruptions	Volcanoes	years
h_t	Exponential random variable to determine size of a particular major eruption	Volcanoes	\emptyset (AOD)
$a_{(-1)}, a_1, a_2, a_0$	Truncated gaussian distributions to determine the atmospheric optical depth in eruption-adjacent and non-eruption years.	Volcanoes	\emptyset (AOD)

1421 Table C1: Glossary of Mathematical Symbols

1422

1423

1424

REFERENCES

- 1425 Abraham, J. P., M. Baringer, N. L. Bindoff, T. Boyer, L. J. Cheng, J. A. Church, J. L.
1426 Conroy, C. M. Domingues, J. T. Fasullo, J. Gilson, G. Goni, S. A. Good, J. M. Gorman, V.
1427 Gouretski, M. Ishii, G. C. Johnson, S. Kizu, J. M. Lyman, A. M. Macdonald, W. J.
1428 Minkowycz, S. E. Moffitt, M. D. Palmer, A. R. Piola, F. Reseghetti, K. Schuckmann, K. E.
1429 Trenberth, I. Velicogna and J. K. Willis (2013). "A review of global ocean temperature
1430 observations: Implications for ocean heat content estimates and climate change." Reviews of
1431 Geophysics **51**(3): 450-483 DOI: <https://doi.org/10.1002/rog.20022>.
- 1432 Armour, K. C., C. M. Bitz and G. H. Roe (2013). "Time-Varying Climate Sensitivity from
1433 Regional Feedbacks." Journal of Climate **26**(13): 4518-4534 DOI:
1434 <https://doi.org/10.1175/JCLI-D-12-00544.1>.
- 1435 Benhamou, E. (2018). "Kalman filter demystified: from intuition to probabilistic graphical
1436 model to real case in financial markets." arXiv e-prints Statistical Finance (q-
1437 fin.ST)(arXiv:1811.11618) DOI: <https://doi.org/10.48550/arXiv.1811.11618>.
- 1438 Betts, R., S. Belcher, L. Hermanson, A. Tank, J. Lowe, C. Jones, C. Morice, N. Rayner, A.
1439 Scaife and P. Stott (2023). "Approaching 1.5 °C: how will we know we've reached this
1440 crucial warming mark?" Nature **624**: 33-35 DOI: 10.1038/d41586-023-03775-z.
- 1441 Bouttier, F. (1996). Application of Kalman filtering to numerical weather prediction.
1442 Workshop on non-linear aspects of data assimilation, Shinfield Park, Reading, ECMWF.
- 1443 Budyko, M. I. (1969). "The effect of solar radiation variations on the climate of the Earth."
1444 Tellus **21**(5): 611-619 DOI: 10.3402/tellusa.v21i5.10109.
- 1445 Buizza, R., M. Milleer and T. N. Palmer (1999). "Stochastic representation of model
1446 uncertainties in the ECMWF ensemble prediction system." Quarterly Journal of the Royal
1447 Meteorological Society **125**(560): 2887-2908 DOI: <https://doi.org/10.1002/qj.49712556006>.
- 1448 Burgess, S. (2024) "Copernicus: In 2024, the world experienced the warmest January on
1449 record." CLIMATE BULLETINS: NEWSFLASH **Jan 2024**.
- 1450 Carré, M., J. P. Sachs, J. M. Wallace and C. Favier (2012). "Exploring errors in paleoclimate
1451 proxy reconstructions using Monte Carlo simulations: paleotemperature from mollusk and
1452 coral geochemistry." Clim. Past **8**(2): 433-450 DOI: 10.5194/cp-8-433-2012.
- 1453 Ceppi, P. and P. Nowack (2021). "Observational evidence that cloud feedback amplifies
1454 global warming." Proceedings of the National Academy of Sciences **118**(30): e2026290118
1455 DOI: doi:10.1073/pnas.2026290118.
- 1456 Chan, D. and P. Huybers (2021). "Correcting Observational Biases in Sea Surface
1457 Temperature Observations Removes Anomalous Warmth during World War II." Journal of
1458 Climate **34**(11): 4585-4602 DOI: <https://doi.org/10.1175/JCLI-D-20-0907.1>.
- 1459 Chen, Z., C. Heckman, S. Julier and N. Ahmed (2018). Weak in the NEES?: Auto-Tuning
1460 Kalman Filters with Bayesian Optimization DOI: 10.23919/ICIF.2018.8454982.
- 1461 Chen, Z., C. Heckman, S. J. Julier and N. R. Ahmed (2021). "Time Dependence in Kalman
1462 Filter Tuning." 2021 IEEE 24th International Conference on Information Fusion (FUSION):
1463 1-8.
- 1464 Cheng, L., K. E. Trenberth, J. Fasullo, T. Boyer, J. Abraham and J. Zhu (2017). "Improved
1465 estimates of ocean heat content from 1960 to 2015." Science Advances **3**(3): e1601545 DOI:
1466 10.1126/sciadv.1601545.

This manuscript has been submitted for publication to JOURNAL OF CLIMATE (AMS). Please note that this manuscript has undergone two rounds of peer review but has yet to be formally accepted for publication. Subsequent versions of this manuscript may differ slightly in content.

- 1467 Cheng, L., K. von Schuckmann, J. P. Abraham, K. E. Trenberth, M. E. Mann, L. Zanna, M.
1468 H. England, J. D. Zika, J. T. Fasullo, Y. Yu, Y. Pan, J. Zhu, E. R. Newsom, B. Bronselaer
1469 and X. Lin (2022). "Past and future ocean warming." Nature Reviews Earth & Environment
1470 **3**(11): 776-794 DOI: 10.1038/s43017-022-00345-1.
- 1471 Coddington, O., J. L. Lean, D. Lindholm, P. Pilewskie, M. Snow and N. C. Program (2017).
1472 NOAA Climate Data Record (CDR) of Total Solar Irradiance (TSI), NRLTSI Version 2.1. N.
1473 N. C. f. E. Information DOI: <https://doi.org/10.7289/V56W985W>.
- 1474 Collins, M., R. Knutti, J. Arblaster, J. L. Dufresne, T. Fichet, P. Friedlingstein, X. Gao, W.
1475 J. Gutowski, T. Johns, G. Krinner, M. Shongwe, C. Tebaldi, A. J. Weaver and M. Wehner
1476 (2013). Long-term climate change: Projections, commitments and irreversibility. Climate
1477 Change 2013: The Physical Science Basis. Contribution of Working Group I to the Fifth
1478 Assessment Report of the Intergovernmental Panel on Climate Change. T. F. Stocker, D. Qin,
1479 G. K. Plattner et al. Cambridge, UK, Cambridge University Press: 1029-1136 DOI:
1480 10.1017/CBO9781107415324.024.
- 1481 Compo, G. P., J. S. Whitaker, P. D. Sardeshmukh, N. Matsui, R. J. Allan, X. Yin, B. E.
1482 Gleason, R. S. Vose, G. Rutledge, P. Bessemoulin, S. Brönnimann, M. Brunet, R. I.
1483 Crouthamel, A. N. Grant, P. Y. Groisman, P. D. Jones, M. C. Kruk, A. C. Kruger, G. J.
1484 Marshall, M. Maugeri, H. Y. Mok, Ø. Nordli, T. F. Ross, R. M. Trigo, X. L. Wang, S. D.
1485 Woodruff and S. J. Worley (2011). "The Twentieth Century Reanalysis Project." Quarterly
1486 Journal of the Royal Meteorological Society **137**(654): 1-28 DOI:
1487 <https://doi.org/10.1002/qj.776>.
- 1488 Duffy, M. L., B. Medeiros, A. Gettelman and T. Eidhammer (2023). "Perturbing parameters
1489 to understand cloud contributions to climate change." Journal of Climate [**Preprint**].
- 1490 Edwards, T. L., S. Nowicki, B. Marzeion, R. Hock, H. Goelzer, H. Seroussi, N. C. Jourdain,
1491 D. A. Slater, F. E. Turner, C. J. Smith, C. M. McKenna, E. Simon, A. Abe-Ouchi, J. M.
1492 Gregory, E. Larour, W. H. Lipscomb, A. J. Payne, A. Shepherd, C. Agosta, P. Alexander, T.
1493 Albrecht, B. Anderson, X. Asay-Davis, A. Aschwanden, A. Barthel, A. Bliss, R. Calov, C.
1494 Chambers, N. Champollion, Y. Choi, R. Cullather, J. Cuzzone, C. Dumas, D. Felikson, X.
1495 Fettweis, K. Fujita, B. K. Galton-Fenzi, R. Gladstone, N. R. Golledge, R. Greve, T.
1496 Hattermann, M. J. Hoffman, A. Humbert, M. Huss, P. Huybrechts, W. Immerzeel, T. Kleiner,
1497 P. Kraaijenbrink, S. Le clec'h, V. Lee, G. R. Leguy, C. M. Little, D. P. Lowry, J.-H. Malles,
1498 D. F. Martin, F. Maussion, M. Morlighem, J. F. O'Neill, I. Nias, F. Pattyn, T. Pelle, S. F.
1499 Price, A. Quiquet, V. Radić, R. Reese, D. R. Rounce, M. Rückamp, A. Sakai, C. Shafer, N.-J.
1500 Schlegel, S. Shannon, R. S. Smith, F. Straneo, S. Sun, L. Tarasov, L. D. Trusel, J. Van
1501 Breedam, R. van de Wal, M. van den Broeke, R. Winkelmann, H. Zekollari, C. Zhao, T.
1502 Zhang and T. Zwinger (2021). "Projected land ice contributions to twenty-first-century sea
1503 level rise." Nature **593**(7857): 74-82 DOI: 10.1038/s41586-021-03302-y.
- 1504 Emile-Geay, J., N. P. McKay, D. S. Kaufman, L. von Gunten, J. Wang, K. J. Anchukaitis, N.
1505 J. Abram, J. A. Addison, M. A. J. Curran, M. N. Evans, B. J. Henley, Z. Hao, B. Martrat, H.
1506 V. McGregor, R. Neukom, G. T. Pederson, B. Stenni, K. Thirumalai, J. P. Werner, C. Xu, D.
1507 V. Divine, B. C. Dixon, J. Gergis, I. A. Mundo, T. Nakatsuka, S. J. Phipps, C. C. Routson, E.
1508 J. Steig, J. E. Tierney, J. J. Tyler, K. J. Allen, N. A. N. Bertler, J. Björklund, B. M. Chase,
1509 M.-T. Chen, E. Cook, R. de Jong, K. L. DeLong, D. A. Dixon, A. A. Ekaykin, V. Ersek, H.
1510 L. Filipsson, P. Francus, M. B. Freund, M. Frezzotti, N. P. Gaire, K. Gajewski, Q. Ge, H.
1511 Goosse, A. Gornostaeva, M. Grosjean, K. Horiuchi, A. Hormes, K. Husum, E. Isaksson, S.
1512 Kandasamy, K. Kawamura, K. H. Kilbourne, N. Koç, G. Leduc, H. W. Linderholm, A. M.
1513 Lorrey, V. Mikhalenko, P. G. Mortyn, H. Motoyama, A. D. Moy, R. Mulvaney, P. M. Munz,

This manuscript has been submitted for publication to JOURNAL OF CLIMATE (AMS). Please note that this manuscript has undergone two rounds of peer review but has yet to be formally accepted for publication. Subsequent versions of this manuscript may differ slightly in content.

- 1514 D. J. Nash, H. Oerter, T. Opel, A. J. Orsi, D. V. Ovchinnikov, T. J. Porter, H. A. Roop, C.
1515 Saenger, M. Sano, D. Sauchyn, K. M. Saunders, M.-S. Seidenkrantz, M. Severi, X. Shao, M.-
1516 A. Sicre, M. Sigl, K. Sinclair, S. St. George, J.-M. St. Jacques, M. Thamban, U. Kuwar
1517 Thapa, E. R. Thomas, C. Turney, R. Uemura, A. E. Viau, D. O. Vladimirova, E. R. Wahl, J.
1518 W. C. White, Z. Yu, J. Zinke and P. A. k. Consortium (2017). "A global multiproxy database
1519 for temperature reconstructions of the Common Era." *Scientific Data* **4**(1): 170088 DOI:
1520 10.1038/sdata.2017.88.
- 1521 Feng, R., B. L. Otto-Bliesner, E. C. Brady and N. Rosenbloom (2020). "Increased Climate
1522 Response and Earth System Sensitivity From CCSM4 to CESM2 in Mid-Pliocene
1523 Simulations." *Journal of Advances in Modeling Earth Systems* **12**(8): e2019MS002033 DOI:
1524 <https://doi.org/10.1029/2019MS002033>.
- 1525 Filar, J. A., P. S. Gaertner and M. A. Janssen (1996). An Application of Optimization to the
1526 Problem of Climate Change. *State of the Art in Global Optimization: Computational Methods*
1527 *and Applications*. C. A. Floudas and P. M. Pardalos. Boston, MA, Springer US: 475-498
1528 DOI: 10.1007/978-1-4613-3437-8_29.
- 1529 Forster, P., T. Storelvmo, K. Armour, W. Collins, J. L. Dufresne, D. Frame, D. J. Lunt, T.
1530 Mauritsen, M. D. Palmer, M. Watanabe, M. Wild and H. Zhang (2021). The Earth's Energy
1531 Budget, Climate Feedbacks, and Climate Sensitivity. *Climate Change 2021: The Physical*
1532 *Science Basis. Contribution of Working Group I to the Sixth Assessment Report of the*
1533 *Intergovernmental Panel on Climate Change*. V. Masson-Delmotte, P. Zhai, A. Pirani et al.
1534 Cambridge, United Kingdom and New York, NY, USA, Cambridge University Press: 923–
1535 1054 DOI: 10.1017/9781009157896.009.
- 1536 Forster, P. M., C. J. Smith, T. Walsh, W. F. Lamb, R. Lamboll, M. Hauser, A. Ribes, D.
1537 Rosen, N. Gillett, M. D. Palmer, J. Rogelj, K. von Schuckmann, S. I. Seneviratne, B. Trewin,
1538 X. Zhang, M. Allen, R. Andrew, A. Birt, A. Borger, T. Boyer, J. A. Broersma, L. Cheng, F.
1539 Dentener, P. Friedlingstein, J. M. Gutiérrez, J. Gütschow, B. Hall, M. Ishii, S. Jenkins, X.
1540 Lan, J. Y. Lee, C. Morice, C. Kadow, J. Kennedy, R. Killick, J. C. Minx, V. Naik, G. P.
1541 Peters, A. Pirani, J. Pongratz, C. F. Schleussner, S. Szopa, P. Thorne, R. Rohde, M. Rojas
1542 Corradi, D. Schumacher, R. Vose, K. Zickfeld, V. Masson-Delmotte and P. Zhai (2023).
1543 "Indicators of Global Climate Change 2022: annual update of large-scale indicators of the
1544 state of the climate system and human influence." *Earth Syst. Sci. Data* **15**(6): 2295-2327
1545 DOI: 10.5194/essd-15-2295-2023.
- 1546 Fox-Kemper, B., H. T. Hewitt, C. Xiao, G. Aðalgeirsdóttir, S. S. Drijfhout, T. L. Edwards, N.
1547 R. Golledge, M. Hemer, R. E. Kopp, G. Krinner, A. Mix, D. Notz, S. Nowicki, I. S. Nurhati,
1548 L. Ruiz, J. B. Sallée, A. B. A. Slangen and Y. Yu (2021). Ocean, Cryosphere and Sea Level
1549 Change. *Climate Change 2021: The Physical Science Basis. Contribution of Working Group*
1550 *I to the Sixth Assessment Report of the Intergovernmental Panel on Climate Change*. V.
1551 Masson-Delmotte, P. Zhai, A. Pirani et al. Cambridge, United Kingdom and New York, NY,
1552 USA, Cambridge University Press: 1211–1362 DOI: 10.1017/9781009157896.011.
- 1553 Friedrich, T., A. Timmermann, M. Tigchelaar, O. Elison Timm and A. Ganopolski (2016).
1554 "Nonlinear climate sensitivity and its implications for future greenhouse warming." *Science*
1555 *Advances* **2**(11): e1501923 DOI: doi:10.1126/sciadv.1501923.
- 1556 Fujimori, S., T. Hasegawa, T. Masui, K. Takahashi, D. S. Herran, H. Dai, Y. Hijioka and M.
1557 Kainuma (2017). "SSP3: AIM implementation of Shared Socioeconomic Pathways." *Global*
1558 *Environmental Change* **42**: 268-283 DOI: <https://doi.org/10.1016/j.gloenvcha.2016.06.009>.

This manuscript has been submitted for publication to JOURNAL OF CLIMATE (AMS). Please note that this manuscript has undergone two rounds of peer review but has yet to be formally accepted for publication. Subsequent versions of this manuscript may differ slightly in content.

- 1559 García-Pintado, J. and A. Paul (2018). "Evaluation of iterative Kalman smoother schemes for
1560 multi-decadal past climate analysis with comprehensive Earth system models." Geosci.
1561 Model Dev. **11**(12): 5051-5084 DOI: 10.5194/gmd-11-5051-2018.
- 1562 Geoffroy, O., D. Saint-Martin, G. Bellon, A. Voltaire, D. J. L. Olivié and S. Tytéca (2013).
1563 "Transient Climate Response in a Two-Layer Energy-Balance Model. Part II: Representation
1564 of the Efficacy of Deep-Ocean Heat Uptake and Validation for CMIP5 AOGCMs." Journal
1565 of Climate **26**(6): 1859-1876 DOI: <https://doi.org/10.1175/JCLI-D-12-00196.1>.
- 1566 Geoffroy, O., D. Saint-Martin, D. J. L. Olivié, A. Voltaire, G. Bellon and S. Tytéca (2013).
1567 "Transient Climate Response in a Two-Layer Energy-Balance Model. Part I: Analytical
1568 Solution and Parameter Calibration Using CMIP5 AOGCM Experiments." Journal of Climate
1569 **26**(6): 1841-1857 DOI: <https://doi.org/10.1175/JCLI-D-12-00195.1>.
- 1570 Gerlach, T. (2011). "Volcanic versus anthropogenic carbon dioxide." Eos, Transactions,
1571 American Geophysical Union **92**(24): 201-202 DOI: 10.1029/2011EO240001.
- 1572 Gettelman, A., C. Hannay, J. T. Bacmeister, R. B. Neale, A. G. Pendergrass, G. Danabasoglu,
1573 J. F. Lamarque, J. T. Fasullo, D. A. Bailey, D. M. Lawrence and M. J. Mills (2019). "High
1574 Climate Sensitivity in the Community Earth System Model Version 2 (CESM2)."
1575 Geophysical Research Letters **46**(14): 8329-8337 DOI:
1576 <https://doi.org/10.1029/2019GL083978>.
- 1577 Gregory, J. M. (2000). "Vertical heat transports in the ocean and their effect on time-
1578 dependent climate change." Climate Dynamics **16**(7): 501-515 DOI:
1579 10.1007/s003820000059.
- 1580 Gregory, J. M. and T. Andrews (2016). "Variation in climate sensitivity and feedback
1581 parameters during the historical period." Geophysical Research Letters **43**(8): 3911-3920
1582 DOI: <https://doi.org/10.1002/2016GL068406>.
- 1583 Grewal, M. S. and A. P. Andrews (2001). Kalman Filtering: Theory and Practice Using
1584 MATLAB, Wiley.
- 1585 Gulev, S. K., P. W. Thorne, J. Ahn, F. J. Dentener, C. M. Domingues, S. Gerland, D. Gong,
1586 D. S. Kaufman, H. C. Nnamchi, J. Quaas, J. A. Rivera, S. Sathyendranath, S. L. Smith, B.
1587 Trewin, K. von Schuckmann and R. S. Vose (2021). Changing State of the Climate System.
1588 Climate Change 2021: The Physical Science Basis. Contribution of Working Group I to the
1589 Sixth Assessment Report of the Intergovernmental Panel on Climate Change. V. Masson-
1590 Delmotte, P. Zhai, A. Pirani et al. Cambridge, United Kingdom and New York, NY, USA,
1591 Cambridge University Press: 287–422 DOI: 10.1017/9781009157896.004.
- 1592 Guttman, N. B. (1989). "Statistical Descriptors of Climate." Bulletin of the American
1593 Meteorological Society **70**(6): 602-607 DOI: 10.1175/1520-
1594 0477(1989)070<0602:SDOC>2.0.CO;2.
- 1595 Hakim, G. J., J. Emile-Geay, E. J. Steig, D. Noone, D. M. Anderson, R. Tardif, N. Steiger
1596 and W. A. Perkins (2016). "The last millennium climate reanalysis project: Framework and
1597 first results." Journal of Geophysical Research: Atmospheres **121**(12): 6745-6764 DOI:
1598 <https://doi.org/10.1002/2016JD024751>.
- 1599 Hall, G. and B. Fox-Kemper (2023). "Regional mixed layer depth as a climate diagnostic and
1600 emergent constraint." Geophysical Research Letters [**Preprint, personal communication**].
- 1601 Harshvardhan and M. D. King (1993). "Comparative Accuracy of Diffuse Radiative
1602 Properties Computed Using Selected Multiple Scattering Approximations." Journal of the

This manuscript has been submitted for publication to JOURNAL OF CLIMATE (AMS). Please note that this manuscript has undergone two rounds of peer review but has yet to be formally accepted for publication. Subsequent versions of this manuscript may differ slightly in content.

- 1603 Atmospheric Sciences **50**(2): 247-259 DOI: 10.1175/1520-
1604 0469(1993)050<0247:caodrp>2.0.co;2.
- 1605 Hasselmann, K. (1997). "Multi-pattern fingerprint method for detection and attribution of
1606 climate change." Climate Dynamics **13**(9): 601-611 DOI: 10.1007/s003820050185.
- 1607 Hausfather, Z. (2024). "When will the world really pass 1.5C?"
1608 <https://twitter.com/hausfath/status/1757916875806392657?s=20>.
- 1609 Haustein, K., M. R. Allen, P. M. Forster, F. E. L. Otto, D. M. Mitchell, H. D. Matthews and
1610 D. J. Frame (2017). "A real-time Global Warming Index." Scientific Reports **7**(1): 15417
1611 DOI: 10.1038/s41598-017-14828-5.
- 1612 Hawkins, E. and R. Sutton (2009). "The Potential to Narrow Uncertainty in Regional Climate
1613 Predictions." Bulletin of the American Meteorological Society **90**(8): 1095-1108 DOI:
1614 <https://doi.org/10.1175/2009BAMS2607.1>.
- 1615 Held, I. M., M. Winton, K. Takahashi, T. Delworth, F. Zeng and G. K. Vallis (2010).
1616 "Probing the Fast and Slow Components of Global Warming by Returning Abruptly to
1617 Preindustrial Forcing." Journal of Climate **23**(9): 2418-2427 DOI:
1618 <https://doi.org/10.1175/2009JCLI3466.1>.
- 1619 Horvat, C. (2021). "Marginal ice zone fraction benchmarks sea ice and climate model skill."
1620 Nature Communications **12**(1): 2221 DOI: 10.1038/s41467-021-22004-7.
- 1621 Houtekamer, P. L. and H. L. Mitchell (1998). "Data Assimilation Using an Ensemble Kalman
1622 Filter Technique." Monthly Weather Review **126**(3): 796-811 DOI:
1623 [https://doi.org/10.1175/1520-0493\(1998\)126<0796:DAUAEK>2.0.CO;2](https://doi.org/10.1175/1520-0493(1998)126<0796:DAUAEK>2.0.CO;2).
- 1624 Hu, S. and A. V. Fedorov (2017). "The extreme El Niño of 2015-2016 and the end of global
1625 warming hiatus." Geophysical Research Letters **44**(8): 3816-3824 DOI:
1626 10.1002/2017GL072908.
- 1627 Huguenin, M. F., R. M. Holmes and M. H. England (2022). "Drivers and distribution of
1628 global ocean heat uptake over the last half century." Nature Communications **13**(1): 4921
1629 DOI: 10.1038/s41467-022-32540-5.
- 1630 Hummels, R., M. Dengler and B. Bourlès (2013). "Seasonal and regional variability of upper
1631 ocean diapycnal heat flux in the Atlantic cold tongue." Progress in Oceanography **111**: 52-74
1632 DOI: <https://doi.org/10.1016/j.pocean.2012.11.001>.
- 1633 Illing, S., C. Kadow, H. Pohlmann and C. Timmreck (2018). "Assessing the impact of
1634 a future volcanic eruption on decadal predictions." Earth Syst. Dynam. **9**(2): 701-715 DOI:
1635 10.5194/esd-9-701-2018.
- 1636 Ishii, M., Y. Fukuda, S. Hirahara, S. Yasui, T. Suzuki and K. Sato (2017). "Accuracy of
1637 Global Upper Ocean Heat Content Estimation Expected from Present Observational Data
1638 Sets." SOLA **13**: 163-167 DOI: 10.2151/sola.2017-030.
- 1639 Jones, C. D., J. E. Hickman, S. T. Rumbold, J. Walton, R. D. Lamboll, R. B. Skeie, S.
1640 Fiedler, P. M. Forster, J. Rogelj, M. Abe, M. Botzet, K. Calvin, C. Cassou, J. N. S. Cole, P.
1641 Davini, M. Deushi, M. Dix, J. C. Fyfe, N. P. Gillett, T. Ilyina, M. Kawamiya, M. Kelley, S.
1642 Kharin, T. Koshiro, H. Li, C. Mackallah, W. A. Müller, P. Nabat, T. van Noije, P. Nolan, R.
1643 Ohgaito, D. Olivie, N. Oshima, J. Parodi, T. J. Reerink, L. Ren, A. Romanou, R. Séférian, Y.
1644 Tang, C. Timmreck, J. Tjiputra, E. Tourigny, K. Tsigaridis, H. Wang, M. Wu, K. Wyser, S.
1645 Yang, Y. Yang and T. Ziehn (2021). "The Climate Response to Emissions Reductions Due to

This manuscript has been submitted for publication to JOURNAL OF CLIMATE (AMS). Please note that this manuscript has undergone two rounds of peer review but has yet to be formally accepted for publication. Subsequent versions of this manuscript may differ slightly in content.

- 1646 COVID-19: Initial Results From CovidMIP." Geophysical Research Letters **48**(8):
1647 e2020GL091883 DOI: <https://doi.org/10.1029/2020GL091883>.
- 1648 Jones, P. D. and C. Harpham (2013). "Estimation of the absolute surface air temperature of
1649 the Earth." Journal of Geophysical Research: Atmospheres **118**(8): 3213-3217 DOI:
1650 <https://doi.org/10.1002/jgrd.50359>.
- 1651 Jones, P. D. and P. M. Kelly (1996). The Effect of Tropical Explosive Volcanic Eruptions on
1652 Surface Air Temperature. The Mount Pinatubo Eruption, Berlin, Heidelberg, Springer Berlin
1653 Heidelberg.
- 1654 Julier, S. J. and J. K. Uhlmann (1997). New extension of the Kalman filter to nonlinear
1655 systems. Proc.SPIE DOI: 10.1117/12.280797.
- 1656 Kalman, R. E. (1960). "A New Approach to Linear Filtering and Prediction Problems."
1657 Journal of Basic Engineering **82**(1): 35-45 DOI: 10.1115/1.3662552.
- 1658 Kalman, R. E. and R. S. Bucy (1961). "New Results in Linear Filtering and Prediction
1659 Theory." Journal of Basic Engineering **83**(1): 95-108 DOI: 10.1115/1.3658902.
- 1660 Kalnay, E. (2002). Atmospheric Modeling, Data Assimilation and Predictability. Cambridge,
1661 Cambridge University Press DOI: DOI: 10.1017/CBO9780511802270.
- 1662 Kaufman, D., N. McKay, C. Routson, M. Erb, B. Davis, O. Heiri, S. Jaccard, J. Tierney, C.
1663 Dätwyler, Y. Axford, T. Brussel, O. Cartapanis, B. Chase, A. Dawson, A. De Vernal, S.
1664 Engels, L. Jonkers, J. Marsicek, P. Moffa-Sánchez, C. Morrill, A. Orsi, K. Rehfeld, K.
1665 Saunders, P. S. Sommer, E. Thomas, M. Tonello, M. Tóth, R. Vachula, A. Andreev, S.
1666 Bertrand, B. Biskaborn, M. Bringué, S. Brooks, M. Caniupán, M. Chevalier, L. Cwynar, J.
1667 Emile-Geay, J. Fegyveresi, A. Feurdean, W. Finsinger, M.-C. Fortin, L. Foster, M. Fox, K.
1668 Gajewski, M. Grosjean, S. Hausmann, M. Heinrichs, N. Holmes, B. Ilyashuk, E. Ilyashuk, S.
1669 Juggins, D. Khider, K. Koinig, P. Langdon, I. Larocque-Tobler, J. Li, A. Lotter, T. Luoto, A.
1670 Mackay, E. Magyari, S. Malevich, B. Mark, J. Massaferrero, V. Montade, L. Nazarova, E.
1671 Novenko, P. Pařil, E. Pearson, M. Peros, R. Pienitz, M. Płóciennik, D. Porinchu, A. Potito, A.
1672 Rees, S. Reinemann, S. Roberts, N. Rolland, S. Salonen, A. Self, H. Seppä, S. Shala, J.-M.
1673 St-Jacques, B. Stenni, L. Syrykh, P. Tarrats, K. Taylor, V. Van Den Bos, G. Velle, E. Wahl,
1674 I. Walker, J. Wilmshurst, E. Zhang and S. Zhilich (2020). "A global database of Holocene
1675 paleotemperature records." Scientific Data **7**(1) DOI: 10.1038/s41597-020-0445-3.
- 1676 Keil, P., H. Schmidt, B. Stevens and J. Bao (2021). "Variations of Tropical Lapse Rates in
1677 Climate Models and Their Implications for Upper-Tropospheric Warming." Journal of
1678 Climate **34**(24): 9747-9761 DOI: <https://doi.org/10.1175/JCLI-D-21-0196.1>.
- 1679 Kirtman, B., S. B. Power, A. J. Adedoyin, G. J. Boer, R. Bojariu, I. Camilloni, F. Doblas-
1680 Reyes, A. M. Fiore, M. Kimoto, G. Meehl, M. Prather, A. Sarr, C. Schär, R. Sutton, G. J. van
1681 Oldenborgh, G. Vecchi and H. J. Wang (2013). Near-term climate change. Projections and
1682 predictability, Cambridge University Press. **9781107057999**: 953-1028 DOI:
1683 10.1017/CBO9781107415324.023.
- 1684 Kravitz, B., D. G. MacMartin, H. Wang and P. J. Rasch (2016). "Geoengineering as a design
1685 problem." Earth System Dynamics **7**(2): 469-497 DOI: 10.5194/esd-7-469-2016.
- 1686 Kravitz, B., P. J. Rasch, H. Wang, A. Robock, C. Gabriel, O. Boucher, J. N. S. Cole, J.
1687 Haywood, D. Ji, A. Jones, A. Lenton, J. C. Moore, H. Muri, U. Niemeier, S. Phipps, H.
1688 Schmidt, S. Watanabe, S. Yang and J. H. Yoon (2018). "The climate effects of increasing
1689 ocean albedo: an idealized representation of solar geoengineering." Atmos. Chem. Phys.
1690 **18**(17): 13097-13113 DOI: 10.5194/acp-18-13097-2018.

This manuscript has been submitted for publication to JOURNAL OF CLIMATE (AMS). Please note that this manuscript has undergone two rounds of peer review but has yet to be formally accepted for publication. Subsequent versions of this manuscript may differ slightly in content.

- 1691 Lacey, T. (1998). "Tutorial: The filter." Computer Vision.
- 1692 Lauritzen, S. L. (1981). "Time Series Analysis in 1880: A Discussion of Contributions Made
1693 by T.N. Thiele." International Statistical Review / Revue Internationale de Statistique **49**(3):
1694 319-331 DOI: 10.2307/1402616.
- 1695 Lauritzen, S. L. and T. N. Thiele (2002). Thiele: Pioneer in Statistics, Oxford University
1696 Press.
- 1697 Lee, J. H. and N. L. Ricker (1994). "Extended Kalman Filter Based Nonlinear Model
1698 Predictive Control." Industrial and Engineering Chemistry Research **33**(6): 1530-1541 DOI:
1699 10.1021/ie00030a013.
- 1700 Lee, J. Y., J. Marotzke, G. Bala, L. Cao, S. Corti, J. P. Dunne, F. Engelbrecht, E. Fischer, J.
1701 C. Fyfe, C. Jones, A. Maycock, J. Mutemi, O. Ndiaye, S. Panickal and T. Zhou (2021).
1702 Future Global Climate: Scenario-Based Projections and Near-Term Information. Climate
1703 Change 2021: The Physical Science Basis. Contribution of Working Group I to the Sixth
1704 Assessment Report of the Intergovernmental Panel on Climate Change. V. Masson-Delmotte,
1705 P. Zhai, A. Pirani et al. Cambridge, United Kingdom and New York, NY, USA, Cambridge
1706 University Press: 553–672 DOI: 10.1017/9781009157896.006.
- 1707 Lehner, F., C. Deser, N. Maher, J. Marotzke, E. M. Fischer, L. Brunner, R. Knutti and E.
1708 Hawkins (2020). "Partitioning climate projection uncertainty with multiple large ensembles
1709 and CMIP5/6." Earth Syst. Dynam. **11**(2): 491-508 DOI: 10.5194/esd-11-491-2020.
- 1710 Lenssen, N. J. L., G. A. Schmidt, J. E. Hansen, M. J. Menne, A. Persin, R. Ruedy and D.
1711 Zyss (2019). "Improvements in the GISTEMP Uncertainty Model." Journal of Geophysical
1712 Research: Atmospheres **124**(12): 6307-6326 DOI: <https://doi.org/10.1029/2018JD029522>.
- 1713 Levitus, S., J. I. Antonov, T. P. Boyer, O. K. Baranova, H. E. García, R. A. Locarnini, A. V.
1714 Mishonov, J. R. Reagan, D. Seidov, E. Yarosh and M. M. Zweng (2017). NCEI ocean heat
1715 content, temperature anomalies, salinity anomalies, thermohaline sea level anomalies,
1716 halosteric sea level anomalies, and total steric sea level anomalies from 1955 to present
1717 calculated from in situ oceanographic subsurface profile data. NOAA National Centers for
1718 Environmental Information DOI: <https://doi.org/10.7289/v53f4mvp>.
- 1719 Loeb, N. G., B. A. Wielicki, D. R. Doelling, G. L. Smith, D. F. Keyes, S. Kato, N. Manalo-
1720 Smith and T. Wong (2009). "Toward Optimal Closure of the Earth's Top-of-Atmosphere
1721 Radiation Budget." Journal of Climate **22**(3): 748-766 DOI: 10.1175/2008jcli2637.1.
- 1722 MacMartin, D. G., B. Kravitz and D. W. Keith (2014). Geoengineering: The world's largest
1723 control problem. 2014 American Control Conference, IEEE.
- 1724 Marotzke, J. and P. M. Forster (2015). "Forcing, feedback and internal variability in global
1725 temperature trends." Nature **517**(7536): 565-570 DOI: 10.1038/nature14117.
- 1726 McClelland, H. L. O., I. Halevy, D. A. Wolf-Gladrow, D. Evans and A. S. Bradley (2021).
1727 "Statistical Uncertainty in Paleoclimate Proxy Reconstructions." Geophysical Research
1728 Letters **48**(15): e2021GL092773 DOI: <https://doi.org/10.1029/2021GL092773>.
- 1729 McCormick, M. P., L. W. Thomason and C. R. Trepte (1995). "Atmospheric effects of the Mt
1730 Pinatubo eruption." Nature **373**(6513): 399-404 DOI: 10.1038/373399a0.
- 1731 McCulloch, M. T., A. Winter, C. E. Sherman and J. A. Trotter (2024). "300 years of
1732 sclerosponge thermometry shows global warming has exceeded 1.5 °C." Nature Climate
1733 Change **14**(2): 171-177 DOI: 10.1038/s41558-023-01919-7.

This manuscript has been submitted for publication to JOURNAL OF CLIMATE (AMS). Please note that this manuscript has undergone two rounds of peer review but has yet to be formally accepted for publication. Subsequent versions of this manuscript may differ slightly in content.

- 1734 McDougall, T. J., P. M. Barker, R. M. Holmes, R. Pawlowicz, S. M. Griffies and P. J. Durack
1735 (2021). "The interpretation of temperature and salinity variables in numerical ocean model
1736 output and the calculation of heat fluxes and heat content." Geosci. Model Dev. **14**(10): 6445-
1737 6466 DOI: 10.5194/gmd-14-6445-2021.
- 1738 McKinnon, K. A., A. Poppick, E. Dunn-Sigouin and C. Deser (2017). "An "Observational
1739 Large Ensemble" to Compare Observed and Modeled Temperature Trend Uncertainty due to
1740 Internal Variability." Journal of Climate **30**(19): 7585-7598 DOI:
1741 <https://doi.org/10.1175/JCLI-D-16-0905.1>.
- 1742 Meehl, G. A., R. Moss, K. E. Taylor, V. Eyring, R. J. Stouffer, S. Bony and B. Stevens
1743 (2014). "Climate Model Intercomparisons: Preparing for the Next Phase." Eos, Transactions
1744 American Geophysical Union **95**(9): 77-78 DOI: <https://doi.org/10.1002/2014EO090001>.
- 1745 Meinshausen, M., Z. R. J. Nicholls, J. Lewis, M. J. Gidden, E. Vogel, M. Freund, U. Beyerle,
1746 C. Gessner, A. Nauels, N. Bauer, J. G. Canadell, J. S. Daniel, A. John, P. B. Krummel, G.
1747 Luderer, N. Meinshausen, S. A. Montzka, P. J. Rayner, S. Reimann, S. J. Smith, M. van den
1748 Berg, G. J. M. Velders, M. K. Vollmer and R. H. J. Wang (2020). "The shared socio-
1749 economic pathway (SSP) greenhouse gas concentrations and their extensions to 2500."
1750 Geosci. Model Dev. **13**(8): 3571-3605 DOI: 10.5194/gmd-13-3571-2020.
- 1751 Merchant, C. J., O. Embury, C. E. Bulgin, T. Block, G. K. Corlett, E. Fiedler, S. A. Good, J.
1752 Mittaz, N. A. Rayner, D. Berry, S. Eastwood, M. Taylor, Y. Tsushima, A. Waterfall, R.
1753 Wilson and C. Donlon (2019). "Satellite-based time-series of sea-surface temperature since
1754 1981 for climate applications." Scientific Data **6**(1) DOI: 10.1038/s41597-019-0236-x.
- 1755 Miller, R. L., G. A. Schmidt, L. S. Nazarenko, N. Tausnev, S. E. Bauer, A. D. DelGenio, M.
1756 Kelley, K. K. Lo, R. Ruedy, D. T. Shindell, I. Aleinov, M. Bauer, R. Bleck, V. Canuto, Y.
1757 Chen, Y. Cheng, T. L. Clune, G. Faluvegi, J. E. Hansen, R. J. Healy, N. Y. Kiang, D. Koch,
1758 A. A. Lacis, A. N. LeGrande, J. Lerner, S. Menon, V. Oinas, C. Pérez García-Pando, J. P.
1759 Perlwitz, M. J. Puma, D. Rind, A. Romanou, G. L. Russell, M. Sato, S. Sun, K. Tsigaridis, N.
1760 Unger, A. Voulgarakis, M.-S. Yao and J. Zhang (2014). "CMIP5 historical simulations
1761 (1850–2012) with GISS ModelE2." Journal of Advances in Modeling Earth Systems **6**(2):
1762 441-478 DOI: <https://doi.org/10.1002/2013MS000266>.
- 1763 Miller, R. N. (1996). Introduction to the Kalman filter. Seminar on Data Assimilation, 2-6
1764 September 1996, Shinfield Park, Reading, ECMWF.
- 1765 Montgomery, D. C. and G. C. Runger (2013). Applied Statistics and Probability for
1766 Engineers. New York, NY, John Wiley & Sons.
- 1767 Morice, C. P., J. J. Kennedy, N. A. Rayner, J. P. Winn, E. Hogan, R. E. Killick, R. J. H.
1768 Dunn, T. J. Osborn, P. D. Jones and I. R. Simpson (2021). "An Updated Assessment of Near-
1769 Surface Temperature Change From 1850: The HadCRUT5 Data Set." Journal of Geophysical
1770 Research: Atmospheres **126**(3): e2019JD032361 DOI:
1771 <https://doi.org/10.1029/2019JD032361>.
- 1772 Myers, M. A. and R. H. Luecke (1991). "Process control applications of an extended Kalman
1773 filter algorithm." Computers & Chemical Engineering **15**(12): 853-857 DOI:
1774 [https://doi.org/10.1016/0098-1354\(91\)80030-Y](https://doi.org/10.1016/0098-1354(91)80030-Y).
- 1775 Nasa/Larc/Sd/Asdc (2018). Global Space-based Stratospheric Aerosol Climatology Version
1776 2.0.
- 1777 Nazarenko, L. S., N. Tausnev, G. L. Russell, D. Rind, R. L. Miller, G. A. Schmidt, S. E.
1778 Bauer, M. Kelley, R. Ruedy, A. S. Ackerman, I. Aleinov, M. Bauer, R. Bleck, V. Canuto, G.

This manuscript has been submitted for publication to JOURNAL OF CLIMATE (AMS). Please note that this manuscript has undergone two rounds of peer review but has yet to be formally accepted for publication. Subsequent versions of this manuscript may differ slightly in content.

- 1779 Cesana, Y. Cheng, T. L. Clune, B. I. Cook, C. A. Cruz, A. D. Del Genio, G. S. Elsaesser, G.
1780 Faluvegi, N. Y. Kiang, D. Kim, A. A. Lacis, A. Leboissetier, A. N. LeGrande, K. K. Lo, J.
1781 Marshall, E. E. Matthews, S. McDermid, K. Mezuman, L. T. Murray, V. Oinas, C. Orbe, C.
1782 P. García-Pando, J. P. Perlwitz, M. J. Puma, A. Romanou, D. T. Shindell, S. Sun, K.
1783 Tsigaridis, G. Tselioudis, E. Weng, J. Wu and M.-S. Yao (2022). "Future Climate Change
1784 Under SSP Emission Scenarios With GISS-E2.1." *Journal of Advances in Modeling Earth*
1785 *Systems* **14**(7): e2021MS002871 DOI: <https://doi.org/10.1029/2021MS002871>.
- 1786 Newsom, E., L. Zanna and J. Gregory (2023). "Background Pycnocline Depth Constrains
1787 Future Ocean Heat Uptake Efficiency." *Geophysical Research Letters* **50**(22):
1788 e2023GL105673 DOI: <https://doi.org/10.1029/2023GL105673>.
- 1789 Ogorek, B. (2019) "Yet Another Kalman Filter Explanation Article." *Towards Data Science*.
- 1790 Okada, M., K. Yamanishi and N. Masuda (2020). "Long-tailed distributions of inter-event
1791 times as mixtures of exponential distributions." *Royal Society Open Science* **7**: 191643 DOI:
1792 10.1098/rsos.191643.
- 1793 Otto, F. E. L., D. J. Frame, A. Otto and M. R. Allen (2015). "Embracing uncertainty in
1794 climate change policy." *Nature Climate Change* **5**(10): 917-920 DOI: 10.1038/nclimate2716.
- 1795 Palmer, M., G. Harris and J. Gregory (2018). "Extending CMIP5 projections of global mean
1796 temperature change and sea level rise due to thermal expansion using a physically-based
1797 emulator." *Environmental Research Letters* **13** DOI: 10.1088/1748-9326/aad2e4.
- 1798 Palmer, M., T. Howard, J. Tinker, J. Lowe, L. Bricheno, D. Calvert, T. Edwards, J. Gregory,
1799 G. Harris, J. Krijnen, M. Pickering, C. Roberts and J. Wolf (2018). UKCP18 marine report.
- 1800 Palmer, M. D., C. M. Domingues, A. B. A. Slangen and F. Boeira Dias (2021). "An ensemble
1801 approach to quantify global mean sea-level rise over the 20th century from tide gauge
1802 reconstructions." *Environmental Research Letters* **16**(4): 044043 DOI: 10.1088/1748-
1803 9326/abdaec.
- 1804 Papale, P. (2018). "Global time-size distribution of volcanic eruptions on Earth." *Scientific*
1805 *Reports* **8**(1): 6838 DOI: 10.1038/s41598-018-25286-y.
- 1806 Pielke Jr, R., M. G. Burgess and J. Ritchie (2022). "Plausible 2005–2050 emissions scenarios
1807 project between 2 °C and 3 °C of warming by 2100." *Environmental Research Letters* **17**(2):
1808 024027 DOI: 10.1088/1748-9326/ac4ebf.
- 1809 Quevedo, H. and G. Gonzalez (2017). "Non-normal Distribution of Temperatures in the
1810 United States of America during 1895-2016: A Challenge to the Central Limit Theorem."
1811 *Pinnacle Environmental & Earth Sciences* **4**: 1182.
- 1812 Rauch, H. E., F. Tung and C. T. Striebel (1965). "Maximum likelihood estimates of linear
1813 dynamic systems." *AIAA Journal* **3**(8): 1445-1450 DOI: 10.2514/3.3166.
- 1814 Roach, L. A., J. Dörr, C. R. Holmes, F. Massonnet, E. W. Blockley, D. Notz, T. Rackow, M.
1815 N. Raphael, S. P. O'Farrell, D. A. Bailey and C. M. Bitz (2020). "Antarctic Sea Ice Area in
1816 CMIP6." *Geophysical Research Letters* **47**(9): e2019GL086729 DOI:
1817 <https://doi.org/10.1029/2019GL086729>.
- 1818 Robinson, A. and H. Stommel (1959). "The Oceanic Thermocline and the Associated
1819 Thermohaline Circulation." *Tellus* **11**: 295-308.
- 1820 Rodgers, K. B., S. S. Lee, N. Rosenbloom, A. Timmermann, G. Danabasoglu, C. Deser, J.
1821 Edwards, J. E. Kim, I. R. Simpson, K. Stein, M. F. Stuecker, R. Yamaguchi, T. Bódai, E. S.
1822 Chung, L. Huang, W. M. Kim, J. F. Lamarque, D. L. Lombardozzi, W. R. Wieder and S. G.

This manuscript has been submitted for publication to JOURNAL OF CLIMATE (AMS). Please note that this manuscript has undergone two rounds of peer review but has yet to be formally accepted for publication. Subsequent versions of this manuscript may differ slightly in content.

- 1823 Yeager (2021). "Ubiquity of human-induced changes in climate variability." *Earth Syst.*
1824 *Dynam.* **12**(4): 1393-1411 DOI: 10.5194/esd-12-1393-2021.
- 1825 Rosenblum, E. and I. Eisenman (2017). "Sea Ice Trends in Climate Models Only Accurate in
1826 Runs with Biased Global Warming." *Journal of Climate* **30**(16): 6265-6278 DOI:
1827 <https://doi.org/10.1175/JCLI-D-16-0455.1>.
- 1828 Sætrom, J. and H. Omre (2013). "Uncertainty Quantification in the Ensemble Kalman Filter."
1829 *Scandinavian Journal of Statistics* **40**(4): 868-885 DOI: 10.1111/sjos.12039.
- 1830 Särkkä, S. (2013). *Bayesian Filtering and Smoothing*, Cambridge University Press.
- 1831 Sato, M., J. E. Hansen, M. P. McCormick and J. B. Pollack (1993). "Stratospheric aerosol
1832 optical depths, 1850-1990." *J. Geophys. Res.* **98**: 22987-22994 DOI: 10.1029/93JD02553.
- 1833 Schmidt, S. F. (1981). "The Kalman filter - Its recognition and development for aerospace
1834 applications." *Journal of Guidance and Control* **4**(1): 4-7 DOI: 10.2514/3.19713.
- 1835 Schwartz, S. E. (2007). "Heat capacity, time constant, and sensitivity of Earth's climate
1836 system." *Journal of Geophysical Research* **112**(D24): D24S05-D24S05 DOI:
1837 10.1029/2007JD008746.
- 1838 Sellers, W. D. (1969). "A Global Climatic Model Based on the Energy Balance of the Earth-
1839 Atmosphere System." *Journal of Applied Meteorology (1962-1982)* **8**(3): 392-400.
- 1840 Sherwood, S. C., M. J. Webb, J. D. Annan, K. C. Armour, P. M. Forster, J. C. Hargreaves, G.
1841 Hegerl, S. A. Klein, K. D. Marvel, E. J. Rohling, M. Watanabe, T. Andrews, P. Braconnot, C.
1842 S. Bretherton, G. L. Foster, Z. Hausfather, A. S. von der Heydt, R. Knutti, T. Mauritsen, J. R.
1843 Norris, C. Proistosescu, M. Rugenstein, G. A. Schmidt, K. B. Tokarska and M. D. Zelinka
1844 (2020). "An Assessment of Earth's Climate Sensitivity Using Multiple Lines of Evidence."
1845 *Reviews of Geophysics* **58**(4): e2019RG000678 DOI:
1846 <https://doi.org/10.1029/2019RG000678>.
- 1847 Smith, C. J., P. M. Forster, S. Berger, W. Collins, B. Hall, D. Lunt, M. D. Palmer, M.
1848 Watanabe, M. Cain, G. Harris, N. J. Leach, M. Ringer and M. Zelinka (2021). Figure and
1849 data generation for Chapter 7 of the IPCC's Sixth Assessment Report, Working Group 1 (plus
1850 assorted other contributions). I. P. o. C. Change DOI:
1851 <https://doi.org/10.5281/zenodo.5211357>.
- 1852 Smith, S. W. (2003). Chapter 15 - Moving Average Filters. *Digital Signal Processing*. S. W.
1853 Smith. Boston, Newnes: 277-284 DOI: [https://doi.org/10.1016/B978-0-7506-7444-7/50052-](https://doi.org/10.1016/B978-0-7506-7444-7/50052-2)
1854 [2](https://doi.org/10.1016/B978-0-7506-7444-7/50052-2).
- 1855 Soden, B. J., R. T. Wetherald, G. L. Stenchikov and A. Robock (2002). "Global Cooling
1856 After the Eruption of Mount Pinatubo: A Test of Climate Feedback by Water Vapor."
1857 *Science* **296**(5568): 727-730 DOI: doi:10.1126/science.296.5568.727.
- 1858 Stratonovich, R. L. (1959). "Optimum nonlinear systems which bring about a separation of a
1859 signal with constant parameters from noise." *Radiofizika* **2**(6): 892-901.
- 1860 Stratonovich, R. L. (1960). "Application of the Markov processes theory to optimal filtering."
1861 *Radio Engineering and Electronic Physics* **5**(11): 1-19.
- 1862 Susskind, J., G. A. Schmidt, J. N. Lee and L. Iredell (2019). "Recent global warming as
1863 confirmed by AIRS." *Environmental Research Letters* **14**(4): 044030 DOI: 10.1088/1748-
1864 9326/aafd4e.
- 1865 Swerling, P. (1959). *First-Order Error Propagation in a Stagewise Smoothing Procedure for*
1866 *Satellite Observations*. Santa Monica, CA, RAND Corporation.

This manuscript has been submitted for publication to JOURNAL OF CLIMATE (AMS). Please note that this manuscript has undergone two rounds of peer review but has yet to be formally accepted for publication. Subsequent versions of this manuscript may differ slightly in content.

- 1867 Tebaldi, C., K. Debeire, V. Eyring, E. Fischer, J. Fyfe, P. Friedlingstein, R. Knutti, J. Lowe,
1868 B. O'Neill, B. Sanderson, D. van Vuuren, K. Riahi, M. Meinshausen, Z. Nicholls, K. B.
1869 Tokarska, G. Hurtt, E. Kriegler, J. F. Lamarque, G. Meehl, R. Moss, S. E. Bauer, O. Boucher,
1870 V. Brovkin, Y. H. Byun, M. Dix, S. Gualdi, H. Guo, J. G. John, S. Kharin, Y. Kim, T.
1871 Koshiro, L. Ma, D. Olivie, S. Panickal, F. Qiao, X. Rong, N. Rosenbloom, M. Schupfner, R.
1872 Séférian, A. Sellar, T. Semmler, X. Shi, Z. Song, C. Steger, R. Stouffer, N. Swart, K.
1873 Tachiiri, Q. Tang, H. Tatebe, A. Voldoire, E. Volodin, K. Wyser, X. Xin, S. Yang, Y. Yu and
1874 T. Ziehn (2021). "Climate model projections from the Scenario Model Intercomparison
1875 Project (ScenarioMIP) of CMIP6." Earth Syst. Dynam. **12**(1): 253-293 DOI: 10.5194/esd-12-
1876 253-2021.
- 1877 Tebaldi, C. and R. Knutti (2018). "Evaluating the accuracy of climate change pattern
1878 emulation for low warming targets." Environmental Research Letters **13** DOI: 10.1088/1748-
1879 9326/aabef2.
- 1880 Timmreck, C., G. W. Mann, V. Aquila, R. Hommel, L. A. Lee, A. Schmidt, C. Brühl, S.
1881 Carn, M. Chin, S. S. Dhomse, T. Diehl, J. M. English, M. J. Mills, R. Neely, J. Sheng, M.
1882 Toohey and D. Weisenstein (2018). "The Interactive Stratospheric Aerosol Model
1883 Intercomparison Project (ISA-MIP): motivation and experimental design." Geosci. Model
1884 Dev. **11**(7): 2581-2608 DOI: 10.5194/gmd-11-2581-2018.
- 1885 van Katwyk, P., B. Fox-Kemper, H. Seroussi, S. Nowicki and K. J. Bergen (2023). "A
1886 variational LSTM emulator of sea level contribution from the Antarctic ice sheet." Journal of
1887 Advances in Modeling Earth Systems Submitted.
- 1888 van Vuuren, D. P., M. G. J. den Elzen, P. L. Lucas, B. Eickhout, B. J. Strengers, B. van
1889 Ruijven, S. Wonink and R. van Houdt (2007). "Stabilizing greenhouse gas concentrations at
1890 low levels: an assessment of reduction strategies and costs." Climatic Change **81**(2): 119-159
1891 DOI: 10.1007/s10584-006-9172-9.
- 1892 van Vuuren, D. P., E. Stehfest, D. E. H. J. Gernaat, J. C. Doelman, M. van den Berg, M.
1893 Harmsen, H. S. de Boer, L. F. Bouwman, V. Daioglou, O. Y. Edelenbosch, B. Girod, T.
1894 Kram, L. Lassaletta, P. L. Lucas, H. van Meijl, C. Müller, B. J. van Ruijven, S. van der Sluis
1895 and A. Tabeau (2017). "Energy, land-use and greenhouse gas emissions trajectories under a
1896 green growth paradigm." Global Environmental Change **42**: 237-250 DOI:
1897 <https://doi.org/10.1016/j.gloenvcha.2016.05.008>.
- 1898 Vernier, J., L. Thomason, J. P. Pommereau, A. Bourassa, J. Pelon, A. Garnier, A.
1899 Hauchecorne, L. Blantot, C. Trepte, D. Degenstein and F. Vargas (2011). "Major influence of
1900 tropical volcanic eruptions on the stratospheric aerosol layer during the last decade."
1901 GEOPHYSICAL RESEARCH LETTERS **38** DOI: 10.1029/2011GL047563.
- 1902 Wan, E. A. and R. Van Der Merwe (2000). The unscented Kalman filter for nonlinear
1903 estimation, Institute of Electrical and Electronics Engineers Inc. DOI:
1904 10.1109/ASSPCC.2000.882463.
- 1905 Wielicki, B. A., B. R. Barkstrom, E. F. Harrison, R. B. Lee, G. Louis Smith and J. E. Cooper
1906 (1996). "Clouds and the Earth's Radiant Energy System (CERES): An Earth Observing
1907 System Experiment." Bulletin of the American Meteorological Society **77**(5): 853-868 DOI:
1908 10.1175/1520-0477(1996)077<0853:catere>2.0.co;2.
- 1909 Wild, M., D. Folini, M. Z. Hakuba, C. Schär, S. I. Seneviratne, S. Kato, D. Rutan, C.
1910 Ammann, E. F. Wood and G. König-Langlo (2015). "The energy balance over land and
1911 oceans: an assessment based on direct observations and CMIP5 climate models." Climate
1912 Dynamics **44**(11): 3393-3429 DOI: 10.1007/s00382-014-2430-z.

This manuscript has been submitted for publication to JOURNAL OF CLIMATE (AMS). Please note that this manuscript has undergone two rounds of peer review but has yet to be formally accepted for publication. Subsequent versions of this manuscript may differ slightly in content.

- 1913 Wild, M., M. Z. Hakuba, D. Folini, P. Dörig-Ott, C. Schär, S. Kato and C. N. Long (2019).
1914 "The cloud-free global energy balance and inferred cloud radiative effects: an assessment
1915 based on direct observations and climate models." Climate Dynamics **52**(7): 4787-4812 DOI:
1916 10.1007/s00382-018-4413-y.
- 1917 Willner, D., C.-B. Chang and K.-P. Dunn (1977). Kalman filter algorithms for a multi-sensor
1918 system DOI: 10.1109/CDC.1976.267794.
- 1919 Winton, M., K. Takahashi and I. M. Held (2010). "Importance of Ocean Heat Uptake
1920 Efficacy to Transient Climate Change." Journal of Climate **23**(9): 2333-2344 DOI:
1921 <https://doi.org/10.1175/2009JCLI3139.1>.
- 1922 Wunsch, C. (2020). "Is the Ocean Speeding Up? Ocean Surface Energy Trends." Journal of
1923 Physical Oceanography **50**(11): 3205-3217 DOI: 10.1175/jpo-d-20-0082.1.
- 1924 Wunsch, C. and P. Heimbach (2007). "Practical global oceanic state estimation." Physica D:
1925 Nonlinear Phenomena **230**(1): 197-208 DOI: <https://doi.org/10.1016/j.physd.2006.09.040>.
- 1926 Yang, S., Z. Li, J.-Y. Yu, X. Hu, W. Dong and S. He (2018). "El Niño–Southern Oscillation
1927 and its impact in the changing climate." National Science Review **5**(6): 840-857 DOI:
1928 10.1093/nsr/nwy046.
- 1929 Youngjoo, K. and B. Hyochoong (2018). Introduction to Kalman Filter and Its Applications.
1930 Introduction and Implementations of the Kalman Filter. G. Felix. Rijeka, IntechOpen DOI:
1931 10.5772/intechopen.80600.
- 1932 Zanchettin, D., M. Khodri, C. Timmreck, M. Toohey, A. Schmidt, E. P. Gerber, G. Hegerl,
1933 A. Robock, F. S. R. Pausata, W. T. Ball, S. E. Bauer, S. Bekki, S. S. Dhomse, A. N.
1934 LeGrande, G. W. Mann, L. Marshall, M. Mills, M. Marchand, U. Niemeier, V. Poulain, E.
1935 Rozanov, A. Rubino, A. Stenke, K. Tsigaridis and F. Tummon (2016). "The Model
1936 Intercomparison Project on the climatic response to Volcanic forcing (VolMIP): experimental
1937 design and forcing input data for CMIP6." Geosci. Model Dev. **9**(8): 2701-2719 DOI:
1938 10.5194/gmd-9-2701-2016.
- 1939 Zanna, L., S. Khatiwala, J. M. Gregory, J. Ison and P. Heimbach (2019). "Global
1940 reconstruction of historical ocean heat storage and transport." Proceedings of the National
1941 Academy of Sciences **116**(4): 1126-1131 DOI: 10.1073/pnas.1808838115.
- 1942 Zelinka, M. D., D. A. Randall, M. J. Webb and S. A. Klein (2017). "Clearing clouds of
1943 uncertainty." Nature Climate Change **7**(10): 674-678 DOI: 10.1038/nclimate3402.
- 1944 Zhang, A. and M. Atia (2020). "An Efficient Tuning Framework for Kalman Filter Parameter
1945 Optimization using Design of Experiments and Genetic Algorithms." Navigation - Journal of
1946 The Institute of Navigation **In press** DOI: 10.1002/navi.399.
- 1947 Zhu, J., B. L. Otto-Bliesner, E. C. Brady, A. Gettelman, J. T. Bacmeister, R. B. Neale, C. J.
1948 Poulsen, J. K. Shaw, Z. S. McGraw and J. E. Kay (2022). "LGM Paleoclimate Constraints
1949 Inform Cloud Parameterizations and Equilibrium Climate Sensitivity in CESM2." Journal of
1950 Advances in Modeling Earth Systems **14**(4): e2021MS002776 DOI:
1951 <https://doi.org/10.1029/2021MS002776>.
- 1952

1
2
3
4
5
6
7
8
9
10
11
12
13
14
15
16
17
18
19

SUPPLEMENT TO

Efficient Estimation of Climate State and Its Uncertainty Using Kalman Filtering with Application to Policy Thresholds and Volcanism

J. Matthew Nicklas,^a Baylor Fox-Kemper,^a Charles Lawrence.^a

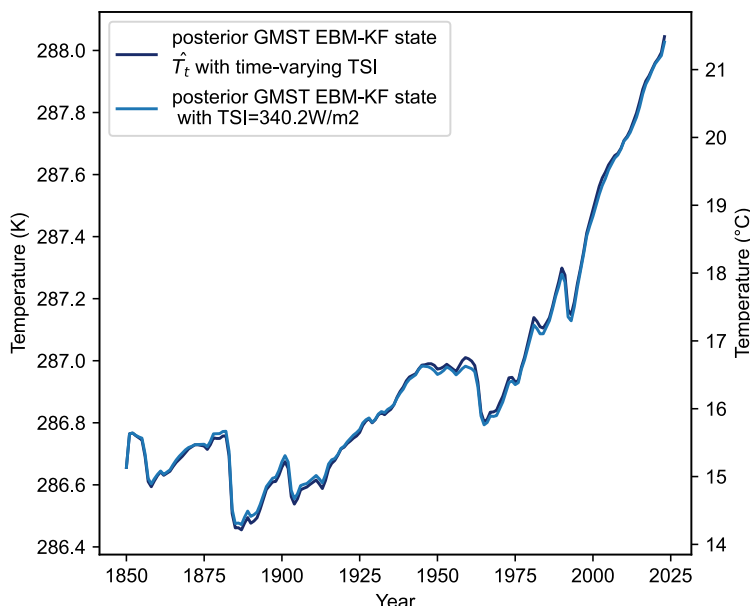
^a Brown University, Providence, Rhode Island.

Corresponding author: J. Matthew Nicklas, john_nicklas@brown.edu

Section A: Derivation of EBM-KF

A1: Individual Functional Parts and Derivation

$\left(\frac{G_{SC}}{4}\right)_t$ is the total solar irradiance (TSI) normalized to the Earth's surface area at ~ 1360 $W/m^2 / 4 = 340.2 W/m^2$. Estimates of this normalized total solar irradiance indicate that it has varied since 1850 between $340.06 W/m^2$ and $340.49 W/m^2$ according to the Naval Research Laboratory 2 solar irradiance model ([NRLTSI2_v02r01](#) (Coddington, Lean et al. 2017)). Within the hindcast EBM-KF model these NRL2 estimates were used, but this had a negligible effect on the model results compared to a constant $\overline{\frac{G_{SC}}{4}} = 340.2 W/m^2$ value.



Supp. Fig. 1: Comparisons of the used EBM-Kalman Filtered climate state with time-varying total solar irradiance (navy blue) with an EBM-Kalman Filtered climate state with constant solar irradiance (light blue) set at $340.2 W/m^2$. These differed by at most $0.028^\circ C$ in 1960.

This manuscript has been submitted for publication to JOURNAL OF CLIMATE (AMS). Please note that this manuscript has undergone two rounds of peer review but has yet to be formally accepted for publication. Subsequent versions of this manuscript may differ slightly in content.

20 $\tilde{d}(t)$ is the prescribed shortwave radiation attenuation due to volcanic dust, the direct
 21 radiative effect of anthropogenic aerosols, and non-cloud atmospheric effects. This
 22 stochastically varying quantity can be calculated from the (unitless) stratospheric optical
 23 depth AOD_n (Sato, Hansen et al. 1993; Vernier, Thomason et al. 2011), according to the
 24 formula given by Harshvardan and King (1993; Schwartz, Harshvardhan et al. 2002).
 25 ($g=0.853$ is the middle of the given range). The AOD_t values used are forcings for the GISS
 26 climate model from 1850 – 1978
 27 (https://data.giss.nasa.gov/modelforce/strataer/tau.line_2012.12.txt, AOD_n at 550nm) and
 28 globally averaged measurements from the GloSSAC_V2.21 satellite measurement product
 29 (Nasa/Larc/Sd/Asdc 2018) from 1979 – 2022
 30 (https://asdc.larc.nasa.gov/project/GloSSAC/GloSSAC_2.21, AOD_t at 525nm). These
 31 wavelengths are at the shorter end of the 0.25-4 μm range of incoming solar shortwave
 32 energy \mathcal{F}_{SW} , allowing satellites to detect dust reflectance. As the CALIPSO satellite mission
 33 ended in 2023, the year 2023 was extrapolated from a linear trend of the AOD_t values from
 34 2025-2022.

$$35 \quad \tilde{d}(t) = \frac{4/3}{AOD_t^{*(1-g)+2q'}}, \quad g \in [0.834 - 0.872], \quad q' = 0.715 \quad (\text{SA1})$$

$$36 \quad \tilde{d}(t) \approx \frac{9.07}{AOD_t + 9.73} \quad (\text{SA2})$$

37 Utilizing the equation above to calculate the dry-atmosphere reflected energy during a
 38 relatively aerosol-free period (2000-2005), when the aerosol optical depth was about 0.002m:

$$39 \quad \mathcal{F}_{SW_{clearsky}}^{refl\ by\ dryatm} = \frac{\overline{G_{SC}}}{4} * (1 - \tilde{d}(2002)) = 340.2 \frac{W}{m^2} \left(1 - \frac{9.07}{0.002+9.73}\right) = 23.1 \frac{W}{m^2} \quad (\text{SA3})$$

40 This value agrees with the clear-sky reflected energy (53 [52-55] W/m^2) minus reflected
 41 surface energy (33 [31-34] W/m^2), of 20 [18-24] W/m^2 reported by Wild, Hakuba et. al.
 42 (2019). Furthermore, the measured and inferred aerosol optical depth measurements already
 43 include those contributions from the anthropogenic sources.

44 $f_{\alpha A}(T_n, t)$ is the additional atmospheric shortwave attenuation due to cloud albedo, while
 45 $f_{\alpha S}(T_n)$ is the surface shortwave attenuation due to ground albedo. A portion of this varying
 46 cloud albedo is direct thermal feedback, whereas another portion is due to cloud seeding by
 47 anthropogenic aerosols AC_t . To contain the EBM model's complexity, the changing ground
 48 albedo is assumed to be only thermal feedback: the shortwave aspect of land use changes are
 49 neglected. Taken together, these two terms and \tilde{d}_n yield an overall absorption of 0.707 as

This manuscript has been submitted for publication to JOURNAL OF CLIMATE (AMS). Please note that this manuscript has undergone two rounds of peer review but has yet to be formally accepted for publication. Subsequent versions of this manuscript may differ slightly in content.

50 measured from March 2000 to February 2005 by the CERES satellite (Wielicki, Barkstrom et
 51 al. 1996; Loeb, Wielicki et al. 2009), or equivalently a top-of-atmosphere, all-sky albedo of
 52 0.293. Decomposition of this overall albedo into its clear-sky component (0.153) yields a
 53 ground * dry atmosphere absorption fraction of 0.847.

$$54 \quad 0.847 = \overline{d}_{2002} * f_{\alpha_S}(T_{2002}) = 0.932 * f_{\alpha_S}(T_{2002}), \quad \text{thus} \quad f_{\alpha_S}(T_{2002})=0.909 \quad (\text{SA4})$$

$$55 \quad 0.707 = \overline{d}_{2002} * f_{\alpha_A}(T_{2002}, 2002) * f_{\alpha_S}(T_{2002}) = 0.847 * f_{\alpha_A}(T_{2002}, 2002),$$

$$56 \quad \text{thus,} \quad f_{\alpha_A}(T_{2002}, 2002)=0.834 \quad (\text{SA5})$$

57 Verifying the reflected energies:

$$58 \quad \mathcal{F}_{\text{SW clearsky}}^{\text{refl by gnd}} = \frac{\overline{G_{\text{SC}}}}{4} * \tilde{d}(2002) * (1 - f_{\alpha_S}(T_{2002}))$$

$$59 \quad = 340.2 \frac{\text{W}}{\text{m}^2} * 0.932 * 0.091 = 28.8 \frac{\text{W}}{\text{m}^2} \quad (\text{SA6})$$

$$60 \quad \mathcal{F}_{\text{SW allsky}}^{\text{refl by gnd}} = \frac{\overline{G_{\text{SC}}}}{4} * \tilde{d}(2002) * f_{\alpha_A}(T_{2002}, 2002) * (1 - f_{\alpha_S}(T_{2002})) = 24.1 \frac{\text{W}}{\text{m}^2} \quad (\text{SA7})$$

$$61 \quad \mathcal{F}_{\text{SW allsky}}^{\text{refl by clouds}} = \frac{\overline{G_{\text{SC}}}}{4} * \tilde{d}(2002) * (1 - f_{\alpha_A}(T_{2002}, 2002)) = 52.6 \frac{\text{W}}{\text{m}^2} \quad (\text{SA8})$$

62

63 There is a slight discrepancy in the clear-sky ground-reflected energy relative to the literature
 64 value (33 [31-34] W/m²), but the all-sky reflected energies are much more closely aligned:
 65 the ground reported value is 25 [23-26] W/m², and the dry atmosphere + cloud reported value
 66 is 75 [71-77] W/m², compared to this inferred value of 52.6 + 24.1 = 76.7 W/m² (Wild, Folini
 67 et al. 2015). Note that this shortwave flux equation does not consider shortwave energy
 68 absorbed into the atmosphere, a substantial simplification.

69 $j^*(T_\ell) = \sigma_{\text{sf}} T_\ell^4$ is the ideal black body radiation or Planck feedback, which derives from
 70 quantum mechanics, particularly the Stefan-Boltzmann law (Boltzmann 1884), which gives
 71 the Stefan-Boltzman constant $\sigma_{\text{sf}} = 5.670 \cdot 10^{-8} \text{Wm}^{-2}\text{K}^{-4}$ as a coefficient. For the Earth, because
 72 the temperature is in the neighborhood of 287K, this black body radiation is primarily in the
 73 infrared spectrum, between 200 and 1200 cm⁻¹ (Zhong and Haigh 2013).

74 $\tilde{g}(\mathbf{t})$ is the prescribed longwave attenuation due to CO₂ and other anthropogenic greenhouse
 75 gases (CH₄, NO₂, O₃, halogens), which is half of the fraction of radiative energy absorbed by
 76 those gases (because half is re-emitted upwards and half downwards). This absorbed,

This manuscript has been submitted for publication to JOURNAL OF CLIMATE (AMS). Please note that this manuscript has undergone two rounds of peer review but has yet to be formally accepted for publication. Subsequent versions of this manuscript may differ slightly in content.

77 downwards-emitted fraction increases linearly by a factor of β_0 with respect to the logarithm
 78 of the CO₂ concentration measured in ppm (see Figure 6b of (Zhong and Haigh 2013)). CO₂
 79 concentrations were taken as the historical concentrations used in the NASA GISS climate
 80 model 1850-1979 (<https://data.giss.nasa.gov/modelforce/ghgases/Fig1A.ext.txt>) and the
 81 NOAA global averages from 1980-2021
 82 (https://gml.noaa.gov/webdata/ccgg/trends/co2/co2_annmean_gl.txt).

$$83 \quad \phi_{LW}(\text{out}) = j^*(T_t) - \frac{\phi_{LW}(\text{absorbed})}{2} = j^*(T_t) * \tilde{g}(t) * f_{H_2O}(T_t) \quad (\text{SA9})$$

$$84 \quad \tilde{g}(t) * f_{H_2O}(T_t) = \left(1 - \frac{\phi_{LW}(\text{CO}_2 \text{ absorb})}{2j^*(T_t)}\right) * \left(1 - \frac{\phi_{LW}(\text{H}_2\text{O absorb})}{2j^*(T_t)}\right) \approx \left(1 - \frac{\phi_{LW}(\text{CO}_2 \text{ absorb}) + \phi_{LW}(\text{H}_2\text{O absorb})}{2j^*(T_t)}\right) \quad (\text{SA10})$$

$$85 \quad \tilde{g}(t) = 1 - \beta_0 \log_{10}([\text{eCO}_2]_t) < 1 \quad (\text{SA11})$$

86 Equation SA9 refers to a single-layer atmosphere assumed by prior researchers such as
 87 Kravitz, Rasch, et. al. (2018). While the technically correct separation of SA9 is shown on the
 88 right hand side of SA10, the form for the product of $\tilde{g}(t) * f_{H_2O}(T_t)$ was chosen specifically
 89 to resemble the previous shortwave energy expressions, essentially representing CO₂ in an
 90 atmospheric layer above H₂O (sequential filtering in the middle expression of SA10).
 91 Relating these two representations demands the simplification that both the longwave
 92 radiative fluxes absorbed by CO₂ and H₂O are each smaller than twice the total ground-
 93 emitted longwave radiative flux, so their product is yet smaller and can be neglected. Indeed,
 94 for CO₂ this ratio $\frac{\phi_{LW}(\text{CO}_2 \text{ absorb})}{2j^*(T_t)} = \beta_0 \log_{10}([\text{CO}_2]_t)$ is in the range [0.165 - 0.176] and for
 95 H₂O the analogous ratio is in the range [0.250 - 0.259] so their product (the difference
 96 between the RHS and LHS of A12) is at most 0.045. This difference in energy flux would be
 97 large enough to cause significant inaccuracies in the energy balance model (larger than the
 98 anthropogenic global warming signal), should parameters from a single-layer atmosphere be
 99 used in a sequential filter model. Thus, the critical parameters β_0 and β_1 must be calculated
 100 within the framework of the chosen model (here a sequential filter – see below), after which
 101 this distinction only matters to the higher-order terms of the deviations from the preindustrial
 102 energy flux $(0.176-0.165) * (0.259-0.250) \approx 0.0001$, a negligible fraction.

103 More complex functions for $\tilde{g}(t)$ exist involving functions for each individual
 104 greenhouse gas (Meinshausen, Nicholls et al. 2020) but for the purposes of simplifying this
 105 energy balance model, only one “effective greenhouse” concentration is used. Our “effective

This manuscript has been submitted for publication to JOURNAL OF CLIMATE (AMS). Please note that this manuscript has undergone two rounds of peer review but has yet to be formally accepted for publication. Subsequent versions of this manuscript may differ slightly in content.

106 greenhouse gas concentration” includes CH₄, N₂O, O₃, contrails, stratospheric water vapor,
107 land use, and black carbon on snow but excluding anthropogenic atmospheric aerosols
108 (Forster, Smith et al. 2023). Formally, land use and black carbon on snow should be included
109 as a prescribed change to the $f_{\alpha S}$ function on the shortwave side but in combination these two
110 amount to within -0.15 W/m², less in absolute value than all the other aforementioned
111 “combined greenhouse forcing” components aside from contrails and stratospheric water
112 vapor. Similarly, the prescribed contribution of stratospheric water vapor should formally be
113 within the $f_{H_2O}(T_t)$ function not lumped with the other greenhouse gases, but as this
114 represents only 0.05 W/m² at most, this is inconsequential (variations in incoming solar
115 insolation are of a similar magnitude). We determined the “effective CO₂ concentration” by
116 first fitting a function relating CO₂ concentrations reported above to the CO₂ radiative
117 forcings reported by Forster (2023) at [https://github.com/ClimateIndicator/forcing-](https://github.com/ClimateIndicator/forcing-timeseries/tree/main/output)
118 [timeseries/tree/main/output](https://github.com/ClimateIndicator/forcing-timeseries/tree/main/output).

$$119 \quad \phi_{LW}^{CO_2} = 12.74 \log_{10}([eCO_2]_t) - 31.55 \quad (SA12)$$

120 Then by summing all “effective greenhouse gas” reported energy fluxes, the above function
121 was inverted to determine the “effective CO₂ concentration.” These ranged from 278 ppm (or
122 $\log_{10}([eCO_2]) = 2.444$ when there was no “effective greenhouse gas” energy flux to
123 558.7ppm or $\log_{10}([eCO_2]) = 2.747$ in 2022, the last date of this timeseries. Within this
124 timeseries, the datapoint corresponding to the year 2023 was not yet published at the time of
125 this study’s publication, but was inferred from a linear projection of the ratio between Mona
126 Loa CO₂ concentrations since 2000
127 (https://gml.noaa.gov/webdata/ccgg/trends/co2/co2_annmean_mlo.txt) and recent eCO₂
128 concentrations ($563.4 \text{ ppm} = [eCO_2]_{2023} \approx 1.34 * [MLO CO_2]_{2023}$).

129 $f_{H_2O}(T_t)$ is the additional atmospheric longwave attenuation due to water vapor and other
130 gasses, including both lapse rate and relative humidity. The precise functional form of this
131 feedback function is unknown, as is the functional form of the two shortwave feedbacks,
132 partially due to disagreements between paleoclimate inferences and ESMs. We thus
133 introduced the following 3 functions, which incorporate an additional 3 positive β
134 coefficients and 1 exponent η . (Note $f_{H_2O}(T_t)$ can be either linearized into a form like these
135 other feedbacks or rewritten in the $(1 - \frac{\phi_{LW}(H_2O \text{ absorb})}{2^{\eta * (T_t)}})$ form.)

136

$$137 \quad f_{H2O}(T_t) \doteq \beta_1 (1/T_t)^\eta \approx 1 - (1 + \beta_1 (T_{2002})^{-\eta} - \beta_1 \eta (T_{2002})^{-\eta-1} (T_t - T_{2002})) \quad (\text{SA13})$$

$$138 \quad f_{\alpha A}(T_t) \doteq 0.834 \left(1 + \beta_2 (T_t - T_{2002}) \right) + \frac{AC_n - AC_{2002}}{\frac{65C}{4} d_{2002}} \quad (\text{SA14})$$

$$139 \quad f_{\alpha S}(T_t) \doteq 0.909 \left(1 + \beta_3 (T_t - T_{2002}) \right) \quad (\text{SA15})$$

140 Finally returning to the heat flux between the surface and the deeper layer of the ocean, other
 141 researchers have modeled this $Q_{\text{surf-deep}}$ as a simple thermal conductivity γ multiplied by the
 142 difference in deviation temperatures between the surface ($\Delta T_t - \Delta \theta_t$), with these deviations
 143 measured relative to the pre-industrial equilibrium.

$$144 \quad Q_{\text{surf-deep}} = \gamma * (\Delta T_t - \Delta \theta_t) = \gamma * (T_t - \theta_t - T_{1850} + \theta_{1850}) \quad (\text{SA16})$$

145 If we take $T_{1850} = 286.66\text{K} = 13.51^\circ\text{C}$ and $\theta_{1850} = 276.66\text{K} = 3.51^\circ\text{C}$, then $\zeta_0 = 10\text{K}$. This
 146 consistent equilibrium temperature difference exists because the ocean is temperature
 147 stratified. We used γ from the CMIP5 reported by Geoffroy et al. Part II (2013) to be
 148 $0.67 \pm 0.15 \text{ W/m}^2/\text{K}$. Estimates of γ from the CMIP6 coupled model comparison project were
 149 almost unchanged, $0.64 \pm 0.14 \text{ W/m}^2/\text{K}$ (Hall and Fox-Kemper 2023). The deep ocean heat
 150 content record was extended back from 1850-1869 by prepending zero values. Since this is
 151 an equilibrium value, the deviation from the equilibrium deep ocean temperature $\theta_{1850} =$
 152 276.66K is given by the deviation from this baseline heat content.

153

154 The ocean heat content anomaly is obtained from Zanna (Zanna, Khatiwala et al. 2019) from
 155 1870-2018. Before 1870, the OHCA was set to 0, with a standard deviation taken to be the
 156 1870-1889 average: 50.2 ZJ. After 2018, the standard deviation was continued as the 2009-
 157 2018 average of 25.2 ZJ. The additional increase in OHCA after 2018 was provided from a
 158 separate NCEI dataset (Levitus, Antonov et al. 2017). This NCEI dataset disagrees with the
 159 Zanna, Khatiwala et al. (2019) dataset regarding the change in OHCA from 2005-2018 by a
 160 factor of 1.71. NCEI reports 134.2 ZJ compared to Zanna (Zanna, Khatiwala et al. 2019)
 161 reporting 78.5 ZJ. However, the NCEI dataset is more directly derived from observations,
 162 especially the Argo array of autonomous floats, and thus is preferred when that array has
 163 been fully available.

164

165

166 **A2: Solving for unknown β coefficients:**

167 Following the definition of climate feedback of w as $\partial N/\partial w * dw/dT$, where N is the TOA
 168 radiative flux (the entire EBM model), we equated the climate feedbacks of each of the three
 169 f_j feedback functions and the Planck response j^* , with the values (in $W/m^2/K$) reported in
 170 Table 7.10 and Figure 7.10 of AR6 (Forster, Storelvmo et al. 2021).

$$171 \quad \frac{\partial N}{\partial j^*} * \frac{dj^*}{dT_t} = -\tilde{g}(t) * f_{H_2O}(T_t) * 4\sigma_{sf}(T_t)^3 = -3.22 \quad (SA17)$$

$$172 \quad \frac{\partial N}{\partial f_{H_2O}(T_t)} * \frac{df_{H_2O}(t)}{dT_t} = -j^*(T_t) * \tilde{g}(t) * -\beta_I p_1(T_t)^{-\eta-1} = 1.30 \quad (SA18)$$

$$173 \quad \frac{\partial N}{\partial f_{aA}(T_t)} * \frac{df_{aA}(T_t)}{dT_t} = 340.2 * \tilde{d}(t) * f_{aS}(T_t) * 0.834 \beta_2 = 0.35 \quad (SA19)$$

$$174 \quad \frac{\partial N}{\partial f_{aS}(T_t)} * \frac{df_{aS}(T_t)}{dT_t} = 340.2 * \tilde{d}(t) * f_{aA}(T_t) * 0.909 \beta_3 = 0.42 \quad (SA20)$$

175 Solving for the exponent by taking the ratio of the first two equations yielded $\eta = 1.615$.
 176 Furthermore, based on the CERES measurements from 2000-2005, everything to the left of
 177 both β_2 (SA19) and β_3 (SA20) is the overall absorbed SW irradiance of $340.2 * 0.707 = 240.5$
 178 W/m^2 , so $\beta_2 = 0.00136 K^{-1}$ and $\beta_3 = 0.00163 K^{-1}$.

179 Figure 3.3 from Zhong and Haigh (2013) shows that per log10 order of magnitude of
 180 [CO2] increase, an additional $15.45 W/m^2$ is absorbed. However, in Forster (2023), the
 181 “greenhouse gas” absorption increases by $12.74 W/m^2$ per log10 order of magnitude of
 182 effective [CO2] increase (eq. SA12). This measurement approximating a partial derivative
 183 was presumably made recently, so we used the more recent 2002 temperature of $\sim 287.5K$
 184 ($14.4^\circ C$), but this choice is relatively inconsequential: $\beta_0\beta_1$ would be only 0.66% larger if the
 185 pre-industrial temperature was used instead. In the pre-industrial climate, we assumed a
 186 steady-state equilibrium with a constant black body temperature of $286.66K$ ($13.6^\circ C$) and a
 187 $\log_{10}([\text{effective CO}_2]) \approx 2.444$. This allows us to solve for β_0 and β_1 as follows:

$$188 \quad 12.74 = \frac{\partial N}{\partial \tilde{g}_n} * \frac{d\tilde{g}_n}{d \log_{10}([eCO_2]_n)} = -\sigma_{sf}(T_n)^4 \beta_I (T_n)^{-1.61} (-\beta_0) \quad (SA21)$$

$$189 \quad 307.24 = \beta_I \beta_0 \quad \text{using } T_{2002} = 287.5 \quad (SA22)$$

$$190 \quad 0 = 340.2 * \tilde{d}_n * f_{aA}(T_{1850}) * f_{aS}(T_{1850}) - \sigma_{sf}(T_{1850})^4 \beta_I (T_{1850})^{-1.61} (1 - \beta_0(2.444)) \quad (SA23)$$

$$191 \quad 240.56 = \sigma_{sf}(286.7)^{2.39} (\beta_I) (1 - \beta_0(2.444)) \quad (SA24)$$

$$192 \quad 5842.68 = (\beta_I) (1 - \beta_0(2.4)) \quad (SA25)$$

$$193 \quad 6593.57 \approx \beta_I \quad \text{and} \quad 0.04660 \approx \beta_0 \quad (SA26)$$

This manuscript has been submitted for publication to JOURNAL OF CLIMATE (AMS). Please note that this manuscript has undergone two rounds of peer review but has yet to be formally accepted for publication. Subsequent versions of this manuscript may differ slightly in content.

194 Checking that Planck partial derivative is accurate, we obtained a value for climate sensitivity
195 of j^* to be $-3.34 \text{ W/m}^2/\text{K}$ at current conditions and the sensitivity of f_{H_2O} to be $1.35 \text{ W/m}^2/\text{K}$,
196 within the likely range of AR6. With an instantaneous doubling or quadrupling of CO_2 the
197 sensitivity of j^* becomes $-3.30 \text{ W/m}^2/\text{K}$ or $-3.22 \text{ W/m}^2/\text{K}$ respectively, matching the reported
198 value. Because they were defined to have proportional climate sensitivities, f_{H_2O} exactly
199 matches AR6 in a $4x\text{CO}_2$ scenario, with $1.30 \text{ W/m}^2/\text{K}$.

200

201

202

203 **Section A3: RTS Smoother**

204

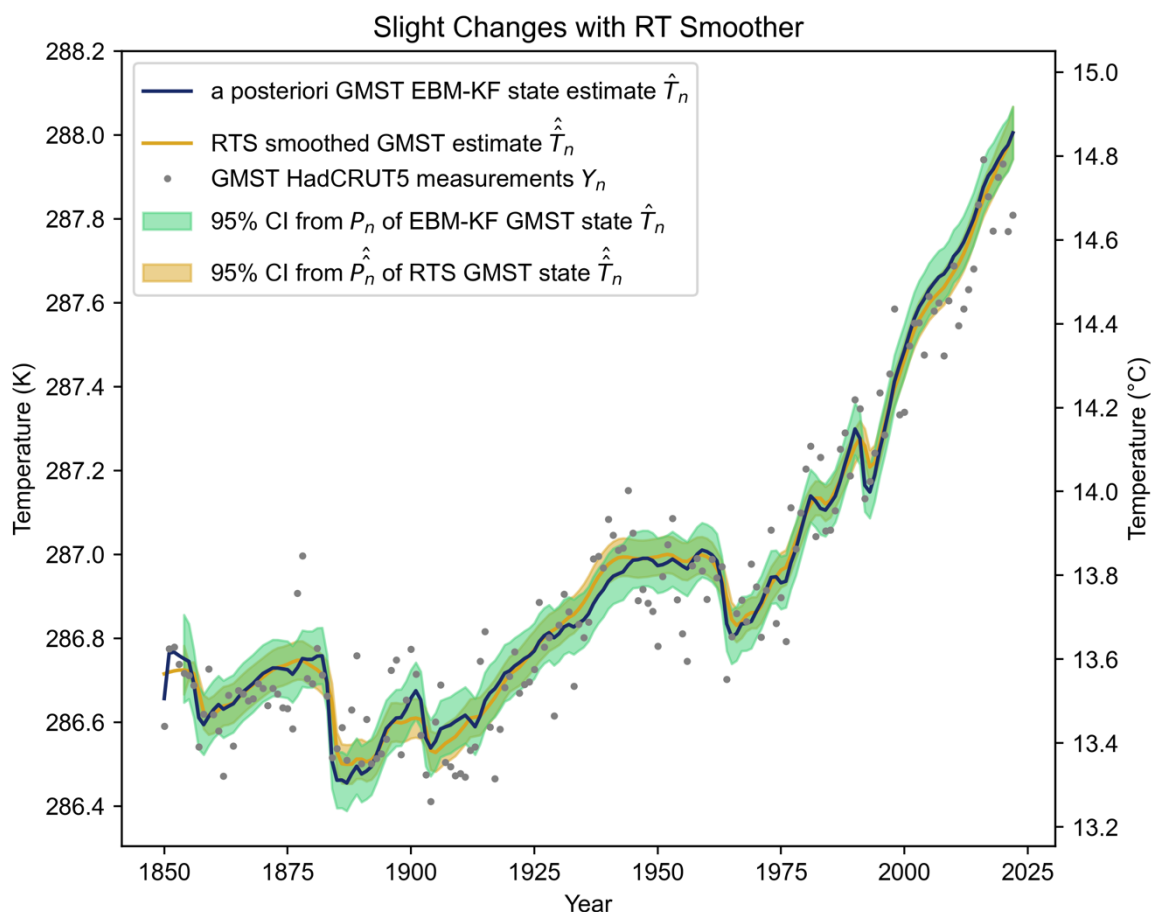
205
$$\widehat{K}_t = P_t \Phi_t (P_{t|t-1})^{-1} \quad \text{back-updated Kalman gain} \quad (\text{SA26})$$

206
$$\widehat{x}_t = \widehat{x}_t + \widehat{K}_t (\widehat{x}_t - \mathbf{F}(\widehat{x}_t, u_{t+1})) \quad \text{back-updated state estimate} \quad (\text{SA27})$$

207
$$\widehat{P}_t = P_t + \widehat{K}_t (\widehat{P}_{t+1} - P_{t|t-1}) \widehat{K}_t^T \quad \text{back-updated state covariance} \quad (\text{SA28})$$

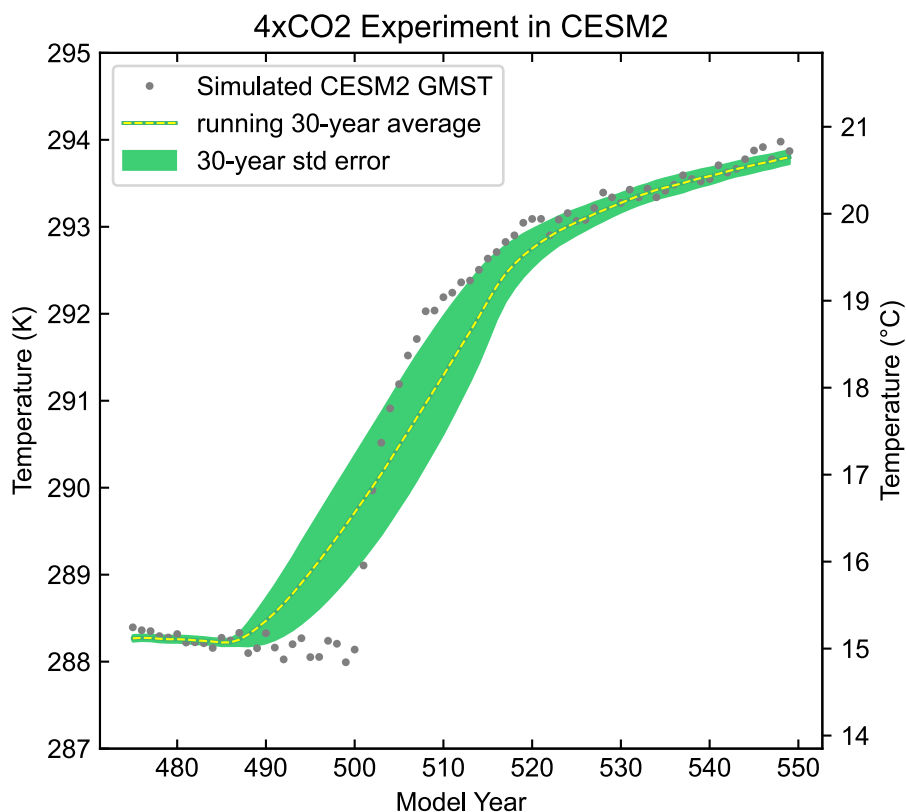
208 This RTS has a theoretical advantage of blending abrupt changes in the model state over
 209 greater time periods, while also slightly reducing the state covariance. For instance, if the
 210 measurements suddenly and persistently diverged from the blind, forward EBM (unrelated to
 211 a known volcanic eruption), an EBM-Kalman Filter model state would only react as these
 212 measurements diverge, whereas an EBM-RTS would slightly foreshadow this jump because
 213 it can see future as well as past measurements. This occurred in 1900: even though the EBM-
 214 KF estimated state is trending up, the EBM-RTS state moves cooler to reflect the colder
 215 GMST measurements from 1902-1907, colder than the EBM predicted from the Santa
 216 Marina volcanic eruption alone (see Supp. Fig. 2). Generally, the EBM-RTS just provides a
 217 second “nudge” toward measurements. However, for the purposes of this paper, these
 218 distinctions make little difference between \widehat{x}_t and \widehat{x}_t , as is demonstrated in Supp. Fig. 1
 219 below.

220

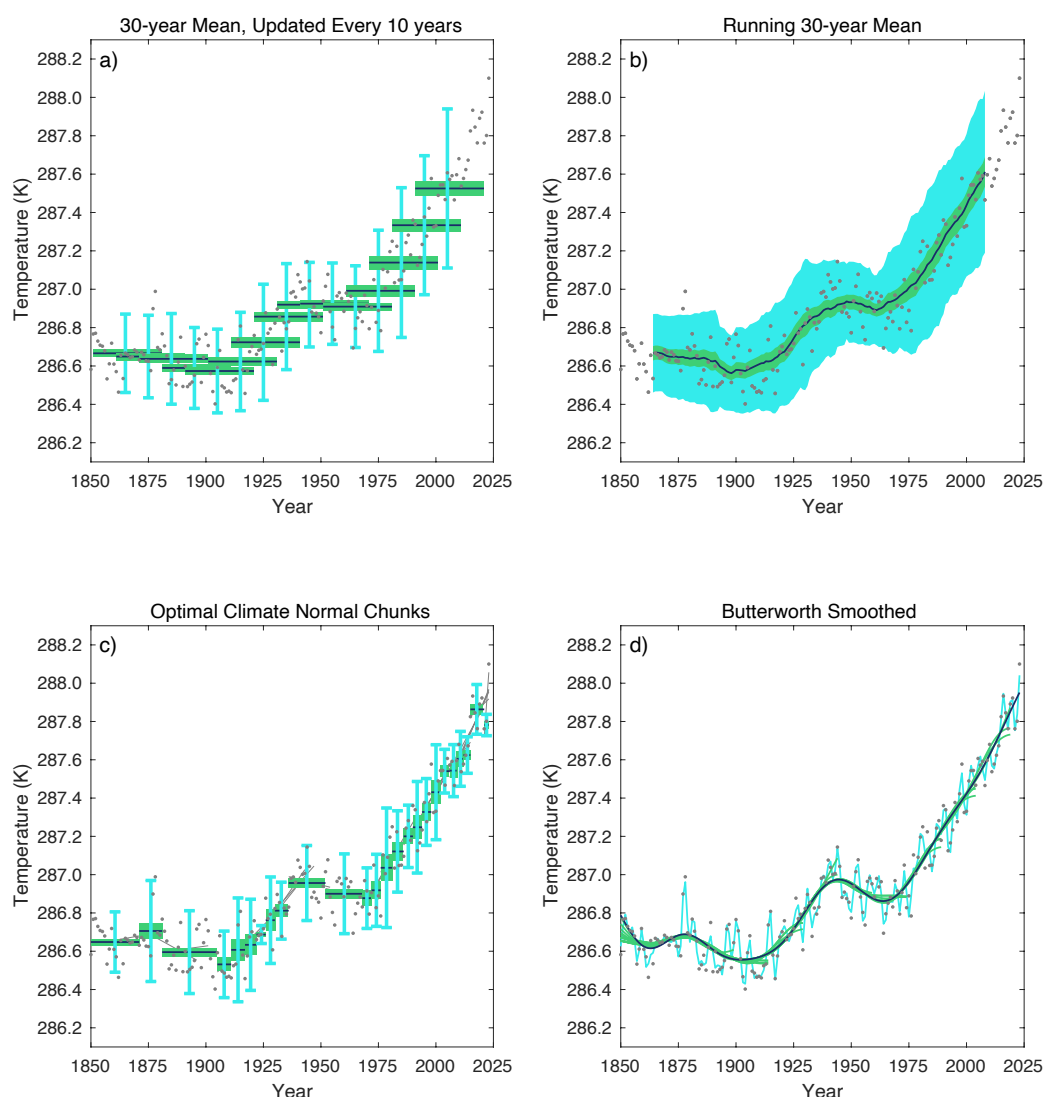


221
 222 Supp. Fig. 2: Comparisons of the original EBM-Kalman Filtered climate state (navy blue line
 223 with green 95% uncertainty window) with an EBM-RTS climate state (orange line with
 224 orange 95% uncertainty window). Note that the temperatures on y-axis are zoomed in relative
 225 to all other figures to demonstrate these minute differences. From 1905-1930 and 2000-2020
 226 when there are repeated cooler GMST temperature measurements than the EBM-KF state
 227 prediction, the EBM-RTS climate state doubly takes these annual temperature measurements
 228 into account, so it has a greater cooling deflection in these periods. Other years are warmer in
 229 the EBM-RTS than the EBM-KF climate state, although even these differences are slight - at
 230 most 0.1K during years of volcanic activity. However, there is greater certainty in the state
 231 estimate with the EBM-RTS: \hat{P}_t shrinks relative to P_t (see Supp. Fig. 10) by factors of 2.25
 232 and 2.84 for the GMST (\hat{p}_t^T) and OHCA (\hat{p}_t^H) components respectively (everywhere except at
 233 the start and tail end of the timeseries). The off-diagonal heat-transfer uncertainty component
 234 of \hat{P}_t is negative and 29 times smaller than those of P_t .
 235

236 **Section B: Alternative Definitions of the Climate State**



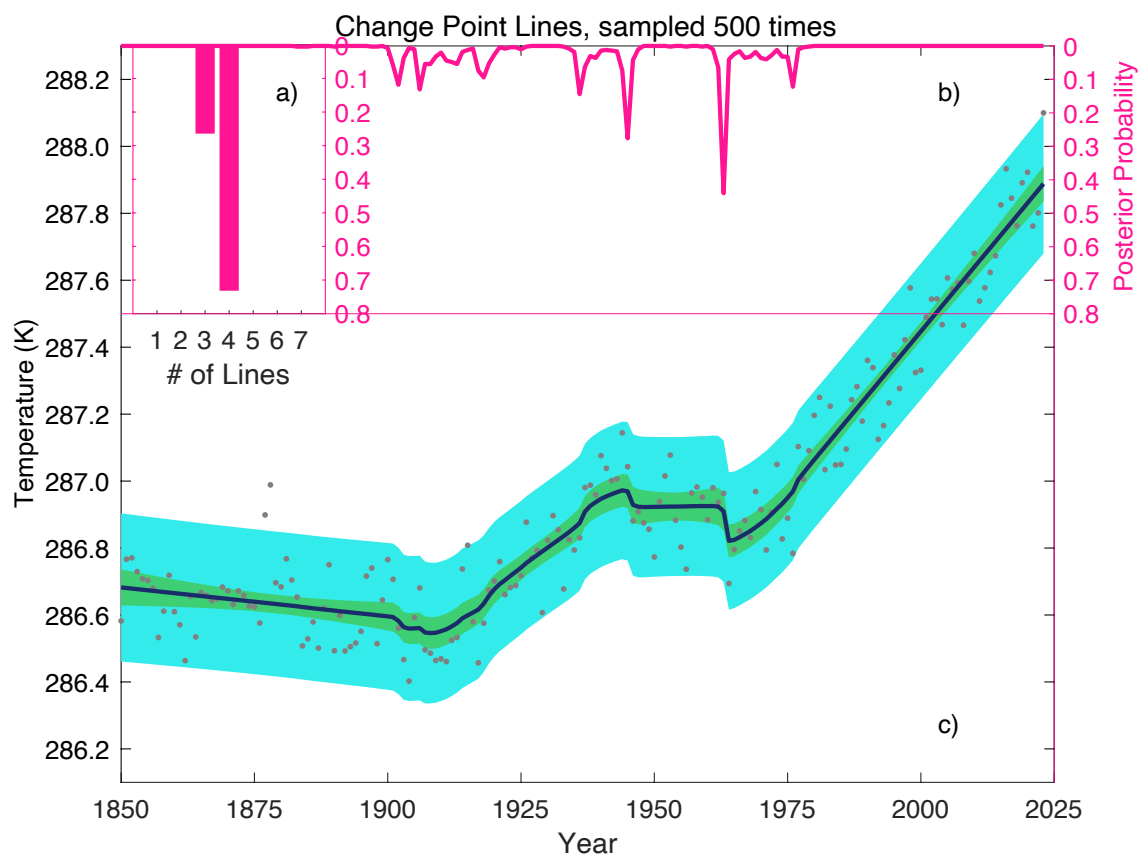
237
238 Supp. Fig. 3: In this modeling experiment conducted within CESM2, the CO₂ concentration
239 was instantaneously quadrupled at year 500. The resulting modeled GMST values are plotted
240 in grey, along with their 30-year running mean (yellow dashed), and the standard error of this
241 mean (green window). The 30-year running average anticipates the jump for 15 years before
242 CO₂ even began to increase, so that the 30-year average "climate" is several °C away from
243 the simulation year 500 temperatures. Then, it fails to increase at the appropriate rate, such
244 that a period of 6 years (505-511) is hotter than the 30-year running average's 95%
245 confidence interval. Only by simulation year 520 does the 30-year running average appear
246 visually to catch up and visually correspond with the simulated temperatures.



247

248 Supp. Fig. 4: Comparison of Prior Methods for Filtering or Smoothing the Climate as applied
 249 to the HadCRUT5 temperature dataset. (Morice, Kennedy et al. 2021) All metrics analogous
 250 to standard deviation are plotted at the 2σ level in light blue, and all metrics analogous to the
 251 standard error are plotted at the 1σ level in light green. a) The 30-year climate normals,
 252 updated every 10 years as per the World Meteorological Association in 1935. b) A running
 253 30-year average. c) Adaptive periods of multiyear averages, known as the optimal climate
 254 normal (OCN). (Livezey, Vinnikov et al. 2007). Chunks became smaller as the rate of climate
 255 change increased in recent decades. d) The Butterworth Smoother applied to this temperature
 256 dataset. (Mann 2008) For the “standard error” highly smoothed lines, the lowpass adaptive,
 257 lowpass mean padded, and lowpass methods were applied to chunks of the timeseries data
 258 ranging from 50 to 170 years in increments of 15 years with a cutoff frequency of $1/30$ years.
 259 The black “best” line a lowpass adaptive curve extended to 2021. The blue “standard
 260 deviation” line is a lowpass mean padded filter with a cutoff frequency of $1/5$ years.

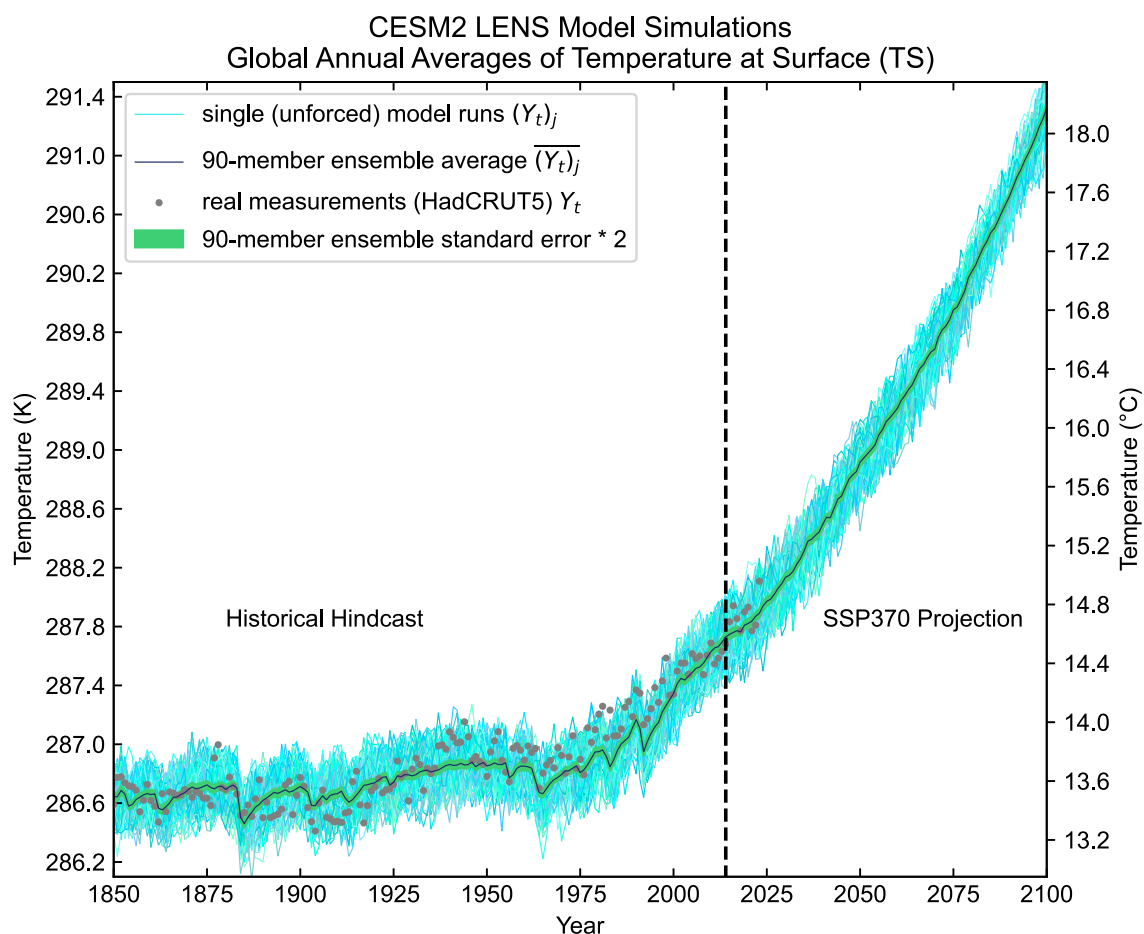
261



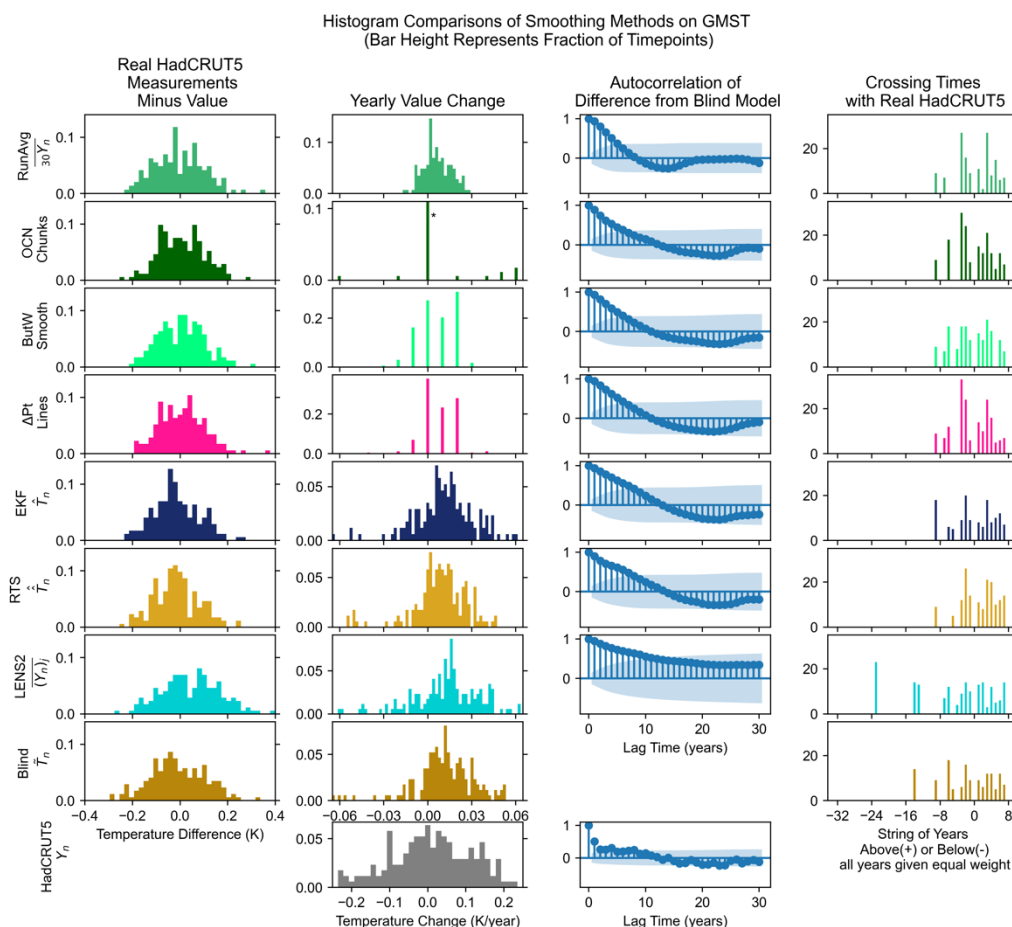
262

263 Supp. Fig. 5: Utilization of Bayesian Change Point on the HadCRUT5 data. (Ruggieri and
264 Antonellis 2016) a) There are likely 4 trendlines with 72% of the posterior probability, and
265 the remaining posterior probability on 3 trendlines. b) The posterior probability plot of where
266 trendlines are most likely to occur: 51.2% of all samplings have a change point occur in 1963,
267 and 26.4% of samplings have a change point occur in 1945. c) The posterior distribution of
268 the trendlines in GMST, again with blue shading to indicate 2σ confidence interval of the
269 data and green shading to indicate 2σ confidence interval of the mean trendline. These trend
270 lines do not have to be continuous (note the dip at 1963), but over many samplings the
271 average trend is smoothed.

272



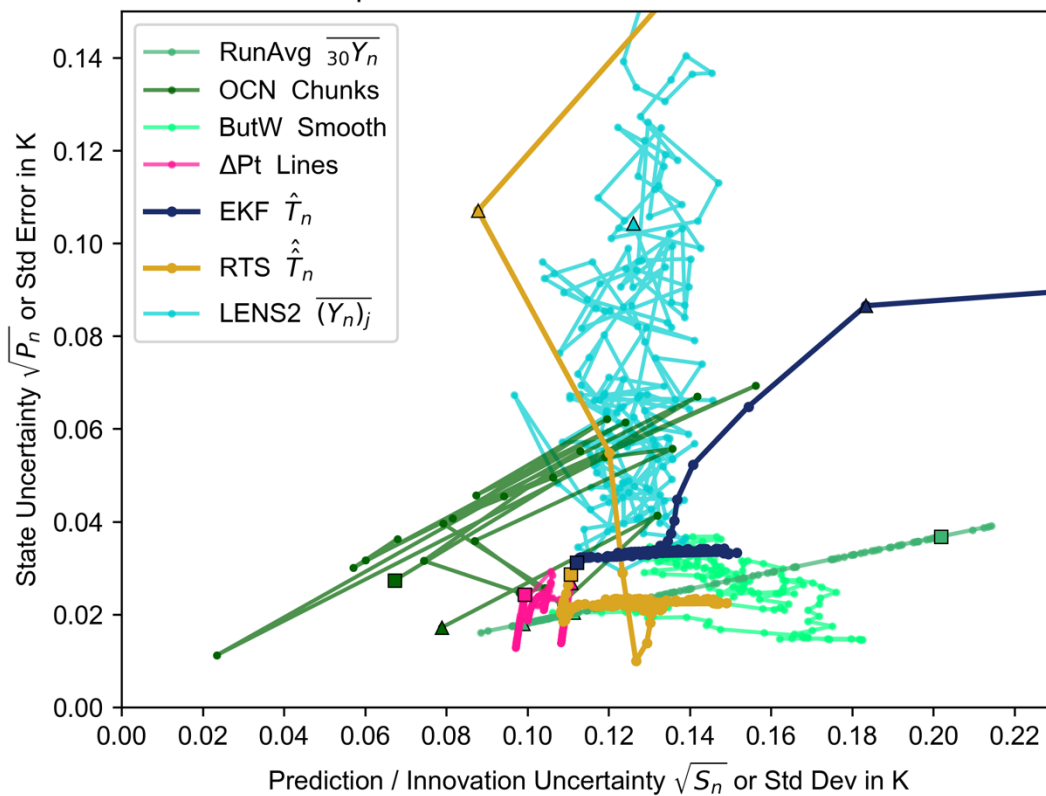
273
 274 Supp. Fig. 6: Comparison of the CESM2 Large Ensemble (LENS2) GSAT (Rodgers, Lee et
 275 al. 2021) with HadCRUT5 GMST measurements. The various shades of thin light blue and
 276 turquoise lines represent each individual simulation ($Y_n)_j$ of the 90-member ensemble. The
 277 ensemble mean is plotted in a navy-blue line, and the ensemble mean standard error is plotted
 278 around this line in green. This standard error is twice the standard deviation divided by the
 279 square root of the number of ensemble members at that moment and shows the 2σ uncertainty
 280 in the yearly simulated climate is roughly 0.026K. The ensemble mean has $r^2 = 0.83$ relative
 281 to the HadCRUT5 measurements, lower than for the blind EBM ($r^2=0.88$). The dashed
 282 vertical line represents when LENS transitions from historical to future forcing (SSP3-7.0).
 283



284

285 Supp. Fig. 7: Histogram comparisons of several aspects of many of the smoothing methods
 286 for generating a climate timeseries. The far-left column represents the absolute differences
 287 between the HadCRUT5 measurements and all the other models. All look similar in this
 288 respect. The center-left column shows the annual changes in the temperatures reported by
 289 each model. In this respect, the real HadCRUT5 measurements are the most spread out,
 290 because the stochastic change each year is large, whereas in most years the OCN Chunks do
 291 not change. The center-right column shows an autocorrelation plot, which demonstrates that
 292 every other model aside from HadCRUT5 (and to a lesser extent the running average) are
 293 autocorrelated with the blind energy-balance model to similar degrees. The far-right column
 294 shows how many continuous years are spent above or below HadCRUT5: both the LENS2
 295 ensemble average and the blind energy-balance model had >20 year spans for which they
 296 were colder than the “real” HadCRUT5 data, illustrating the benefit of data assimilation.
 297

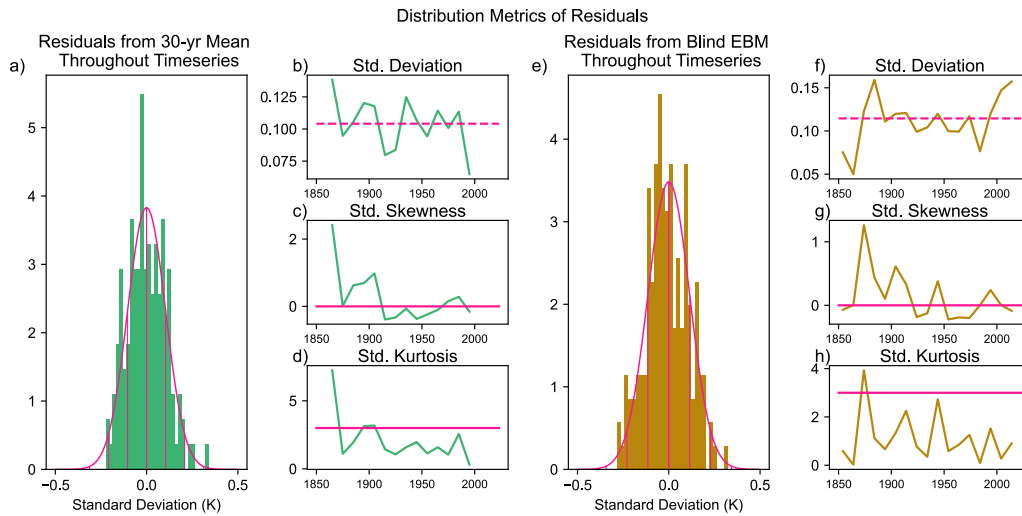
Comparison of Modeled GMST Variabilities



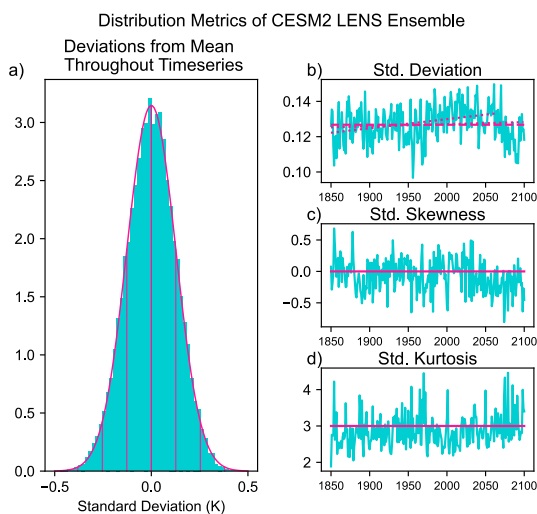
298
299
300
301
302
303
304
305
306
307
308
309
310
311
312
313
314
315
316
317
318
319
320
321
322
323
324

Supp. Fig. 8: Comparisons of the state and prediction (or equivalent) uncertainties of the smoothing methods for generating a climate timeseries. The x-axis represents the state uncertainty (colored light green in all other figures), and the y-axis represents the prediction uncertainty (colored light blue and doubled in all other figures). As these quantities change over time, all points in these smoothing timeseries are connected with colored lines, with the triangle Δ representing the value of these quantities in 1850 or the first point that they entered the frame limits of this graph, and the square \square representing the value of these quantities in 2021 or the last point that they were within the frame limits. For instance, the running average draws a straight line because standard deviation and standard error are linearly correlated by a factor of $1/\sqrt{30}$, and latter points have larger quantities for each variability due to the changing climate. The Butterworth Smoother traces a curve roughly in this region, with both the standard deviations and standard errors being twice the 15-year running average of the maximum of the absolute value of differences between colored and black curves. The EKF and RTS methods rapidly converge to an innovation uncertainty of 0.11-0.15K and state uncertainties of 0.034K and 0.023K respectively. The Change Point Regression variance also fluctuate the same region as the RTS, although change point method's standard error twice drops to 0.014K, and the prediction uncertainty is slightly smaller, 0.10-0.11K. Both the OCN and the LENS2 climates have standard errors that are above the other methods at most times. For LENS2, the standard deviation within the CESM2 ensemble generally remains between 0.11K and 0.14K, whereas the state uncertainty is taken to be the standard deviation of the 20 ensembles comprising [CMIP6](#) in October 2021. (Meehl, Moss et al. 2014) These metrics are unrelated to Figure 10 in the main text. Within CMIP6, the 20 ensembles are closest to agreement in 1939, when the state uncertainty dipped down to only 0.029K between ensemble means, but this uncertainty was much greater at earlier and later time points, reaching 0.183K by 2014.

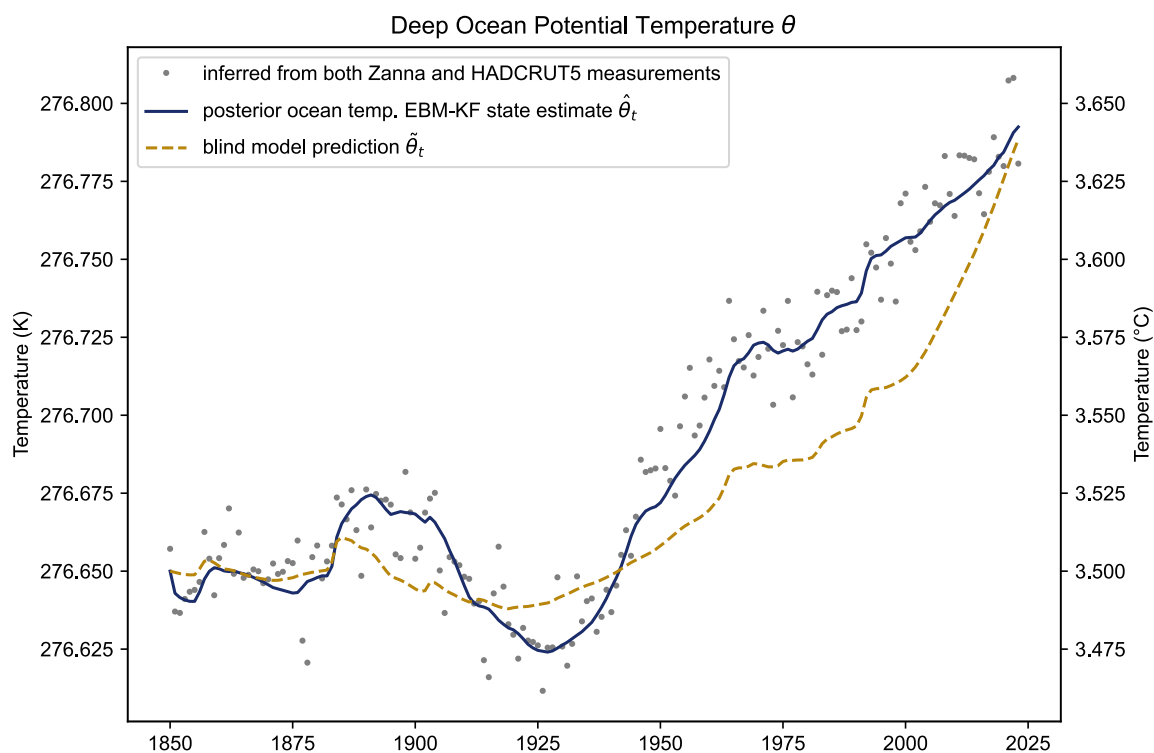
325 **Section C: Miscellaneous Additional Figures**



326
 327 Supp. Fig. 9: Left panels show statistical features of the residuals between the HadCRUT5
 328 measurements with respect to their 30-year running mean, which have a bias of -0.00339K .
 329 Pink lines in the histogram in (a) depict an ideal Gaussian distribution with standard deviation
 330 of 0.105K , and vertical lines drawn for each of these standard deviations. The dashed pink
 331 line (b) indicates the overall standard deviation. Solid pink lines for the skewness = 0.147 (c)
 332 and kurtosis = 1.904 (d) indicate the ideal values for a Gaussian distribution.
 333 Right panels show statistical features of the differences between the HadCRUT5
 334 measurements with respect to the blind EBM, which have a bias of -0.00104K . Pink lines in
 335 the histogram in (e) depict an ideal Gaussian distribution with standard deviation of 0.115K ,
 336 and vertical lines drawn for each of these standard deviations. The dashed pink line (f)
 337 indicates the overall standard deviation. The skewness = 0.123 (g) and kurtosis = 1.208 (h)
 338 differ from the ideal values for a Gaussian distribution indicated by solid pink lines.
 339
 340
 341



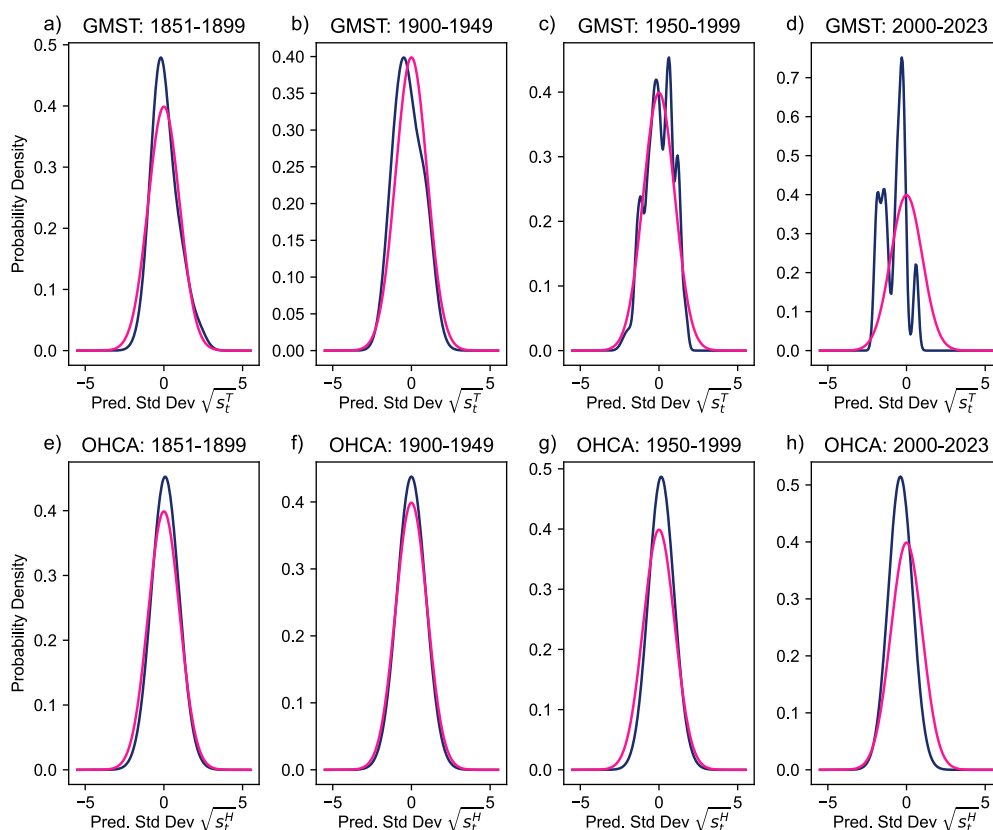
336
 337 Supp. Fig. 10: Statistical Features of the CESM2 Large Ensemble. (Rodgers, Lee et
 338 al. 2021). Pink lines in the histogram in (a) depict an ideal Gaussian distribution
 339 with standard deviation of 0.127K , and vertical lines drawn for each of these
 340 standard deviations. The observed trend (b) up until 2065 ($p < 0.001$) and overall
 341 ($p = 0.168$) in the standard deviation over time is plotted in a dotted pink, while the
 dashed line indicates the overall standard deviation of 0.127K . The skewness = -0.069 (c)
 and kurtosis = 2.87 (d) differ from the ideal values for a Gaussian
 distribution indicated by solid pink lines.



357

358 Supp. Fig. 11: As in Fig. 2, but regarding the deep ocean potential temperature. A comparison
359 of the blind model EBM, the a posteriori EKF state estimate, and the inferred deep ocean
360 potential by combining the Zanna (2019) and HadCRUT5 measurements with the surface and
361 deep ocean heat capacities specified in Section 2a and Appendix A.

EBM-KF Residuals Over Time

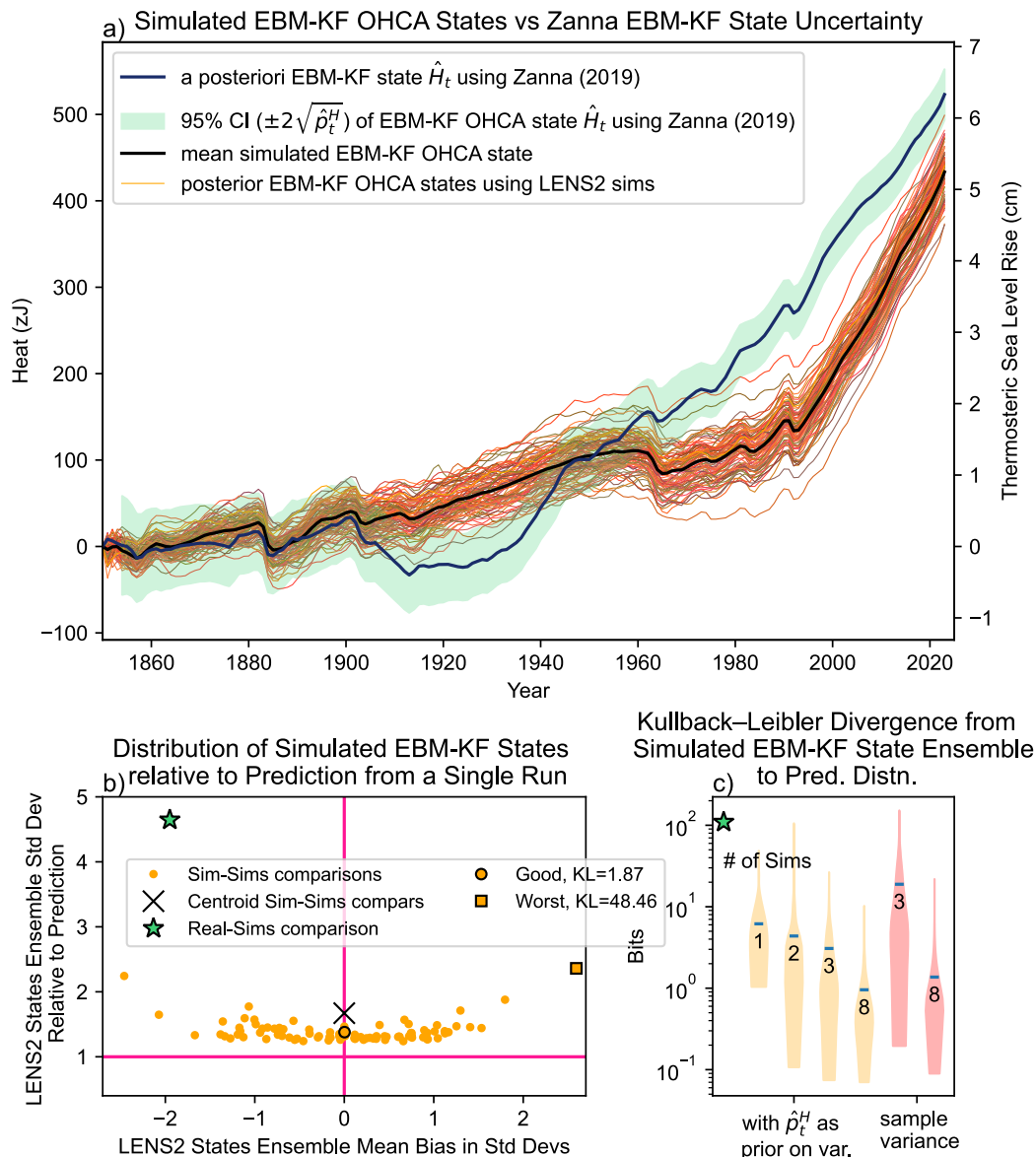


362

363 Supp. Fig. 12: Deviation between the projected climate state (pink) and empirical PDFs of the
 364 Gaussian mixture of measurements with associated uncertainty (purple), plotted relative to
 365 the ideal distribution given by the innovation covariance. Each column indicates a different
 366 time window of the EMB-KF model's run length. The top row displays the empirical PDFs of
 367 the GMST HadCRUT5 measurements relative to the model's estimate of GMST state,
 368 whereas the bottom row displays empirical PDFs of the OHCA Zanna 2019 measurements
 369 relative to the model's estimate of OHCA state. Note the initial period begins at 1851 (and
 370 the 1850 measurement is excluded from main text Fig. 3 and 4) because this has comparison
 371 involves P_0 , which was intentionally over-estimated (resulting in relatively too-narrow
 372 measurement kernel). Also note that the last period is less than half the time of the others, so
 373 the GMST empirical distribution is much choppier. The observations from this most recent
 374 period 2000-2023 are also shifted slightly colder than the EMB-KF predictions, possibly
 375 indicating that some of the parameters could be better tuned than the original literature
 376 values.

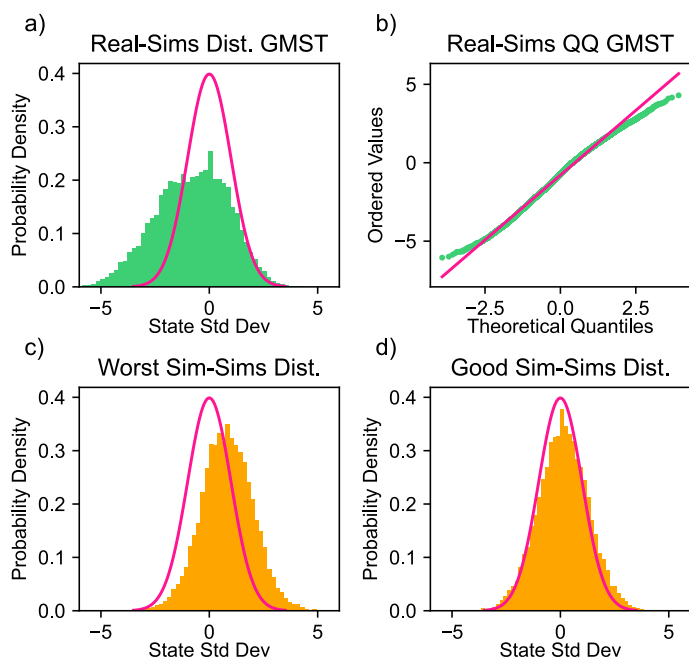
377

378

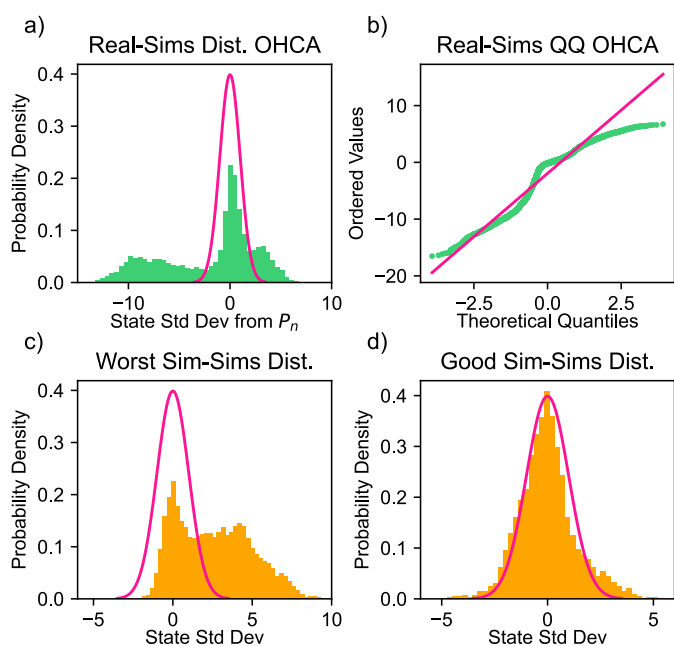


379

380 Supp. Fig. 13: As in Fig. 7, but focusing on the OHCA component rather than GMST. a) The
 381 EBM-KF *a posteriori* from Zanna (2019) state estimate (thick blue) and its 95% confidence
 382 interval (light green), along with EBM-KF state estimates for each individual CESM2
 383 ensemble member (orange lines) and their mean (thick black line). b) The differences
 384 between the “real” measurement based Zanna (2019) climate state and all LENS2 climate
 385 states, scaled by the state standard deviation and plotted against the ideal normal distribution.
 386 This is a particularly ill-fitting distribution because the LENS timeseries of OHCA differ
 387 substantially from the Zanna (2019) observation. c) In the quantile-quantile plot, this
 388 disagreement is apparent between the “real” measurement based Zanna (2019) climate state
 389 and all LENS2 climate states of OHCA. d) Climate states and associated uncertainties arising
 390 from each of 90 LENS2 simulations and Zanna (2019) are compared to all other LENS2
 391 climate states, and the bias and standard deviation respect to a particular member, of the
 392 resulting empirical distributions are plotted. e) An example of these empirical distributions is
 393 graphed, indicated by the point circled in black within the scatterplot. The expected
 394 difference across an entire simulation run between $(\hat{H}_t)_i$ and $(\hat{H}_t)_j$ is $\pm 0.721(\sqrt{p_t^T})_i$ with range
 395 $(-2.439 - 2.574)$, or 12.72ZJ with range $(-40.47 - 42.85)$ ZJ.



396
 397 Supp. Fig. 14 (a) The differences between the “real” measurement based HadCRUT5 climate
 398 state and all LENS2 climate states, scaled by the state standard deviation and plotted against
 399 the ideal normal distribution. b) In the quantile-quantile plot, these differences between the
 400 “real” measurement based HadCRUT5 climate state and all LENS2 climate states
 401 distributions agree. c) The “worst” (by Kullback-Leibler divergence) correspondence
 402 between the predicted GMST ensemble distribution (pink) and the actual LENS2 ensemble
 403 (orange), indicated by the point outlined with a square within the Fig. 7b scatterplot. d) An
 404 example a “good” (25th percentile by Kullback-Leibler divergence) correspondence between
 405 the predicted ensemble distribution (pink) and the actual LENS2 ensemble (orange),
 406 indicated by the point circled in black within the Fig. 7b scatterplot.



407
 408 Supp. Fig. 15: As for Supp. Fig. 14, but regarding OHCA instead of GMST.

409 **Section D: Justification that the EKF is sufficient for nonlinearity, will not diverge**

410 The issue of nonlinearity arises not in the computation of $\hat{\mathbf{x}}_{t+1} = \mathbf{F}(\hat{\mathbf{x}}_{t-1})$ but rather the
 411 covariance distribution \mathbf{P}_t of points (infinitesimal probability masses) neighboring $\hat{\mathbf{x}}_{t-1}$, which
 412 are assumed to scale linearly around this transformation to maintain a normal distribution.
 413 The OHCA part of the model is linear, producing 2nd-order derivatives which are 0 (SC3,
 414 SC10). Nonlinear distortion may pile more probability density onto a state other than the
 415 transformed original projection $\mathbf{F}(\hat{\mathbf{x}}_{t-1})$, necessitating a new computation of $\hat{\mathbf{x}}_{t+1}$ as the mean
 416 of this distorted PDF. Thus, for an arbitrary point that is z standard deviations away from $\hat{\mathbf{x}}_{t-1}$,
 417 tracing out an ellipse that is symbolized as $\mathbf{z}\sqrt{\mathbf{P}_t}$ the remainder error \mathbf{R}_1 (Lagrange mean-
 418 value form) induced in a single cycle is:

$$419 \quad \mathbf{F}(\hat{\mathbf{x}}_{t-1} + \mathbf{z}\sqrt{\mathbf{P}_t}; u_t) - \mathbf{F}(\hat{\mathbf{x}}_{t-1}) - \frac{\partial \mathbf{F}(x; u_t)}{\partial T} (\mathbf{z}\sqrt{\mathbf{P}_t})|_T - \frac{\partial \mathbf{F}(x; u_t)}{\partial H} (\mathbf{z}\sqrt{\mathbf{P}_t})|_H = \mathbf{R}_1(\hat{\mathbf{x}}_{t-1} + \mathbf{z}\sqrt{\mathbf{P}_t})$$

420 (SC1)

421 This is a vector equation with two components, T_{t+1} and H_{t+1} Splitting this remainder term
 422 into its two components, starting with T_{t+1} :

$$423 \quad \mathbf{R}_{1,T_{t+1}}(\hat{\mathbf{x}}_{t-1} + \mathbf{z}\sqrt{\mathbf{P}_t}; u_t) = \frac{\partial^2 F_T(\xi_{T1}, \xi_{H1}; u_n)}{\partial T \partial T} \frac{(\xi_{T1} - T_{t-1})^2}{2}$$

$$424 \quad + \frac{\partial^2 F_T(\xi_{T1}, \xi_{H1}; u_n)}{\partial T \partial H} (\xi_{T1} - T_{t-1})(\xi_{H1} - H_{t-1}) + \frac{\partial^2 F_T(\xi_{T1}, \xi_{H1}; u_n)}{\partial H \partial H} \frac{(\xi_{H1} - H_{t-1})^2}{2}$$

425 for $[\xi_{T1}, \xi_{H1}] = \hat{\mathbf{x}}_{t-1} + \mathbf{z}\xi_1\sqrt{\mathbf{P}_t}$, where $0 \leq |z_{\xi_1}| \leq z$ (SC2)

$$427 \quad \frac{\partial T_{t+1}}{\partial H_t} = \frac{\gamma}{C_{\text{surf}} C_{\text{deep}}}, \text{ so } \frac{\partial^2 F_T}{\partial T \partial H} = \frac{\partial^2 F_T}{\partial H \partial H} = 0$$

428 (SC3)

$$429 \quad \frac{\partial^2 F_T}{\partial T \partial T} = \frac{137.6 * 2\beta_2\beta_3}{\text{AOD}_t + 9.73} - \frac{1.39 * 2.39 \sigma_{sf}\beta_1}{C_{\text{surf}}} (T_t)^{0.39} (1 - \beta_0 \log_{10}([\text{eCO}_2]_t))$$

430 (SC4)

$$431 \quad \mathbf{R}_{1,T_{t+1}}(\hat{\mathbf{x}}_{t-1} + \mathbf{z}\sqrt{\mathbf{P}_t}; u_t) = \frac{(z\sqrt{\hat{p}_{t-1}^T})^2}{2} * \left(\frac{0.00061}{\text{AOD}_t + 9.73} - 7.26 \text{ E} - 5 (T_t)^{0.39} (1 - \beta_0 \log_{10}([\text{eCO}_2]_t)) \right)$$

432 (SC5)

$$433 \quad |\mathbf{R}_{1,T_{t+1}}(\hat{\mathbf{x}}_{t-1} + \mathbf{z}\sqrt{\mathbf{P}_t}; u_t)| \leq \frac{z^2 \hat{p}_{t-1}^T}{2} |6.15 \text{ E} - 5 - 5.685 \text{ E} - 4| \leq \frac{z^2 \hat{p}_{t-1}^T}{2} * 0.0005$$

434 (SC6)

$$434 \quad \hat{p}_{t-1}^T \leq 0.003 \text{ after } t = 1855$$

435 (SC7)

$$435 \quad |\mathbf{R}_{1,T_{t+1}}(\hat{\mathbf{x}}_{t-1} + \mathbf{z}\sqrt{\mathbf{P}_t}; u_t)| \leq 10^{-7} z^2 * 7.5$$

(SC8)

436 This means that all probability masses that are within $|z| < 4$ standard deviations regarding the
 437 T component will have a one-step error of $< 0.000012\text{K}$. Even if the error accumulates in the
 438 same direction in each cycle of the EKF, over the 174 year timeseries, the error will be within
 439 0.002K compared to a particle method such as the Unscented Kalman Filter. (Julier and
 440 Uhlmann 1997; Wan and Van Der Merwe 2000)

441

442 Splitting this remainder term into its second component, H_{t+1} :

$$443 \quad \mathbf{R}_{1,H_{t+1}}(\hat{\mathbf{x}}_{t-1} + \mathbf{z}\sqrt{\mathbf{P}_t}; \mathbf{u}_t) = \frac{\partial^2 F_H(\xi_{T2}, \xi_{H1}; u_n)}{\partial T \partial T} \frac{(\xi_{T1} - T_{t-1})^2}{2} +$$

$$444 \quad \frac{\partial^2 F_H(\xi_{T1}, \xi_{H1}; u_n)}{\partial T \partial H} (\xi_{T1} - T_{t-1})(\xi_{H1} - H_{t-1}) + \frac{\partial^2 F_H(\xi_{T1}, \xi_{H1}; u_n)}{\partial H \partial H} \frac{(\xi_{H1} - H_{t-1})^2}{2}$$

$$445 \quad \text{for } [\xi_{T2}, \xi_{H2}] = \hat{\mathbf{x}}_{t-1} + \mathbf{z}\xi_2\sqrt{\mathbf{P}_t}, \text{ where } 0 \leq |z_{\xi_2}| \leq z \quad (\text{SC9})$$

$$449 \quad \frac{\partial H_{t+1}}{\partial \mathbf{H}_t} = \frac{\gamma}{C_{\text{deep}}} * \left(\frac{C_{\text{upper0}}}{C_{\text{surf}}} - 1 \right) + 1, \text{ so } \frac{\partial^2 F_H}{\partial T \partial H} = \frac{\partial^2 F_H}{\partial H \partial H} = 0 \quad (\text{SC10})$$

$$451 \quad \frac{\partial^2 F_H}{\partial T \partial T} = C_{\text{upper0}} * \frac{\partial T_{t+1}}{\partial T \partial T} \quad (\text{SC11})$$

$$453 \quad \mathbf{R}_{1,H_{t+1}}(\hat{\mathbf{x}}_{t-1} + \mathbf{z}\sqrt{\mathbf{P}_t}; \mathbf{u}_t) = \frac{(z\sqrt{\hat{p}_{t-1}^T})^2}{2} * C_{\text{upper0}} * \mathbf{R}_{1,T_{t+1}}(\hat{\mathbf{x}}_{t-1} + \mathbf{z}\sqrt{\mathbf{P}_t}; \mathbf{u}_t) \quad (\text{SC12})$$

454 Repeating the logic above, this means that all probability masses that are within $|z| < 4$
 455 standard deviations will have a one-step error of < 0.0016 ZJ. Even if the error accumulates in
 456 the same direction in each cycle of the EKF, over the 174 year timeseries, the error will be
 457 within 0.28 ZJ compared to a particle method such as the Unscented Kalman Filter. (Julier
 458 and Uhlmann 1997; Wan and Van Der Merwe 2000)

459
 460

461 **Section E: References**
462

463 Boltzmann, L. (1884). "Ableitung des Stefan'schen Gesetzes, betreffend die Abhängigkeit der
464 Wärmestrahlung von der Temperatur aus der electromagnetischen Lichttheorie." Annalen der
465 Physik **258**(6): 291-294 DOI: <https://doi.org/10.1002/andp.18842580616>.

466 Coddington, O., J. L. Lean, D. Lindholm, P. Pilewskie, M. Snow and N. C. Program (2017).
467 NOAA Climate Data Record (CDR) of Total Solar Irradiance (TSI), NRLTSI Version 2.1. N.
468 N. C. f. E. Information DOI: <https://doi.org/10.7289/V56W985W>.

469 Forster, P., T. Storelvmo, K. Armour, W. Collins, J. L. Dufresne, D. Frame, D. J. Lunt, T.
470 Mauritsen, M. D. Palmer, M. Watanabe, M. Wild and H. Zhang (2021). The Earth's Energy
471 Budget, Climate Feedbacks, and Climate Sensitivity. Climate Change 2021: The Physical
472 Science Basis. Contribution of Working Group I to the Sixth Assessment Report of the
473 Intergovernmental Panel on Climate Change. V. Masson-Delmotte, P. Zhai, A. Pirani et al.
474 Cambridge, United Kingdom and New York, NY, USA, Cambridge University Press: 923–
475 1054 DOI: 10.1017/9781009157896.009.

476 Forster, P. M., C. J. Smith, T. Walsh, W. F. Lamb, R. Lamboll, M. Hauser, A. Ribes, D.
477 Rosen, N. Gillett, M. D. Palmer, J. Rogelj, K. von Schuckmann, S. I. Seneviratne, B. Trewin,
478 X. Zhang, M. Allen, R. Andrew, A. Birt, A. Borger, T. Boyer, J. A. Broersma, L. Cheng, F.
479 Dentener, P. Friedlingstein, J. M. Gutiérrez, J. Gütschow, B. Hall, M. Ishii, S. Jenkins, X.
480 Lan, J. Y. Lee, C. Morice, C. Kadow, J. Kennedy, R. Killick, J. C. Minx, V. Naik, G. P.
481 Peters, A. Pirani, J. Pongratz, C. F. Schleussner, S. Szopa, P. Thorne, R. Rohde, M. Rojas
482 Corradi, D. Schumacher, R. Vose, K. Zickfeld, V. Masson-Delmotte and P. Zhai (2023).
483 "Indicators of Global Climate Change 2022: annual update of large-scale indicators of the
484 state of the climate system and human influence." Earth Syst. Sci. Data **15**(6): 2295-2327
485 DOI: 10.5194/essd-15-2295-2023.

486 Geoffroy, O., D. Saint-Martin, G. Bellon, A. Voltaire, D. J. L. Olivié and S. Tytéca (2013).
487 "Transient Climate Response in a Two-Layer Energy-Balance Model. Part II: Representation
488 of the Efficacy of Deep-Ocean Heat Uptake and Validation for CMIP5 AOGCMs." Journal
489 of Climate **26**(6): 1859-1876 DOI: <https://doi.org/10.1175/JCLI-D-12-00196.1>.

490 Hall, G. and B. Fox-Kemper (2023). "Regional mixed layer depth as a climate diagnostic and
491 emergent constraint." Geophysical Research Letters [**Preprint, personal communication**].

492 Harshvardhan and M. D. King (1993). "Comparative Accuracy of Diffuse Radiative
493 Properties Computed Using Selected Multiple Scattering Approximations." Journal of the
494 Atmospheric Sciences **50**(2): 247-259 DOI: 10.1175/1520-
495 0469(1993)050<0247:caodrp>2.0.co;2.

496 Julier, S. J. and J. K. Uhlmann (1997). New extension of the Kalman filter to nonlinear
497 systems. Proc.SPIE DOI: 10.1117/12.280797.

498 Kravitz, B., P. J. Rasch, H. Wang, A. Robock, C. Gabriel, O. Boucher, J. N. S. Cole, J.
499 Haywood, D. Ji, A. Jones, A. Lenton, J. C. Moore, H. Muri, U. Niemeier, S. Phipps, H.
500 Schmidt, S. Watanabe, S. Yang and J. H. Yoon (2018). "The climate effects of increasing
501 ocean albedo: an idealized representation of solar geoengineering." Atmos. Chem. Phys.
502 **18**(17): 13097-13113 DOI: 10.5194/acp-18-13097-2018.

503 Levitus, S., J. I. Antonov, T. P. Boyer, O. K. Baranova, H. E. García, R. A. Locarnini, A. V.
504 Mishonov, J. R. Reagan, D. Seidov, E. Yarosh and M. M. Zweng (2017). NCEI ocean heat
505 content, temperature anomalies, salinity anomalies, thermocline sea level anomalies,
506 halosteric sea level anomalies, and total steric sea level anomalies from 1955 to present

This manuscript has been submitted for publication to JOURNAL OF CLIMATE (AMS). Please note that this manuscript has undergone two rounds of peer review but has yet to be formally accepted for publication. Subsequent versions of this manuscript may differ slightly in content.

- 507 calculated from in situ oceanographic subsurface profile data. NOAA National Centers for
508 Environmental Information DOI: <https://doi.org/10.7289/v53f4mvp>.
- 509 Livezey, R. E., K. Y. Vinnikov, M. M. Timofeyeva, R. Tinker and H. M. van den Dool
510 (2007). "Estimation and Extrapolation of Climate Normals and Climatic Trends." *Journal of*
511 *Applied Meteorology and Climatology* **46**(11): 1759-1776 DOI: 10.1175/2007JAMC1666.1.
- 512 Loeb, N. G., B. A. Wielicki, D. R. Doelling, G. L. Smith, D. F. Keyes, S. Kato, N. Manalo-
513 Smith and T. Wong (2009). "Toward Optimal Closure of the Earth's Top-of-Atmosphere
514 Radiation Budget." *Journal of Climate* **22**(3): 748-766 DOI: 10.1175/2008jcli2637.1.
- 515 Mann, M. E. (2008). "Smoothing of climate time series revisited." *Geophysical Research*
516 *Letters* **35**(16) DOI: <https://doi.org/10.1029/2008GL034716>.
- 517 Meehl, G. A., R. Moss, K. E. Taylor, V. Eyring, R. J. Stouffer, S. Bony and B. Stevens
518 (2014). "Climate Model Intercomparisons: Preparing for the Next Phase." *Eos, Transactions*
519 *American Geophysical Union* **95**(9): 77-78 DOI: <https://doi.org/10.1002/2014EO090001>.
- 520 Meinshausen, M., Z. R. J. Nicholls, J. Lewis, M. J. Gidden, E. Vogel, M. Freund, U. Beyerle,
521 C. Gessner, A. Nauels, N. Bauer, J. G. Canadell, J. S. Daniel, A. John, P. B. Krummel, G.
522 Luderer, N. Meinshausen, S. A. Montzka, P. J. Rayner, S. Reimann, S. J. Smith, M. van den
523 Berg, G. J. M. Velders, M. K. Vollmer and R. H. J. Wang (2020). "The shared socio-
524 economic pathway (SSP) greenhouse gas concentrations and their extensions to 2500."
525 *Geosci. Model Dev.* **13**(8): 3571-3605 DOI: 10.5194/gmd-13-3571-2020.
- 526 Morice, C. P., J. J. Kennedy, N. A. Rayner, J. P. Winn, E. Hogan, R. E. Killick, R. J. H.
527 Dunn, T. J. Osborn, P. D. Jones and I. R. Simpson (2021). "An Updated Assessment of Near-
528 Surface Temperature Change From 1850: The HadCRUT5 Data Set." *Journal of Geophysical*
529 *Research: Atmospheres* **126**(3): e2019JD032361 DOI:
530 <https://doi.org/10.1029/2019JD032361>.
- 531 Nasa/Larc/Sd/Asdc (2018). Global Space-based Stratospheric Aerosol Climatology Version
532 2.0.
- 533 Rodgers, K. B., S. S. Lee, N. Rosenbloom, A. Timmermann, G. Danabasoglu, C. Deser, J.
534 Edwards, J. E. Kim, I. R. Simpson, K. Stein, M. F. Stuecker, R. Yamaguchi, T. Bódai, E. S.
535 Chung, L. Huang, W. M. Kim, J. F. Lamarque, D. L. Lombardozzi, W. R. Wieder and S. G.
536 Yeager (2021). "Ubiquity of human-induced changes in climate variability." *Earth Syst.*
537 *Dynam.* **12**(4): 1393-1411 DOI: 10.5194/esd-12-1393-2021.
- 538 Ruggieri, E. and M. Antonellis (2016). "An exact approach to Bayesian sequential change
539 point detection." *Computational Statistics & Data Analysis* **97**: 71-86 DOI:
540 <https://doi.org/10.1016/j.csda.2015.11.010>.
- 541 Sato, M., J. E. Hansen, M. P. McCormick and J. B. Pollack (1993). "Stratospheric aerosol
542 optical depths, 1850-1990." *J. Geophys. Res.* **98**: 22987-22994 DOI: 10.1029/93JD02553.
- 543 Schwartz, S. E., n. Harshvardhan and C. M. Benkovitz (2002). "Influence of anthropogenic
544 aerosol on cloud optical depth and albedo shown by satellite measurements and chemical
545 transport modeling." *Proceedings of the National Academy of Sciences* **99**(4): 1784-1789
546 DOI: 10.1073/pnas.261712099.
- 547 Vernier, J., L. Thomason, J. P. Pommereau, A. Bourassa, J. Pelon, A. Garnier, A.
548 Hauchecorne, L. Blantot, C. Trepte, D. Degenstein and F. Vargas (2011). "Major influence of
549 tropical volcanic eruptions on the stratospheric aerosol layer during the last decade."
550 *GEOPHYSICAL RESEARCH LETTERS* **38** DOI: 10.1029/2011GL047563.

This manuscript has been submitted for publication to JOURNAL OF CLIMATE (AMS). Please note that this manuscript has undergone two rounds of peer review but has yet to be formally accepted for publication. Subsequent versions of this manuscript may differ slightly in content.

- 551 Wan, E. A. and R. Van Der Merwe (2000). The unscented Kalman filter for nonlinear
552 estimation, Institute of Electrical and Electronics Engineers Inc. DOI:
553 10.1109/ASSPCC.2000.882463.
- 554 Wielicki, B. A., B. R. Barkstrom, E. F. Harrison, R. B. Lee, G. Louis Smith and J. E. Cooper
555 (1996). "Clouds and the Earth's Radiant Energy System (CERES): An Earth Observing
556 System Experiment." Bulletin of the American Meteorological Society **77**(5): 853-868 DOI:
557 10.1175/1520-0477(1996)077<0853:catere>2.0.co;2.
- 558 Wild, M., D. Folini, M. Z. Hakuba, C. Schär, S. I. Seneviratne, S. Kato, D. Rutan, C.
559 Ammann, E. F. Wood and G. König-Langlo (2015). "The energy balance over land and
560 oceans: an assessment based on direct observations and CMIP5 climate models." Climate
561 Dynamics **44**(11): 3393-3429 DOI: 10.1007/s00382-014-2430-z.
- 562 Wild, M., M. Z. Hakuba, D. Folini, P. Dörig-Ott, C. Schär, S. Kato and C. N. Long (2019).
563 "The cloud-free global energy balance and inferred cloud radiative effects: an assessment
564 based on direct observations and climate models." Climate Dynamics **52**(7): 4787-4812 DOI:
565 10.1007/s00382-018-4413-y.
- 566 Zanna, L., S. Khatiwala, J. M. Gregory, J. Ison and P. Heimbach (2019). "Global
567 reconstruction of historical ocean heat storage and transport." Proceedings of the National
568 Academy of Sciences **116**(4): 1126-1131 DOI: 10.1073/pnas.1808838115.
- 569 Zhong, W. and J. Haigh (2013). "The greenhouse effect and carbon dioxide." Weather **68**:
570 100-105 DOI: 10.1002/wea.2072.
- 571